
Doctoral Dissertations

Student Theses and Dissertations

Summer 2008

A tour-de-force in polymer crosslinked aerogels

Sudhir Mulik

Follow this and additional works at: https://scholarsmine.mst.edu/doctoral_dissertations

 Part of the [Chemistry Commons](#)

Department: Chemistry

Recommended Citation

Mulik, Sudhir, "A tour-de-force in polymer crosslinked aerogels" (2008). *Doctoral Dissertations*. 1935.
https://scholarsmine.mst.edu/doctoral_dissertations/1935

This thesis is brought to you by Scholars' Mine, a service of the Missouri S&T Library and Learning Resources. This work is protected by U. S. Copyright Law. Unauthorized use including reproduction for redistribution requires the permission of the copyright holder. For more information, please contact scholarsmine@mst.edu.

A TOUR-DE-FORCE IN POLYMER CROSSLINKED AEROGELS

by

SUDHIR M. MULIK

A DISSERTATION

Presented to the Faculty of the Graduate School of the
MISSOURI UNIVERSITY OF SCIENCE AND TECHNOLOGY

In Partial Fulfillment of the Requirements for the Degree

DOCTOR OF PHILOSOPHY

in

CHEMISTRY

2008

Approved by

Dr. Chariklia Sotiriou-Leventis, Advisor

Dr. Nicholas Leventis, Co-Advisor

Dr. James Stoffer

Dr. Phillip Whitefield

Dr. Isaac Kakkattukuzhy

© 2008

Sudhir Mansing Mulik

All Rights Reserved

PUBLICATION DISSERTATION OPTION

This dissertation consists of the following three manuscripts for publication:

Pages 17-67 have been accepted for publication in *Chemistry of Materials*.

Pages 68-95 have been published in *Chemistry of Materials* **2007**, *19*, 6138-6144.

Pages 96-145 have been prepared for submission to *Chemistry of Materials*.

ABSTRACT

In the quest of building mechanically strong materials with low density and high porosity, polymer crosslinked aerogels stand as the most promising nano-engineered examples. Covalent attachment of polymers and bridging of skeletal nanoparticles of typical aerogels is demonstrated by using surface initiated polymerization (SIP) with a bidentate free-radical initiator structurally related to azobisisobutyronitrile (AIBN) and confined on mesoporous silica surfaces. Different monomers were introduced in the mesopores and upon heating at 70 °C, all mesoporous surfaces throughout the entire skeletal framework were coated conformally with a 10-12 nm thick polymer layer indistinguishable spectroscopically from the respective commercial bulk materials. The new materials combine hydrophobicity with vastly improved mechanical properties.

Resorcinol formaldehyde (RF) aerogels are pursued as precursors of carbon aerogels, which are electrically conducting. We have developed a HCl-catalyzed gelation process in CH₃CN, which is completed in ~ 2 h at room temperature as opposed to the week-long base-catalyzed literature process. The final aerogels are spectroscopically indistinguishable from typical base-catalyzed samples. Carbon (C-) aerogels are made by pyrolysis of RF aerogels, and combine electrical conductivity with a high open mesoporosity. Nevertheless, macropores facilitate mass-transfer and they could be beneficial for applications in separations or as fuel cell and battery electrodes. Here, we report a method where an open macroporosity is introduced by pyrolysing RF aerogels whose skeletal nanoparticles have been coated conformally and crosslinked chemically with an isocyanate-derived polymer. The new macroporous material was evaluated electrochemically for possible application as an electrode in batteries and fuel cells.

ACKNOWLEDGEMENTS

First, I would like to thank my advisor, Prof. Chariklia Sotiriou-Leventis and co-advisor, Prof. Nicholas Leventis for being the best mentors one can ask for. I would like to express my gratitude to them for their guidance, advice and for sincere concern about my future and life. Their scientific perception and friendship are perhaps only surpassed by their courage in allowing their students to explore the vast scientific landscape, in order to train us to be freethinking independent scientists at the end of the journey. They made me realize that apart from knowing your subject and hard work you need passion and imagination to invent and discover.

I would like to express my gratitude and deep appreciation to my advisory committee members, Dr. James Stoffer, Dr. Phillip Whitefield and Dr. Kakkattukuzhy Isaac for their time and valuable suggestions. I also would like to express my gratitude to our research collaborator Dr. Hongbin Lu at Oklahoma State University for his valuable suggestions and help with mechanical testing.

I would like to thank Mr. Mike Myer for his help and Mr. Joe Council for training me on the departmental instruments and all the professors and staff in the department for being there for me, and The University of Missouri Science and Technology (Missouri S&T) for providing me with a great working environment. I am deeply indebted to Manesh, Vinita, Rakesh, Yogesh and Anand for their continuous heartfelt support throughout my stay here. Special thanks are due to all my friends, no matter where I go they will always remain in my heart. Finally, words alone can not express the thanks I owe to my parents and brother for their encouragement and love bestowed upon me throughout my life. It is to them, I dedicate my thesis.

TABLE OF CONTENTS

	Page
PUBLICATION DISSERTATION OPTION	iii
ABSTRACT.....	iv
ACKNOWLEDGMENTS	v
LIST OF ILLUSTRATIONS.....	ix
LIST OF SCHEMES.....	xii
LIST OF TABLES.....	xiii
LIST OF ABBREVIATIONS.....	xiv
SECTION	
1. INTRODUCTION.....	1
1.1. AEROGELS: NANOMATERIALS BEFORE NANOMATERIALS EXISTED	1
1.2. AEROGELS AND SOL-GEL CHEMISTRY.....	3
1.3. POLYMER CROSSLINKED AEROGELS	6
1.4. TECHNOLOGY SUMMARY	10
1.5. CHALLENGES AND PROGRESS IN POLYMER CROSSLINKED AEROGELS.....	11
REFERENCES.....	14
PAPER	
I. CROSSLINKING 3D ASSEMBLIES OF NANOPARTICLES INTO MECHANICALLY STRONG AEROGELS BY SURFACE-INITIATED FREE RADICAL POLYMERIZATION	17
1. ABSTRACT	17
2. INTRODUCTION	18
3. EXPERIMENTAL	22
3.1. Materials	22
3.1.1. Synthesis of 4,4'-(diazene-1,2-diyl)bis(4-cyano- <i>N</i> -(3-(triethoxysilyl)propyl)-pentamide) (1)	22
3.1.2. Preparation of native silica aerogels incorporating 1 (native Si-1).....	23
3.1.3. Preparation of polymer crosslinked aerogels incorporating 1 (X-Si-1- polymer).....	24

3.2. Methods	25
4. RESULTS AND DISCUSSION	29
4.1. Synthesis, incorporation of 1 in mesoporous silica and preparation of polymer crosslinked aerogels.....	29
4.2. Physical, chemical and morphological characterization of native and crosslinked aerogels	32
4.2.1. Native silica aerogels incorporating 1 (native Si-1).....	32
4.2.2. Silica aerogels crosslinked with PMMA (X-Si-1-PMMA), PS (X-Si-1-PS) and PDVB (X-Si-1-PDVB)	34
4.2.3. Mechanical properties of X-Si-1-polymer	41
5. CONCLUSIONS	44
6. ACKNOWLEDGEMENTS	45
7. REFERENCES.....	46
8. FIGURES	51
9. SUPPORTING INFORMATION	63
II. TIME-EFFICIENT ACID-CATALYZED SYNTHESIS OF RESORCINOL-FORMALDEHYDE AEROGELS.....	68
1. ABSTRACT	68
2. INTRODUCTION	69
3. EXPERIMENTAL	71
3.1. Materials	71
3.2. Methods	73
4. RESULTS.....	74
4.1. Reaction of resorcinol with formaldehyde in HCl-catalyzed CH ₃ CN solutions.....	74
4.2. Time-efficient preparation and characterization of RF aerogels.....	75
5. DISCUSSION	81
6. CONCLUSIONS	85
7. ACKNOWLEDGEMENTS	85
8. REFERENCES.....	86
9. FIGURES	89

III. MACROPOROUS ELECTRICALLY CONDUCTING CARBON NETWORKS BY PYROLYSIS OF ISOCYANATE-CROSSLINKED RESORCINOL- FORMALDEHYDE AEROGELS.....	96
1. ABSTRACT	96
2. INTRODUCTION	97
3. EXPERIMENTAL	99
3.1. Materials	99
3.1.1. Preparation of native RF aerogels.	99
3.1.2. Preparation of isocyanate-crosslinked RF aerogels.....	100
3.1.3. Preparation of polyurea aerogels.....	101
3.1.4. Preparation of carbon aerogels	101
3.2. Methods.....	101
4. RESULTS AND DISCUSSION	103
4.1. Native RF aerogels and their crosslinking with isocyanates.....	103
4.2. Preparation of polyurea aerogels.....	110
4.3. Pyrolysis of native RF, X-RF and polyurea aerogels.....	111
4.4. Chemical, physical and morphological evolution of RF, X-RF and polyurea aerogels upon heat treatment	115
4.4.1. Physical and chemical characterization after heat treatment at different temperatures.	115
4.4.2. Morphological characterization after heat treatment at different temperatures.....	117
4.5. Electrochemical evaluation of C-aerogels made from X-RF aerogels.....	120
5. CONCLUSIONS	121
7. ACKNOWLEDGEMENTS	122
8. REFERENCES.....	123
9. FIGURES	126
6. SUPPORTING INFORMATION	142
VITA	146

LIST OF ILLUSTRATIONS

Figure	Page
1.1 Sol-gel processes for aerogel preparation	5
1.2 Nanostructure of mesoporous silica.....	7
1.3 Preparation of polymer crosslinked aerogels.....	9
1.4 Polymer tethers connecting interparticle necks in polymer crosslinked aerogels	10
PAPER I	
1. Scanning Electron Micrographs of: (A) native Si-1; (B) X-Si-1-PMMA; (C) X-Si-1-PS.....	51
2. Nitrogen sorption porosimetry	52
3. FTIR spectra (in KBr) of compound 1, native Si-1 and crosslinked aerogels X-Si-1-PMMA and X-Si-1-PS in comparison with neat PMMA and PS.....	53
4. (A) Liquid ¹³ C NMR of 1 in CDCl ₃ (marked as “S”)	54
(B) Solid ¹³ C CPMAS NMR of samples as indicated.....	55
5. Solid state ²⁹ Si CPMAS NMRs of: (A) base-catalyzed, TMOS-only native silica; (B) native Si-1; (C) X-Si-1-PMMA; and, (D) X-Si-1-PS.....	56
6. Thermogravimetric analysis (TGA) at 10 °C min ⁻¹ in air of (A) compound 1 and native Si-1; (B) crosslinked samples of X-Si-1-PMMA and X-Si-1-PS at the densities shown	57
7. Back-illuminated water droplets on flat surfaces cut off from cylinders of X-Si-1-PMMA and of X-Si-1-PS, as indicated	58
8. Log(Porosity) as a function of Log(Bulk Density) for all samples prepared	59
9. Shift in glass transition temperature (T _g) of PMMA and PS coated conformally and covalently bonded on the skeletal nanoparticles of X-Si-1-PMMA and X-Si-1-PS, in comparison to the neat polymers.....	60
10. Mechanical characterization of X-Si-1-PMMA and X-Si-1-PS	61
11. Top: Samples before compression, left: X-Si-1-PMMA; right: X-Si-1-PS. Bottom: Samples after compression, left: X-Si-1-PMMA; right: X-Si-1-PS, in comparison to the neat polymers	62
SUPPORTING INFORMATION	
1S. A two-sphere model for two secondary particles connected to each other.....	64
2S. Contours of the normal stresses in the Y direction	65

3S. Bending stiffness ratio of polymer nano-encapsulated secondary silica nanoparticles as a function of the dimensionless contact diameter of the secondary silica nanoparticles.....	67
4S. Bending stiffness ratio of polymer encapsulated secondary silica nanoparticles to the neat silica nanoparticles for dimensionless contact diameters of 0.2774, 0.3364, and 0.3992, as a function of the increase in densities of cross-linked samples due to polymer nanoencapsulation.....	67

PAPER II

1. Solution ^{13}C NMR of resorcinol/formaldehyde mixtures in 1:2 mol ratio in CD_3CN	89
2. Evolution of the absorbance of a resorcinol/formaldehyde mixture at 1:2 mol ratios in CH_3CN at room temperature.....	90
3. Viscosity evolution of three solutions as indicated, according to ASTM D 562-01 ...	91
4. (A) SEM of a RF aerogel prepared according to Scheme 1, using a mol ratio of R:F=1:3. (B) For comparison, SEM of a native silica aerogel of similar density	92
5. Nitrogen sorption isotherms for a RF aerogel prepared according to Scheme 1 using R:F=1:2 at room temperature, 1 day aging	93
6. Infrared spectra (in KBr) of two RF aerogels prepared with the R:F ratios indicated.....	94
7. ^{13}C CPMAS NMR of two RF aerogels as indicated.....	95

PAPER III

1. Scanning Electron Microscopy (SEM) of a native RF aerogel (A), and of a Desmodour N3300A tri-isocyanate crosslinked (X-RF) aerogel (B), prepared according to Scheme 1	126
2. Thermogravimetric Analysis (TGA) and Differential Scanning Calorimetry (DSC) both under N_2 of native RF aerogels	127
3. Nitrogen sorption porosimetry	128
4. Solid ^{13}C CPMAS NMR of acid-catalyzed native RF aerogel (A), a X-RF aerogel sample crosslinked with Desmodur N3300A without catalyst (B) and a X-RF aerogel sample crosslinked with Desmodur N3300A in the presence of TEA (C)	129
5. Photograph (A) and SEM (B) of a polyurea aerogel sample prepared by gelation of Desmodur N3300A in acetone/water in the presence of TEA	130
6. Thermogravimetric analysis under N_2 of a native RF, two X-RF samples, one crosslinked with Desmodur N3200 di-isocyanate and one with Desmodur N3300A tri-isocyanate, and a polyurea aerogel, as indicated.....	131

7. Photographs of carbon aerogels prepared by pyrolysis at 800 °C under Ar of native RF aerogels and of X-RF aerogels prepared using Desmodur N3300A tri-isocyanate and TEA	132
8. SEM of carbon aerogels made by pyrolysis of native RF aerogels (A), X-RF aerogels crosslinked with Desmodur N3300A tri-isocyanate (B) and X-RF aerogels crosslinked with Desmodur N3200 di-isocyanate (C).....	133
9. Nitrogen sorption porosimetry	134
10. Differential Scanning Calorimetry (DSC) under N ₂ at 10 °C min ⁻¹ of two X-RF samples, one crosslinked with Desmodur N3200 di-isocyanate and one with Desmodur N3300A tri-isocyanate, and a polyurea aerogel, as indicated.....	135
11. Solid ¹³ C CPMAS NMR of polyurea aerogels: as-made (A), after heating under Ar for 3 h at 250 °C (B) and at 300 °C (C)	136
12. Solid ¹³ C CPMAS NMR of native RF and X-RF-N3300A aerogels as indicated....	137
13. SEM of four types of aerogels, heat-treated under Ar for 3 h at three different temperatures, as indicated.....	138
14. Looking inside the skeletal framework: (A) Survey SEM and SEM at the fracture (see inset) on the skeletal framework of an X-RF sample crosslinked with Desmodur N3200 (X-RF-N3200) and heat-treated under Ar at 300 °C. (B) Survey SEM and SEM at the fracture (see inset) on the skeletal framework of a C-aerogel prepared by pyrolysis under Ar at 800 °C of a X-RF-N3300A aerogel...	139
15. Cyclic voltammetry of ferrocene (3 mM) in CH ₃ CN/0.1 M TBAP at 0.1 V s ⁻¹ , using a Pt disc electrode (1 mm in diameter), or a C-aerogel electrode (0.008 g) made from a X-RF-N3300A aerogel, as indicated	140
16. (A) SEM of a carbon aerogel prepared by pyrolysis of a X-RF-N3300A aerogel after electrodeposition of Pt from a 3 mM solution of K ₂ PtCl ₄ in CH ₃ CN/0.1 M TBAP containing enough water to solubilize the salt. (B) Energy Dispersive Spectra (EDS)-derived Pt map at the same location.....	141

SUPPORTING INFORMATION

1S. FTIR spectra of RF and X-RF aerogels	142
2S. Solid ¹³ C CPMAS NMR of acid-catalyzed native RF aerogel (A), a X-RF aerogel sample crosslinked with Desmodur N3200 without catalyst (B) and a X-RF aerogel sample crosslinked with Desmodur N3200 in the presence of TEA.....	143
3S. XRD of C-aerogels.	144
4S. SEM of silica aerogels crosslinked with Desmodur N3200 and heat-treated for 3 h under Ar at three different temperatures, as indicated.....	145

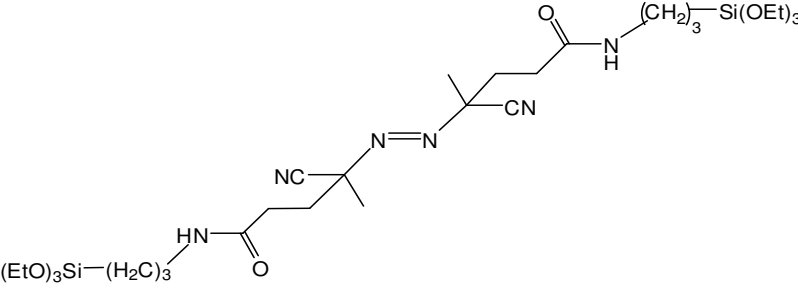
LIST OF SCHEMES

Scheme	Page
PAPER I	
1. Preparation of the bidentate initiator 1.....	30
2. Preparation of native silica aerogels incorporating 1 (native Si-1) and crosslinking with MMA, styrene or DVB into X-Si-1-polymer.....	31
3. Crosslinking through termination of chain reactions initiated by bidentate free radical initiator on the mesoporous surfaces of 3D assemblies of silica nanoparticles	40
4. The effect of a conformal polymer coating on the stiffness of a two-particle system	43
PAPER II	
1. Time-Efficient Synthesis of Resorcinol-Formaldehyde Aerogels.....	76
2. Proposed Mechanism for RF Gel Formation under Acid (HCl) Catalysis	82
PAPER III	
1. Synthesis of native and isocyanate crosslinked resorcinol-formaldehyde aerogels (RF and X-RF, respectively).....	105
2. Crosslinking of an RF network with and without TEA as crosslinking catalyst.....	110
3. First decomposition pathway of polyurea aerogels	116

LIST OF TABLES

Table	Page
PAPER I	
1. Selected Properties of X-Si-1-polymer (polymer: PMMA, PS or PDVB).....	27
PAPER II	
1. Physical characterization data for RF aerogels processed under various conditions..	77
PAPER III	
1. Physical characterization of native and isocyanate crosslinked RF aerogels processed under various conditions	108
2. Material characterization data of polyurea aerogels derived from Desmodur N3300A.....	111
3. Characterization of carbon aerogels derived from native RF and X-RF aerogels	114
4. Pertinent materials characterization data of various samples after heat-treatment under Ar at three different temperatures as indicated.....	119

LIST OF ABBREVIATIONS

Abbreviation	Description
MMA	Methyl Methacrylate
PMMA	Poly(methyl methacrylate)
DVB	Divinylbenzene
PDVB	Poly(divinylbenzene)
PS	Poly(styrene)
TEA	Triethylamine
Compound 1	 <p data-bbox="558 1528 1084 1598">4,4'-(diazene-1,2-diyl)bis(4-cyano-<i>N</i>-(3-(triethoxysilyl)propyl)pentanamide</p>
TMOS	Tetramethoxysilane
Native Si aerogel	Silica aerogel prepared by using TMOS as the sol-gel precursor

Native Si-1 aerogel	Silica aerogel prepared by using compound 1 together with TMOS as the sol-gel precursor
X-Si-1-polymer aerogel	Silica aerogels prepared from crosslinking Native Si-1 aerogels with any polymer
X-Si-1-PMMA aerogel	Silica aerogels prepared from crosslinking Native Si-1 aerogels with PMMA
X-Si-1-PS aerogel	Silica aerogels prepared from crosslinking Native Si-1 aerogels with PS
X-Si-1-PDVB aerogel	Silica aerogels prepared from crosslinking Native Si-1 aerogels with PDVB
RF aerogel	Resorcinol-formaldehyde aerogel
Native RF aerogel	Same as “RF aerogel”
X-RF aerogel	RF aerogel crosslinked with isocyanate derived polymer
X-RF-N3200	Resorcinol formaldehyde aerogel crosslinked with Desmodur N3200 di-isocyanate (from Bayer)
X-RF-N3300A	Resorcinol formaldehyde aerogel crosslinked with Desmodur N3300A tri-isocyanate (from Bayer)
C-aerogel	Carbon aerogel
SIP	Surface initiated polymerization
SCF	Supercritical fluid

1. INTRODUCTION

1.1 AEROGELS: NANOMATERIALS BEFORE NANOMATERIALS EXISTED

The essence of nanotechnology is the ability to work at the molecular organization level, in order to create large macroscopic structures with fundamentally new bulk material properties. Specifically, nanotechnology refers broadly to a field of applied science and technology whose unifying theme is the control of matter on the atomic and molecular scale, normally 1 to 100 nanometers, and the fabrication of assemblies, structures and devices with critical dimensions that lie within that size range. Nanotechnology is concerned with materials and systems whose structures and components exhibit novel and significantly improved physical, chemical, and biological properties, phenomena, and processes due to their organization at the nanoscale size regime. Therefore, from a materials perspective, nanotechnology is the use of molecular science (chemistry, physics) to manipulate matter in the 1-100 nm size regimes in order to achieve useful macroscopic properties.¹ Generally, two main approaches are used in nanotechnology in order to create assemblies of nanoscopic dimension. In the "bottom-up" approach, materials and devices are built from molecular components, which assemble themselves chemically by principles of molecular recognition and in the "top-down" approach, where nano-objects are constructed by breaking down larger entities.

Out of the world of nano-structured materials, quasi-stable, ultra-low density, three-dimensional assemblies of nanoparticles are referred to as aerogels, and they have picked up interest because of their versatile bulk properties such as low density, low

dielectric constant, low thermal conductivity, high surface area and high acoustic impedance. All those properties are results of their open-cell mesoporous structure with a large internal void space (up to >99%).²⁻³ Aerogels are classified as open cell foams, and they can be purely organic materials (like resorcinol-formaldehyde, phenol-formaldehyde, melamine-formaldehyde or polyurea aerogels) or purely inorganic materials (mostly metal and semimetal oxides), and they are derived by supercritical fluid (SCF) drying of wet gels, which in turn are prepared via sol-gel chemistry.⁴ Despite the attractive properties, however, aerogels are also very fragile materials, and that has limited applications.⁵

Historically, aerogels were first reported by Kistler in 1931.⁶ His materials were prepared by exchanging pore-filling liquids in wet gels with air, without a substantial change in pore and network structure. Kistler's method of preparing wet-gels was based on an acid-catalyzed gelation of sodium silicate followed by extensive washing with water in order to remove sodium chloride produced as the gelation byproduct. Subsequently, water was exchanged with methanol, which in turn was removed supercritically. The first commercially available aerogels were produced in 1942 by the Monsanto Corporation, under the trade name Santocel.⁷ Monsanto described the product as "a light, slightly opalescent solid containing as much as 95 percent air volume which is a very effective heat insulating material." In the 1960s the Teichner group efforts to use the sol-gel process involving hydrolysis and condensation of alkoxy silane, in the preparation of silica wet-gels reduced the preparation time from weeks to days.⁸ After the practical use of aerogels in Cerenkov detectors, new developments in aerogels science and technology occurred rapidly as an increasing number of researchers joined the field.

Until recently, many commercial applications such as thermal window insulation, acoustic barriers, supercapacitor and catalyst supports were all proposed but little in the way of actual use had resulted.^{9,10} In 1990s, NASA employed aerogel in two missions namely, the Mars Pathfinder and the Stardust Program.¹¹ Those projects utilized the unique thermal insulations (Mars Pathfinder) and mechanical properties of aerogels (Stardust). Since the early 2000s commercialization and efforts for mass production of aerogels have been intensified, and various new day-to-day applications and different market segments have been proposed. Thus, in addition to more sophisticated applications in space missions, fuel cells and catalysis, the usage of aerogels as thermal insulation in shoes/jackets, as lightweight materials in squash rackets or as water filters have made commercial scale production more promising and attractive.

Overall, however, in spite the versatile properties of aerogels, their application has been limited because of their fragility. Attempts to address the fragility problem led us to produce the next generation of aerogels referred to as “polymer crosslinked aerogels.” By using chemical means to cast a thin conformal polymer coating over the entire internal porous surface of the nanostructure, polymer crosslinked aerogels are still light weight materials with enormous increase in strength extending their usage in high load applications.¹²

1.2 AEROGELS AND SOL-GEL CHEMISTRY

The sol-gel process is a versatile “bottom-up” solution process, initially used for the preparation of inorganic materials such as glasses and ceramics of high purity and homogeneity. The sol-gel route offers a degree of control on composition and structure at

the molecular level. The process involves the reactive generation of a colloidal suspension (sol), which is subsequently converted to a viscous gel.⁴ More precisely, a 'sol' is a colloidal system of *liquid* character in which the dispersed particles are either solid or large molecules whose dimensions are in the colloidal range of 1-1000 nm and a 'gel' is a colloidal system of *solid* character in which the dispersed substance forms a continuous, coherent framework that is interpenetrated by a system (usually liquid) consisting of kinetic units smaller than colloidal entities.¹⁴ A gel can be easily imagined as a three-dimensional network of solid building blocks filled with a solvent. The sol-gel chemistry has been studied widely and extends into both organic as well as inorganic precursors.

Aerogels are prepared in two stages. The first stage involves formation of wet-gels by means of sol-gel chemistry, and the second stage involves drying of wet-gels without damaging the pore and network structure.¹³ Figure 1.1 summarizes the typical sol-gel processes for aerogel preparation. In the preparation of a silica glass, one first starts with an appropriate alkoxide, such as tetramethoxysilane (TMOS) or tetraethoxysilane (TEOS), which is mixed with water and a mutual solvent, such as ethanol or methanol, to form a solution, which in the presence of an appropriate acid or base catalyst undergoes hydrolysis leading to the formation of free silanols (-Si-OH). These species are only intermediates as they react further, i.e. condense, to form siloxanes (-Si-O-Si-). As the hydrolysis and condensation reactions continue, the viscosity of the reaction mixture increases until the "sol" ceases to flow and forms a "gel."

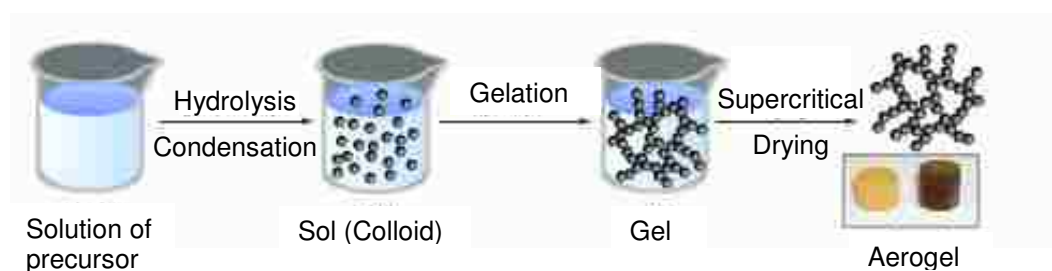
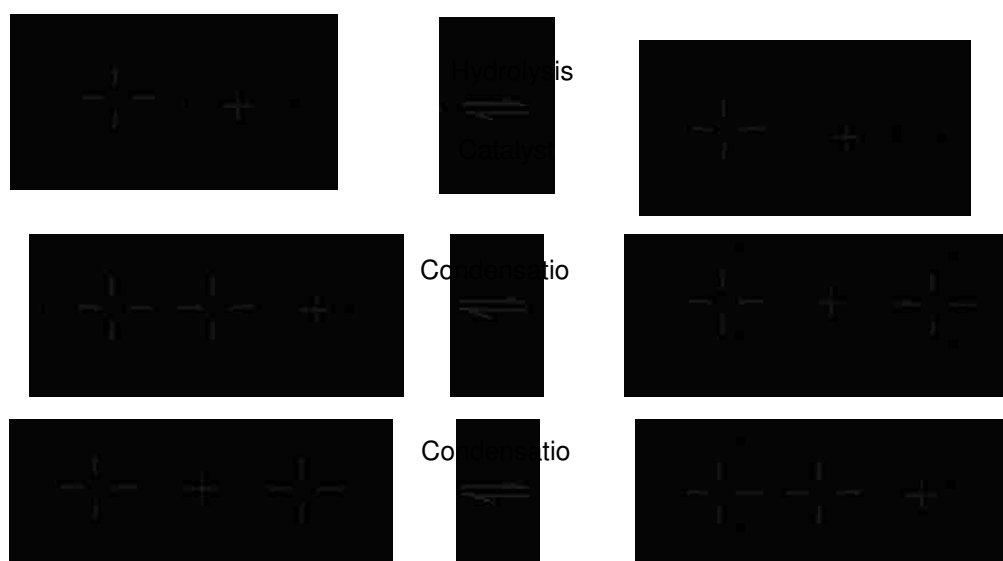


Figure 1.1 Sol-gel processes for aerogel preparation.

There are several parameters which influence the hydrolysis and condensation reactions of the sol-gel process. For example, for inorganic gels those include include the activity of metal alkoxide, the water/alkoxide ratio, the solution pH, the temperature, and nature of the solvent. By varying those parameters, materials with different microstructure and surface chemistry can be obtained. Further processing of the "sol" enables one to make ceramic materials of different forms. Generally, in case of inorganic precursors like tetramethoxysilane (TMOS) the overall sol-gel reactions are:



In case of organic precursors, although the gelation occurs by a different mechanism compared to that of inorganic precursors, the processing steps are very similar in both cases. The final gels are aged for a period of time to allow the gel network to strengthen (syneresis). If the liquid in a wet-gel is removed under supercritical conditions, a highly porous and extremely low density solid material called "aerogel" is obtained.

During supercritical drying, the solvent from the last wash-step filling the mesopores of the wet-gel is exchanged with liquid CO₂ in an autoclave and when the temperature and pressure inside the autoclave are raised to above the critical point of CO₂ (32 °C, 73.8 bar), the entire volume of the liquid CO₂ goes into the supercritical phase all at once. This prevents formation of a liquid-gas interfacial meniscus retreating through the pores of the wet gel. Hence, since no surface tension forces are ever exerted on the skeletal framework as during ambient pressure drying, SCF drying leaves the geometric dimensions of the wet gel unchanged, and the resulting aerogels are very low density objects (3-800 mg cm⁻³).

1.3 POLYMER CROSSLINKED AEROGELS

Aerogels have been considered as thermal and acoustic insulators, dielectrics and as hosts of functional guests for optical, electronic and chemical applications (supports for catalysts, platforms for sensors etc.)¹ However, none of those applications has been materialized, because conventional aerogels are fragile materials. Microscopically, aerogels consist of a continuous random "pearl like" three dimensional network of secondary particles (5-10 nm) that define the network of 2-50 nm diameter

interconnected voids which are referred to as mesopores.¹⁵ Figure 1.2 shows schematically the nanostructure of mesoporous silica. In general, the strength of porous materials increases with an increase in the pore wall thickness and decreases with an increase in the pore diameter. Specifically for aerogels, pore walls have well-defined weak joints which are referred to as interparticle “necks.”



Figure 1.2 Nanostructure of mesoporous silica.

The fragility of aerogels is traced to the interparticle necks. Those are formed upon particle coagulation during gelation and become wider by dissolution and re-precipitation of silica during aging (syneresis).¹⁶ As necks become wider, in other words as the accumulation of more materials reinforces these weak joints, the mechanical strength of the bulk material increases. This process, however, is self-limiting because preferential re-precipitation at the necks stops as soon as the curvature is no longer

negative. Inspired by the processes taking place during aging of wet gels, another method by which necks can be reinforced is via post-gelation incorporation of interparticle molecular tethers bridging and covalently connecting the skeletal nanoparticles. The interparticle tethers can be polymeric and the new materials are referred to as polymer crosslinked aerogels.¹² Since the reinforcing polymer is confined at the contours of the skeletal framework, crosslinked aerogels preserve the porosity and the useful properties of their native counterparts.

In the quest of building mechanically strong materials with low density and high porosity, polymer crosslinked aerogels stand as the most promising nano-engineered materials. Classification-wise, polymer crosslinked aerogels are three-dimensional (3D) core-shell superstructures, as opposed to core-shell single particles. Figure 1.3 shows the preparation of polymer crosslinked aerogels. In that regard, three degrees of freedom were recognized in their design: the chemical identity of the framework, the chemical identity of the polymer and the nanoparticle surface functionality. The latter is seemingly the most versatile parameter in new material design because by careful choice of the reactive group on the surface of silica, one can incorporate a variety of polymers. This has been demonstrated for instance with the amine functionality, which has become the point of attachment for polyurea (via reaction with di-isocyanates),¹⁷⁻²⁰ epoxy resins (via reaction with epoxides),²¹ or even polystyrene (PS) after further surface modification with styrene via a lengthy process that involves reaction of dangling amines with *p*-chloromethylstyrene.¹⁵

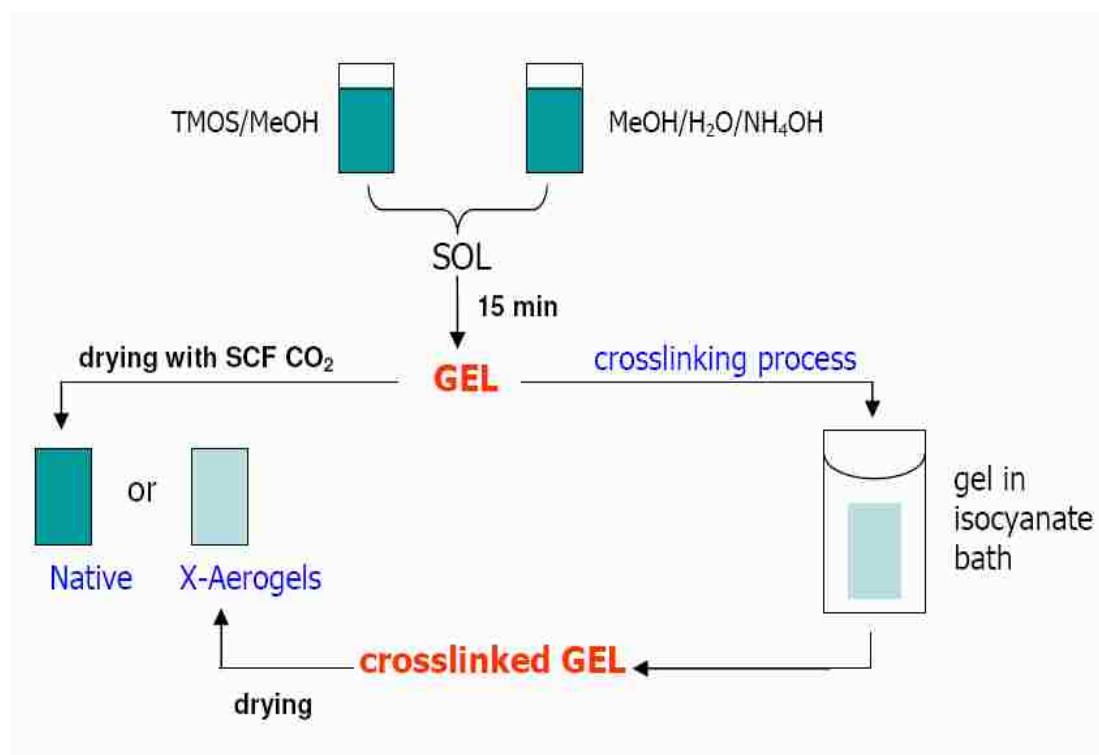


Figure 1.3 Preparation of polymer crosslinked aerogels.

Crosslinked silica aerogels (X-aerogels) are very strong mechanically, while the high porosity of the native (non-crosslinked) framework is preserved. Thus, unique macroscopic properties of the native material, such as low thermal conductivity and high acoustic impedance are maintained. Cross-linking of silica aerogels with isocyanates effectively mimics polyurethane chemistry, where a polyfunctional isocyanate reacts with a polyfunctional alcohol to form carbamates (urethanes). In case of silica aerogels, the role of functional polyols is played by hydroxyl groups on the surface of silica. Surface modified silicas with amines and epoxy groups were crosslinked with similar chemistry. Figure 1.4 shows polymer tethers connecting interparticle necks in polymer crosslinked aerogels.

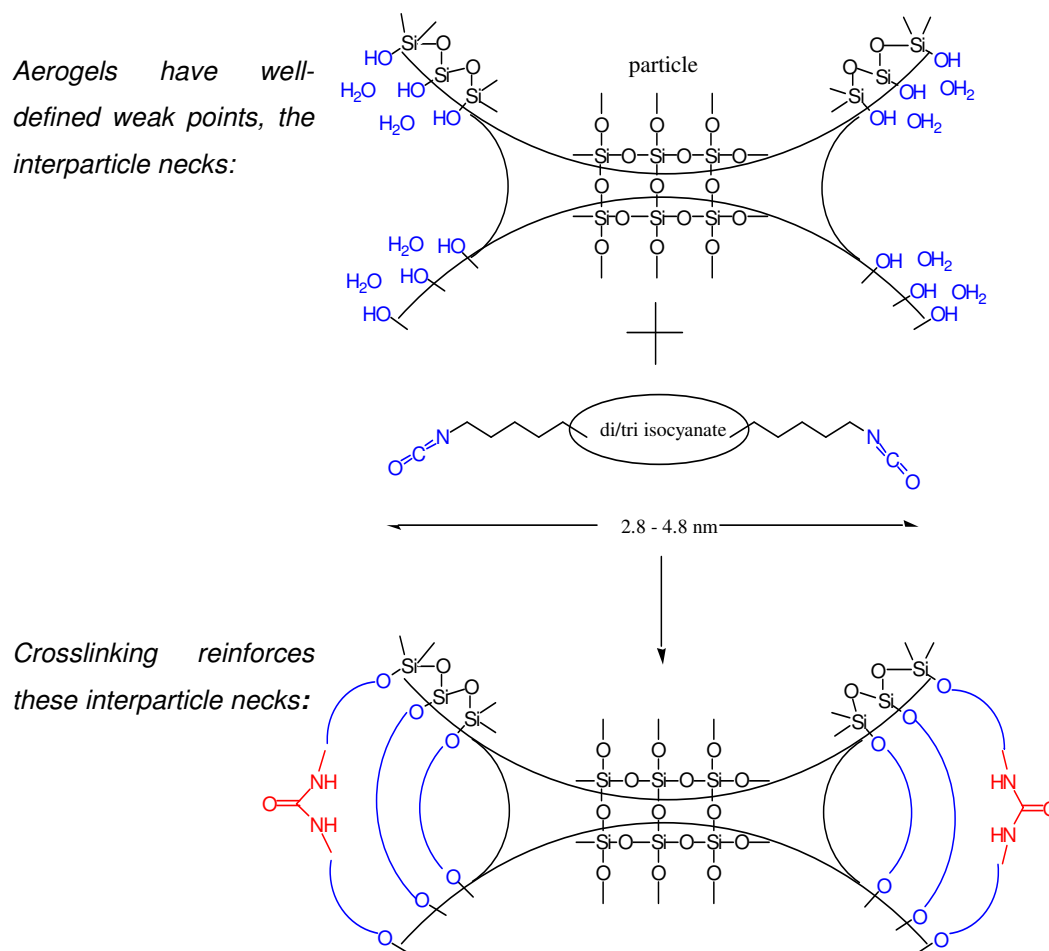


Figure 1.4 Polymer tethers connecting interparticle necks in polymer crosslinked aerogels.

1.4 TECHNOLOGY SUMMARY

The crosslinked aerogels (X-aerogels) are three dimensional superstructures in which the conformal coating of polymer causes 3 fold increase in density but the mechanical strength is enhanced by 300 times. This versatile crosslinking chemistry works for a range of polymers and exhibits similar increase in strength when expanded over aerogels made from 30 different oxides.

1.5 CHALLENGES AND PROGRESS IN POLYMER CROSSLINKED AEROGELS

From a chemical perspective, it was necessary to expand the crosslinking chemistry of polymer crosslinked aerogels in order to take advantage of numerous monomers available and to explore new dimensions in this technology. Also, with an eye on the efficient large-scale manufacturing of polymer crosslinked aerogels, chemical process design and scale-up process optimization should comprise one integral part. Therefore from that perspective, the principal scientific objective was to develop methodology for crosslinking aerogels with most major classes of polymers. The incorporation of polymer chains will reinforce the interparticle necks by forming a conformal coating on nano particles and eventually, the fragility issue will be addressed. Those mechanical strong aerogels can be used to replace other heavy materials used in a wide variety of applications, for example, ranging from ballistics to acoustic, and thermal insulation to construction. In this regard, the methodology for decorating the surface of the skeletal backbone with free-radical initiators similar to that of AIBN followed by crosslinking with commercially available monomers has been developed.

Although various literature reports explain the importance of free radical initiators bonded to the surface of silica via a wide variety of interactions such as covalent bonding, ionic bonding or simply via physical adsorption, nevertheless most practical examples concern asymmetric peroxides and AIBN derivatives attached on silica by one side only. In particular, physical adsorption and ionic bonding²³⁻²⁵ of free radical initiators on the surface of silica have been studied extensively in the spirit of exploring the ‘grafting from’ surface-initiated polymerization (SIP). Prucker et al. reported the immobilization of an AIBN-like monodentate azo-compound on silica.²⁶ Advincula and coworkers also

showed the attachment of an ionically bound free radical initiator on clay nanoparticles.²³ Monodentate free-radical initiators have the disadvantage that upon homolytic cleavage they produce only one surface-bound radical, releasing a second radical in the solution. For our purposes, that is with an eye to one-step/one-pot processing from gelation to crosslinking, we need bidentate free-radical initiators that will attach themselves on silica from both ends.²⁷ Thus, we report the facile synthesis of a bis-triethoxysilane derivative of AIBN and its incorporation in silica wet-gels and aerogels and its use for obtaining mechanically strong polymer crosslinked aerogels by SIP of methylmethacrylate (MMA), styrene and divinylbenzene (DVB).

In another approach, the inorganic matrix of aerogel is replaced by an organic matrix. In this respect resorcinol-formaldehyde (RF) gels seem to be quite attractive. Typically, RF aerogels are prepared via Pekala's method that involves base (Na_2CO_3)-catalyzed gelation of aqueous solutions of resorcinol with formaldehyde, followed by aging and drying from supercritical fluid (SCF) CO_2 .^{28,29} RF aerogels exhibit high porosity (>80%), high surface area (>400 m^2g^{-1}), ultrafine cell size (<500 Å) and densities as low as 0.03 g cm^{-3} . The major drawback of the base-catalyzed method seems to be the long gelation time, which typically spans over several days. The extensive literature on base-catalyzed RF aerogels overshadows the few reports on acid-catalyzed processes.³⁰⁻³³ We have developed and describe here an HCl-catalyzed gelation process that is completed in minutes rather than days, yielding gels indistinguishable from those obtained by the usual base-catalyzed process in a week. The process has commercial advantage over traditional base catalyzed aerogels.

Also in the spirit of making polymer crosslinked aerogels, these organic backbone resorcinol-formaldehyde gels were crosslinked with isocyanate in analogy to silica wet-gels and resulted in crosslinked RF aerogels with minimal shrinkage. Generally, RF gels are prepared as the precursors for carbon aerogels, which are promising materials for use as electrodes for super capacitors and rechargeable batteries, advanced catalyst supports, adsorbents, thermal insulators, and as new materials for hydrogen storage.³⁴⁻³⁷ Providing either stereoregular (ordered or periodic) mesoporosity or macroporosity (pore diameters > 50 nm) in monolithic carbon or films can be beneficial for applications ranging from fuel cell electrodes to photonic crystals.³⁹⁻⁴⁰ Typically macro-pores are introduced in carbon aerogels by using templating agents during gelation, like for example with monodispersed beads of polystyrene or silica, which are removed from the wet gels later by dissolving in toluene or HF, respectively, or with self-assembled surfactant aggregates, which decompose during carbonization of the surrounding RF matrix.^{41,42}

A method for producing macroporous carbon aerogels by pyrolysis of isocyanate-crosslinked RF aerogels has been developed. During pyrolysis the crosslinker melts before it decomposes, thereby exerting surface tension forces, which transform the mesoporous RF network into a macroporous one that upon carbonization is converted to a new electrically conducting material with morphology and properties different from those of typical carbon aerogels obtained from native (non-crosslinked) RF aerogels. The new macroporous material was evaluated electrochemically for possible application as an electrode in batteries and fuel cells.

REFERENCES

1. Leventis, N. *Acc. Chem. Res.* **2007**, *40*(9), 874-884.
2. Morris, C. A.; Anderson, M. L.; Stroud, R. M.; Merzbacher, C. I.; Rolison, D. R. *Science* **1999**, *284*, 622-624.
3. (a) Hüsing, N; Schubert, U. *Angew. Chem. Int. Ed. Engl.* **1998**, *37*, 22-45. (b) Pierre, A. C.; Pajonk, G. M. *Chem. Rev.* **2002**, *102*, 4243-4265. (c) Fricke, J. *J. Non-Cryst. Solids* **1988**, *100*(1-3), 169-173.
4. Hench, L. L.; West, J. K. *Chem. Rev.* **1990**, *90*(1), 33-72.
5. <http://stardust.jpl.nasa.gov/tech/aerogel.html>, **2008**.
6. (a) Kistler, S. S. *J. Phys. Chem.* **1932**, *36*, 52-64. (b) Kistler, S. S. *Nature*, **1931**, *127*, 741.
7. (a) Smith, D. M.; Stein, D.; Anderson, J. M.; Ackerman, W. *J. Non-Cryst. Solids* **1995**, *186*, 104-12. (b) White, J. F.; *T. Am. Inst. Chem. Eng.* **1942**, *38*, 435-46.
8. Fricke, J.; Emmerling, A. *J. Sol-Gel Sci. Technol.* **1998**, *13*(1-3), 299-303.
9. (a) Pierre, A. C.; Pajonk, G. M. *Chem. Rev.* **2002**, *102*(11), 4243-4265. (b) Schmidt, M.; Schwertfeger, F. *J. Non-Cryst. Solids* **1998**, *225*, 364-368. (c) Reim, M.; Koerner, W.; Manara, J.; Korder, S.; Arduini-Schuster, M.; Ebert, H.-P.; Fricke, J. *Solar Energy* **2005**, *79*(2), 131-139. (d) Pekala, R. W.; Alviso, C. T.; LeMay, J. D. *J. Non-Cryst. Solids* **1990**, *125*(1-2), 67-75.
10. Lu, X.; Wang, P.; Arduini-Schuster, M. C.; Kuhn, J.; Buettner, D.; Nilsson, O.; Heinemann, U.; Fricke, J. *J. Non-Cryst. Solids* **1992**, *145*(1-3), 207-10.
11. Jones, Steven M. *J. Sol-Gel Sci. Technol.* **2006**, *40*(2/3), 351-357.

12. (a) Leventis, N.; Sotiriou-Leventis, C.; Zhang, G.; Rawashdeh, A.-M. M. *Nano Lett.* **2002**, *2*, 957-960. (b) Zhang, G.; Rawashdeh, A.-M. M.; Sotiriou-Leventis, C.; Leventis, N. *Polym. Prepr.* **2003**, *44*, 35-36. (c) Bertino, M. F.; Hund, J. F.; Zhang, G.; Sotiriou-Leventis, C.; Tokuhiro, A. T.; Leventis, N. *J. Sol-Gel Sci. Technol.* **2004**, *30*, 43-48. (d) Zhang, G.; Dass, A.; Rawashdeh, A.-M. M.; Thomas, J.; Council, J. A.; Sotiriou-Leventis, C.; Fabrizio, E. F.; Ilhan, F.; Vassilaras, P.; Scheiman, D. A.; McCorkle, L.; Palczer, A.; Johnston, J. C.; Meador, M. A. B.; Leventis, N. *J. Non-Cryst. Solids* **2004**, *350*, 152-164. (e) Leventis, N.; Palczer, A.; McCorkle, L.; Zhang, G.; Sotiriou-Leventis, C. *J. Sol-Gel Sci. Technol.* **2005**, *35*, 99-105. (f) Leventis, N.; Vassilaras, P.; Fabrizio, E. F.; Dass, A. *J. Mater. Chem.* **2007**, *17*, 1502-1508. (g) Leventis, N.; Mulik, S.; Wang, X.; Dass, A.; Patil, V.; Sotiriou-Leventis, C.; Lu, H.; Churu, G.; Capecelatro, A. *J. Non-Cryst. Solids* **2008**, *354*, 632-644. (h) Leventis, N.; Sotiriou-Leventis, C.; Mulik, S.; Dass, A.; Schnobrich, J.; Hobbs, A.; Fabrizio, E. F.; Luo, H.; Churu, G.; Zhang, Y.; Lu, H. *J. Mater. Chem.* **2008**, *18*, 2475-2482.
13. Brinker, C.; Scherer, G. *Sol-Gel Science: The Physics and Chemistry of Sol-Gel Processing*, Academic Press, Inc. **1990**, 518-546.
14. Gesser, H. D.; Goswami, P. C. *Chem. Rev.* **1989**, *89(4)*, 765-88.
15. Ilhan, F.; Fabrizio, E. F.; McCorkle, L.; Scheiman, D. A.; Dass, A.; Palczer, A.; Meador, M. A. B.; Johnston, J. C.; Leventis, N. *J. Mater. Chem.* **2006**, *16*, 3046-3054.
16. Einarsrud, M.-A.; Nilsen, E.; Rigacci, A.; Pajonk, G. M.; Buathier, S.; Chevalier, B.; Nitz, P.; Ehrburger-Dolle, F. *J. Non-Cryst. Solids* **2001**, *285*, 1- 7.
17. Katti, A.; Shimpi, N.; Roy, S.; Lu, H.; Fabrizio, E. F.; Dass, A.; Capadona, L. A.; Leventis, N. *Chem. Mater.* **2006**, *18*, 285-296.
18. Luo, H.; Lu, H.; Leventis, N. *Mech. Time-Depend. Mater.* **2006**, *10*, 83-111.
19. Capadona, L. A.; Meador, M. A. B.; Alunni, A.; Fabrizio, E. F.; Vassilaras, P., Leventis, N. *Polymer* **2006**, *47*, 5754-5761.
20. Meador, M. A. B.; Capadona, L. A.; McCorkle, L.; Papadopoulos, D. S.; Leventis, N. *Chem. Mater.* **2007**, *19*, 2247-2260.
21. Meador, M. A. B.; Fabrizio, E. F.; Ilhan, F.; Dass, A.; Zhang, G.; Vassilaras, P.; Johnston, J. C.; Leventis, N. *Chem. Mater.* **2005**, *17*, 1085-1098.
22. Leventis N.; Sotiriou-Leventis C. *U.S. Patent Application Publication No. 2004/0132846* (filed 8-18-2002).
23. Fan, X.; Xia, C.; Advincula, R. C. *Langmuir* **2005**, *21*, 2537-2544.

24. Huang, X.; Brittain, W. J. *Macromolecules* **2001**, *34*, 3255-3260.
25. Meier, L. P.; Shelden, R. A.; Caseri, U. W. *Macromolecules* **1994**, *27*, 1637-1642.
26. Prucker, O.; Ruhe, J. *Langmuir* **1998**, *14*, 6893-6898.
27. Prucker, O.; Ruhe, J. *Macromolecules* **1998**, *31*, 592-601.
28. Pekala, R. W. *J. Mater. Science* **1989**, *24*, 3221-3227.
29. Pekala, R. W.; Schaefer, D. W. *Macromolecules* **1993**, *26*, 5887-5893.
30. Merzbacher, C. I.; Meier, S. R.; Pierce, J. R. *J. Non-Cryst. Solids* **2001**, *285*, 210-215.
31. (a) Brandt, R.; Fricke, J. *J. Non-Cryst. Solids* **2004**, *350*, 131-135. (b) Brandt, R.; Petricevic, R.; Pröbstle, H.; Fricke, J. *J. Porous Mater.* **2003**, *10*, 171-178.
32. Baumann, T. F.; Satcher, J. H. Jr.; Gash, A. E. *U.S. Pat. Appl. Pub. No. US 2002/0173554 A1*.
33. Hansch, C.; Leo, A.; Taft, R. W. *Chem. Rev.* **1991**, *91*, 165-195.
34. Yamamoto, T.; Sugimoto, T.; Suzuki, T.; Mukai, S. R.; Tamon, H. *Carbon* **2002**, *40*(8), 1345-1351.
35. Pekala, R. W.; Farmer, J. C.; Alviso, C. T.; Tran, T. D.; Mayer, S. T.; Miller, J. M.; Dunn, B. *J. Non-Cryst. Solids* **1998**, *225*, 74-80.
36. Kabbour, H.; Baumann, T. F.; Satcher, J. H., Jr.; Saulnier, A.; Ahn, C. C. *Chem. Mater.* **2006**, *18*(26), 6085-6087.
37. Chan, K.; Ding, J.; Cheng, S.; Tsang, K. *J. Mater. Chem.* **2004**, *14*(4), 505-516.
38. Liu, R.; Shi, Y.; Wan, Y.; Meng, Y.; Zhang, F.; Gu, D.; Chen, Z.; Tu, B.; Zhao, D. *J. Am. Chem. Soc.*, **2006**, *128*, 11652-11662.
39. Baumann, T. F.; Satcher, J. H. *J. Non-Cryst. Solids*, **2004**, *350*, 120-125.
40. Perpall, M. W.; Perera, K. P. U.; DiMaio, J.; Ballato, J.; Foulger, S. H.; Smith, D. W. J.; *Langmuir* **2003**, *19*, 7151-7156.
41. Gierszal, K. P.; Jaroniec, M. *J. Am. Chem. Soc.* **2006**, *128*, 10026-10027.
42. Tanaka, S.; Katayama, Y.; Tate, M. P.; Hillhouse, H. W.; Miyake, Y. *J. Mater. Chem.* **2007**, *17*, 3639-3645.

PAPER I**CROSSLINKING 3D ASSEMBLIES OF NANOPARTICLES INTO
MECHANICALLY STRONG AEROGELS BY SURFACE-INITIATED FREE
RADICAL POLYMERIZATION**

Sudhir Mulik¹, Chariklia Sotiriou-Leventis^{1,*}, Gitogo Churu², Hongbing Lu^{2,*} and Nicholas Leventis^{1,*}

1. Department of Chemistry, Missouri University of Science and Technology (*formerly, University of Missouri-Rolla*), Rolla, MO 65409
2. Department of Mechanical and Aerospace Engineering, 218 Engineering North, Oklahoma State University, Stillwater, OK 74078

Accepted for Publication in *Chemistry of Materials*.

1. ABSTRACT

Skeletal nanoparticles of porous low-density materials formally classified as aerogels are crosslinked by surface initiated polymerization (SIP) using a new surface-confined bidentate free-radical initiator structurally related to azobisisobutyronitrile (AIBN). Methylmethacrylate, styrene and divinylbenzene are introduced in the mesopores and upon heating at 70 °C, all mesoporous surfaces throughout the entire skeletal framework are coated conformally with a 10-12 nm thick polymer layer indistinguishable spectroscopically from the respective commercial bulk materials. The amount of polymer incorporated in the structure is controlled by the concentration of the monomer in the mesopores, and albeit an up to a three-fold increase in bulk density (up to 0.6-0.8 g cm⁻³) and a decrease in the porosity even down to 40%, the materials remain

mesoporous with average pore diameters increasing from 20 nm in the native samples, to 41 nm and 62 nm in PMMA and polystyrene crosslinked samples, respectively. The new materials combine hydrophobicity with vastly improved mechanical properties in terms of strength, modulus and toughness relative to their native (non-crosslinked) counterparts. The effect of polymer accumulation on the modulus has been also simulated numerically. Being able to use SIP for crosslinking 3D assemblies of nanoparticles comprising the skeletal framework of typical aerogels, paves the way for the deconvolution of crosslinking from gelation (a free radical versus an ionic process, respectively), so that ultimately all gelation and crosslinking reagents will be included together in one pot, leading to great process simplification.

2. INTRODUCTION

Aerogels are open-cell mesoporous foams with a large internal void space (up to >99%), which is responsible for some very attractive bulk properties such as low density, low dielectric constant, low thermal conductivity, high surface area and high acoustic impedance.^{1,2} Unfortunately, those desirable properties come at a cost: aerogels are extremely fragile materials and do not survive long in applications where they experience mechanical stresses. Polymer crosslinked aerogels seem to alleviate those problems while they retain the desirable properties of their native (non-crosslinked) counterparts.

Silica aerogels resulting from a base-catalyzed gelation process of tetramethoxysilane (TMOS) consist of a three-dimensional network of nanoparticles. The fragility of those materials is traced to the interparticle necks. Those are formed naturally upon particle coagulation during gelation and become wider by dissolution and

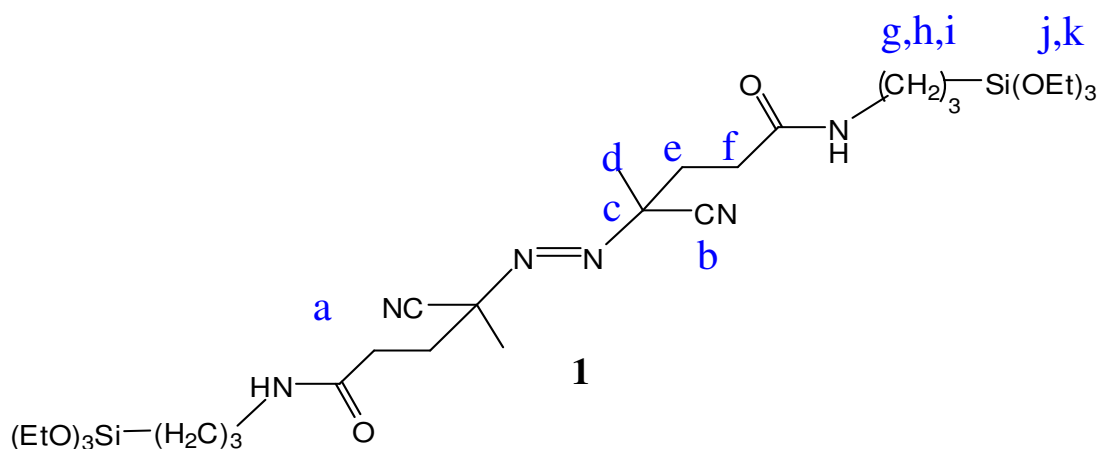
reprecipitation of silica during aging.³ As necks become wider, the mechanical strength of the bulk material increases. This process, however, is self-limiting because dissolution and preferential re-precipitation at the necks cannot go on indefinitely; it will stop as soon as the neck curvature is no longer negative. Inspired by the processes taking place during aging of wet gels, another method by which necks can be reinforced is via post-gelation incorporation of interparticle polymeric tethers bridging and covalently connecting the skeletal nanoparticles. The resulting materials have been referred to as polymer crosslinked aerogels.⁴ Since the reinforcing polymer is confined on the skeletal framework, crosslinked aerogels preserve the porosity and the associated attractive properties of their native counterparts.

Classification-wise, polymer crosslinked aerogels are three-dimensional (3D) core-shell superstructures (as opposed to core-shell single particles) and there are three degrees of freedom in their design: the chemical identity of the framework, the chemical identity of the polymer and the nanoparticle surface functionality. The latter is seemingly the most versatile parameter, because by careful choice of the reactive group on the surface of silica, one can incorporate a variety of polymers. This has been demonstrated for instance with the amine functionality, which has become the point of attachment for polyurea (via reaction with di-isocyanates),⁵⁻⁸ epoxy resins (via reaction with epoxides),⁹ or even polystyrene (PS) after further surface modification with styrene via a lengthy process that involves reaction of dangling amines with *p*-chloromethylstyrene.¹⁰ Crosslinking with isocyanates and epoxides are “grafting from” approaches,¹¹ while crosslinking with PS is a “grafting to” free radical method. “Grafting from” provides the most control over building a shell around a core, because it uses the latter as the central

point of departure for the polymeric chains. Preparation methods of inorganic core/organic shell nanoparticles by the “grafting from” method span the entire range from layer-by-layer electrostatic assembly of oppositely charged materials,¹²⁻¹⁶ to atom-transfer radical polymerization.¹⁷ In order to combine “grafting from” with free radical chemistry, the nanoparticle surface needs to be modified with a free radical initiator, which will induce a so-called surface initiated polymerization (SIP) process. In that regard, peroxide,¹⁸ and azobisisobutyronitrile (AIBN) derivatives¹⁹⁻²¹ have been attached to the surface of silica by ionic interactions, physical adsorption and covalently.²²⁻²⁷ In almost all cases the free radical initiator is monodentate, namely it is attached to the surface of silica by one side only.

For our purpose, namely with an eye on the efficient large-scale production of polymer crosslinked aerogels, scale-up should be considered together with chemical process design. From that perspective, surface initiated free radical crosslinking chemistry is attractive because its precursors can co-exist with the sol-gel precursors and therefore in principle the two processes can be switched on selectively, for example by heat or light, simplifying the crosslinked aerogel preparation process tremendously. This reasoning is akin to ideas advanced in the early 1990’s by Novak in relation to sol-gel materials including interpenetrating polymer networks.²⁸ But, although Novak recognized both the importance of using free radical polymerization for process simplification, and the importance of binding the polymer on the skeletal backbone for avoiding leaching and homogeneity problems, nevertheless he overlooked the possibility of realizing both of those goals and in addition improving the mechanical properties of the composites via surface initiated free radical polymerization.²⁸ Monodentate free-radical initiators have

the disadvantage that upon homolytic cleavage they produce one surface-bound radical and they release a second radical in the solution, initiating homogeneous polymerization whose products will have to be removed later, introducing more processing steps.²⁹ Therefore, in order to stand any chance for one-pot synthesis of crosslinked aerogels, we realized that the free-radical initiator should be bidentate. Thus, here we report the facile synthesis of a bis-triethoxysilane derivative of AIBN (compound **1**), its incorporation on the skeletal nanoparticles of silica wet-gels and the synthesis of mechanically strong polymer crosslinked aerogels by SIP of methylmethacrylate (MMA), styrene and divinylbenzene (DVB). All new materials have been characterized for their macroscopic, microscopic/morphological, chemical as well as their mechanical properties. It turns out that polystyrene and polymethylmethacrylate crosslinked aerogels are among the strongest in that class of materials and possible applications in armor are clearly visible.



3. EXPERIMENTAL

3.1 Materials

All reagents and solvents were used as received unless noted otherwise. Azobiscyanovaleric acid (ABCA), ethylchloroformate, 3-aminopropyltriethoxysilane (APTES), tetramethoxysilane (TMOS), 14.8 N ammonium hydroxide solution as well as polymethylmethacrylate (PMMA, $M_w \sim 90,000$; $M_n = 58,000$) and polystyrene (PS, $M_w \sim 240,000$; $M_n = 120,000$) that were used as standards for ^{13}C CMPAS NMR and for differential scanning calorimetry were all purchased from Aldrich Chemical Co. Triethylamine was obtained from Acros Chemicals and was further purified by distillation over calcium hydride. Anhydrous tetrahydrofuran (THF) was made by pre-drying over NaOH and distilling over lithium aluminum hydride. Styrene, methylmethacrylate (MMA), and divinylbenzene (DVB) were purchased from Aldrich Chemical Co. and were washed with a 5% (w/w) sodium hydroxide solution in water to remove the inhibitor, followed by distillation under reduced pressure. Toluene was purchased from Fisher, and it was purified by stirring overnight with concentrated H_2SO_4 , followed by several extractions with water, pre-drying with Na_2SO_4 followed by a final distillation over phosphorus pentoxide.

3.1.1 Synthesis of 4,4'-(diazene-1,2-diyl)bis(4-cyano-N-(3-(triethoxysilyl)propyl)pentamide) (1)

Azobiscyanovaleric acid (ABCA, 30 g, 0.1070 mol) was dissolved in 650 mL anhydrous THF at room temperature in a jacketed 1 L flask. The solution was maintained under dry and inert conditions (N_2) and the flask was cooled to -76°C by circulating

ethanol using a Neslab's ULT-80 low temperature bath circulator. After 20 min, ethylchloroformate (20.40 mL, 0.2140 mol) and triethylamine (29.75 mL, 0.2140 mol) were added with a syringe through a septum under magnetic stirring. After another 20 min, APTES (49.93 mL, 0.2140 mol) was added also with a syringe. The reaction temperature was raised to -10 °C, and it was maintained for 24 h. At the end of that period, the reaction mixture was allowed to reach room temperature and it was filtered under nitrogen in a glove box. The filtrate was concentrated under reduced pressure, followed by addition of hexane. The precipitate was collected in a dry box under nitrogen, it was recrystallized from THF/hexane twice, and it was dried under vacuum to give pure product **1** (46.14 g, 63% yield), which was stored as a 0.112 M solution in THF in a refrigerator at 10 °C. ¹H NMR δ 6.05 (2 H, br, s), 3.79 (12 H, q, *J* = 7.0 Hz, -OCH₂CH₃), 3.15-3.33 (4 H, m, -CH₂NH), 2.13-2.49 (8 H, m, -CH₂), 1.67 (6 H, s), 1.56-1.66 (4 H, m, -CH₂), 1.20 (18 H, t, *J* = 7.0 Hz, -CH₂CH₃), 0.6 (4 H, t, *J* = 8.0 Hz, -CH₂Si); ¹³C NMR δ 170.1 (C=O), 117.9, 71.8, 58.5, 42.0, 33.9, 31.0, 23.8, 22.7, 18.3, 7.8; IR $\bar{\nu}$ (cm⁻¹) 3430 (m), 2970-2880 (s), 2240 (w), 1640 (s), 1100 (s).

3.1.2 Preparation of native silica aerogels incorporating **1** (native Si-1)

The stock solution of **1** in THF (0.112 M) was allowed to warm to room temperature and an aliquot (11.6 mL, 0.0013 mol) was placed in a round bottom flask. The solvent was removed at room temperature under reduced pressure and the resulting solid was dissolved in a mixture of 4.5 mL of methanol and 3.465 mL of TMOS (0.0234 mol). This is referred to as Solution A. A second solution (Solution B) was made by mixing 4.5 mL methanol, 1.5 mL distilled water and 40 μL 14.8 N NH₄OH. Solution "B"

was added into solution “A,” the mixture was shaken well and it was poured into polypropylene molds (Wheaton polypropylene Omni-Vials, Part No. 225402, 1 cm in diameter), or in 19.6 mm diameter, 20 cm³ polyethylene syringes (samples from the latter were used for compression testing). All solutions gelled within 10-15 min. The resulting wet gels were aged for 24 h at room temperature, they were solvent-exchanged with acetone (3 washes, 8 h per cycle), and they were either dried directly in an autoclave to native aerogels with liquid CO₂ taken out supercritically, or they were crosslinked with different olefins as described below.

3.1.3 Preparation of polymer crosslinked aerogels incorporating 1 (X-Si-1-polymer)

For crosslinking, wet-gels incorporating **1** in acetone were solvent-exchanged with toluene (3 washes, 8 h per wash cycle). The volume of toluene used for each wash cycle was 5× the volume of each gel. Subsequently, toluene-filled wet gels were further washed (3×, 8 h each time) with different monomer solutions in toluene. Again, the volume of the monomer solution used for each wash cycle was 5× the volume of each gel. Gels were then heated in the last monomer solution at 70 °C for 12 h, followed by washing with fresh toluene (3×, 8 h each time) and they were dried using SCF CO₂ in an autoclave.

1) Crosslinking with methylmethacrylate (MMA) into X-Si-1-PMMA: Gels were crosslinked with 10%, 25%, 30%, 40% and 50% v/v solutions of MMA in toluene.

2) *Crosslinking with Styrene into X-Si-1-PS*: In addition to pure styrene, gels were also crosslinked with several different concentrations of styrene in toluene (10%, 25%, 50%, 75% and 100% v/v).

3) *Crosslinking with Divinylbenzene (DVB) into X-Si-1-PDVB*: Gels were crosslinked with 10%, 25% and 50% v/v solutions of DVB in toluene.

3.2 Methods

Supercritical fluid CO₂ drying was conducted using an autoclave (SPI-DRY Jumbo Supercritical Point Drier, SPI Supplies, Inc., West Chester, PA). Bulk densities (ρ_b) were calculated from the weight and the physical dimensions of the samples. Skeletal densities (ρ_s) were determined using helium pycnometry with a Micromeritics AccuPyc II 1340 instrument. Porosities were determined from ρ_b and ρ_s . Porosities of selected crosslinked samples were also determined gravimetrically by dipping them in methylcyclohexane, followed by weighting and determination of the amount of cyclohexane uptaken. Mesoporous surface areas (σ) and pore size distributions were measured by nitrogen adsorption/desorption porosimetry using a Quantachrome Autosorb-1 Surface Area/Pore Distribution analyzer. Samples for surface area and skeletal density determination were outgassed for 24 h at 80 °C under vacuum before analysis. Average pore diameters were determined by the $4 \times V_{\text{Total}} / \sigma$ method, where V_{Total} is the total pore volume per gram of sample. V_{Total} can be calculated either from the single highest volume of N₂ adsorbed along the adsorption isotherm, or from the relationship: $V_{\text{Total}} = (1/\rho_b) - (1/\rho_s)$. The single point N₂ adsorption method tends to underestimate V_{Total} significantly when macropores are involved.³⁰ Table 1 cites average pore diameter values

by both methods and the values agree well, except when macropores are involved (the presence of the latter was confirmed by SEM). The discussion of average pore diameters is based on values calculated using $V_{\text{Total}} = (1/\rho_b) - (1/\rho_s)$. The liquid ^{13}C NMR of compound **1** was recorded using a 400 MHz Varian Unity Inova NMR instrument. Chemical characterization of native and crosslinked silica aerogels was conducted with infrared and solid state ^{13}C and ^{29}Si NMR spectroscopy. Infrared spectra were obtained in KBr pellets using a Nicolet-FTIR Model 750 Spectrometer. Solid ^{13}C NMR spectra were obtained with samples ground in fine powders on a Bruker Avance 300 Spectrometer with 75.475 MHz carbon frequency using magic angle spinning (at 7 kHz) with broad band proton suppression and the CPMAS TOSS pulse sequence for spin sideband suppression. ^{13}C NMR spectra were externally referenced to the carbonyl of glycine (196.1 ppm relative to tetramethylsilane). Thermogravimetric analysis (TGA) was conducted with a TA Instrument, model Hi-Res-TGA 2950, under air and with a heating rate of $10\text{ }^{\circ}\text{C min}^{-1}$. Modulated Differential Scanning Calorimetry (MDSC) was conducted under nitrogen with a TA Instrument Model 2920 apparatus at a heating rate of $10\text{ }^{\circ}\text{C min}^{-1}$. The mass of each sample was approximately 8-12 mg. Samples were subjected to two heating scans and one cooling scan from $30\text{ }^{\circ}\text{C}$ to $250\text{ }^{\circ}\text{C}$. Glass transition temperatures were determined from the second heating scan. Scanning electron microscopy was conducted with samples coated with Au using a Hitachi S-4700 field emission microscope.

Table 1. Selected Properties of **X-Si-1-polymer** (polymer: PMMA, PS or PDVB).

Material	Diameter (cm)	Bulk density, ρ_b (g cm ⁻³)	Skeletal density, ρ_s (g cm ⁻³)	Porosity, Π (% void space)	BET Surf.Area, σ [Av.Pore Dia.] (m ² g ⁻¹ [nm])	Force at failure ^a (N)	Failure Stress ^a (MPa)	Flexural Modulus, E^a (MPa)	Total % mass loss (by TGA)	% polymer (eq 2)
native silica	0.999 ± 0.002	0.169 ± 0.004	1.981 ± 0.017	92	997 [13.40]	b	b	b	4	c
native Si-1	0.910 ± 0.005	0.189 ± 0.005	1.8516 ± 0.008	90	973 [22.78]	b	b	b	21	c
X-Si-1-PMMA from 50% MMA	0.885 ± 0.032	0.807 ± 0.047	1.304 ± 0.001	38	46.05 [31.12]	1057.65 ± 54.15	93.13 ± 5.29	618.54 ± 79.31	77	74
X-Si-1-PMMA from 40% MMA	0.928 ± 0.004	0.436 ± 0.036	1.416 ± 0.002	69	185.7 [36.20]	272.10 ± 49.95	19.79 ± 3.37	64.59 ± 19.44	62	58
X-Si-1-PMMA from 30% MMA	0.850 ± 0.045	0.261 ± 0.013	1.855 ± 0.008	86	740 [24.70]	b	b	b	19	11
X-Si-1-PMMA from 25% MMA	0.968 ± 0.011	0.198 ± 0.028	1.799 ± 0.003	89	787.1 [27.63]	b	b	b	45	21
X-Si-1-PMMA from 10% MMA	0.961 ± 0.014	0.174 ± 0.011	1.798 ± 0.005	90	731.3 [27.70]	0.68 ± 0.10	0.05 ± 0.01	1.08 ± 0.11	24	8
X-Si-1-PS from 100 % Styrene	0.881 ± 0.020	0.549 ± 0.042	1.260 ± 0.001	56	65.98 [43.73]	329.51 ± 32.58	28.86 ± 2.36	192.08 ± 17.98	68	62
X-Si-1-PS from 75 % Styrene	0.909 ± 0.012	0.333 ± 0.014	1.396 ± 0.002	76	160 [33.47]	104.55 ± 14.31	8.10 ± 1.17	27.50 ± 3.92	54	43
X-Si-1-PS from 50 % Styrene	0.931 ± 0.005	0.325 ± 0.008	1.383 ± 0.002	77	183.4 [43.67]	118.55 ± 12.96	8.60 ± 0.94	27.75 ± 2.69	54	46
X-Si-1-PS from 25 % Styrene	0.925 ± 0.003	0.232 ± 0.016	1.744 ± 0.005	87	620 [27.69]	14.90 ± 5.38	1.09 ± 0.39	7.81 ± 0.78	40	22
X-Si-1-PS from 10 % Styrene	0.963 ± 0.036	0.200 ± 0.031	1.739 ± 0.003	89	668.3 [28.69]	1.44 ± 0.41	0.09 ± 0.03	1.30 ± 0.12	24	20
X-Si-1-PDVB from 50% DVB	0.888 ± 0.011	0.795 ± 0.015	1.246 ± 0.001	36	247.0 [5.60]	11.90 ± 3.23	0.99 ± 0.31	50.96 ± 18.45	69	74
X-Si-1-PDVB from 25% DVB	0.919 ± 0.005	0.310 ± 0.005	1.437 ± 0.003	78	530.2 [13.74]	11.40 ± 1.87	0.85 ± 0.15	17.99 ± 0.86	52	41
X-Si-1-PDVB from 10% DVB	0.986 ± 0.008	0.276 ± 0.002	1.624 ± 0.003	83	731.4 [20.24]	n/a	n/a	n/a	34	46

a. By a short beam three point flexural bending method, values are averages of 5 samples. b. Too weak to measure. c. Not applicable.

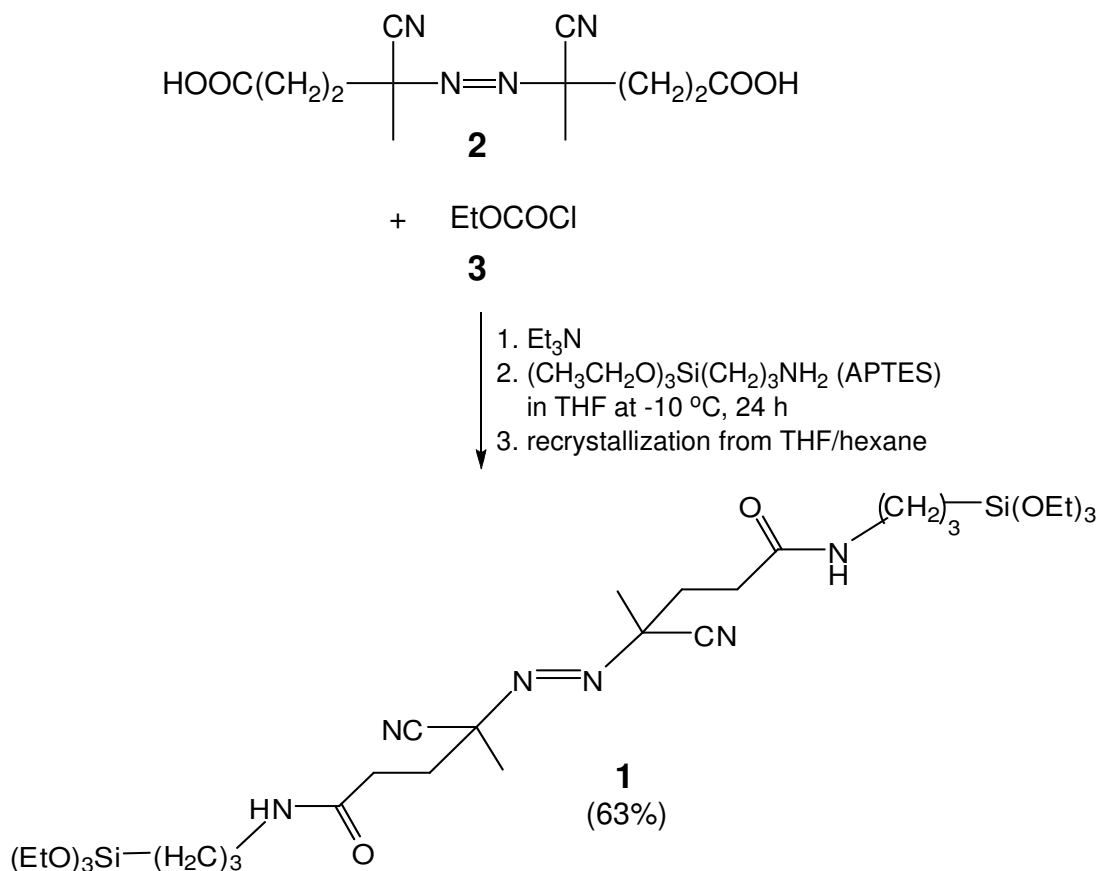
Three-point flexural bending tests were performed according to ASTM D790, Procedure A (Flexural Properties of Unreinforced and Reinforced Plastics and Electrical Insulating Materials), using an Instron 4469 universal testing machine frame with a 2 kN load cell (Instron part number 2525-818) and a three-point bend fixture, with 22.9 mm span and 25 mm roller diameter (Instron part number 2810-182). Typical samples were cylindrical, ~1 cm in diameter and ~ 4 cm in length. Glass transition temperatures were determined from the second heating scan. Scanning electron microscopy was conducted with samples coated with Au using a Hitachi S-4700 field emission microscope. Three-point flexural bending tests were performed according to ASTM D790, Procedure A (Flexural Properties of Unreinforced and Reinforced Plastics and Electrical Insulating Materials), using an Instron 4469 universal testing machine frame with a 2 kN load cell (Instron part number 2525-818) and a three-point bend fixture, with 22.9 mm span and 25 mm roller diameter (Instron part number 2810-182). Typical samples were cylindrical, ~1 cm in diameter and ~ 4 cm in length. The crosshead speed was set at 1.0 mm min^{-1} .^{4b,4e} Compression testing was performed according to the ASTM D695-02a standard on cylindrical specimens, using a MTS machine (Model 810) equipped with a 55000 lb load cell, as described previously.⁵ According to the ASTM standard, the height-to-diameter ratio of the specimen should be 2:1; typical samples were ~1.5 cm in diameter, 3 cm long.

4. RESULTS AND DISCUSSION

4.1 Synthesis, incorporation of **1** in mesoporous silica and preparation of polymer crosslinked aerogels

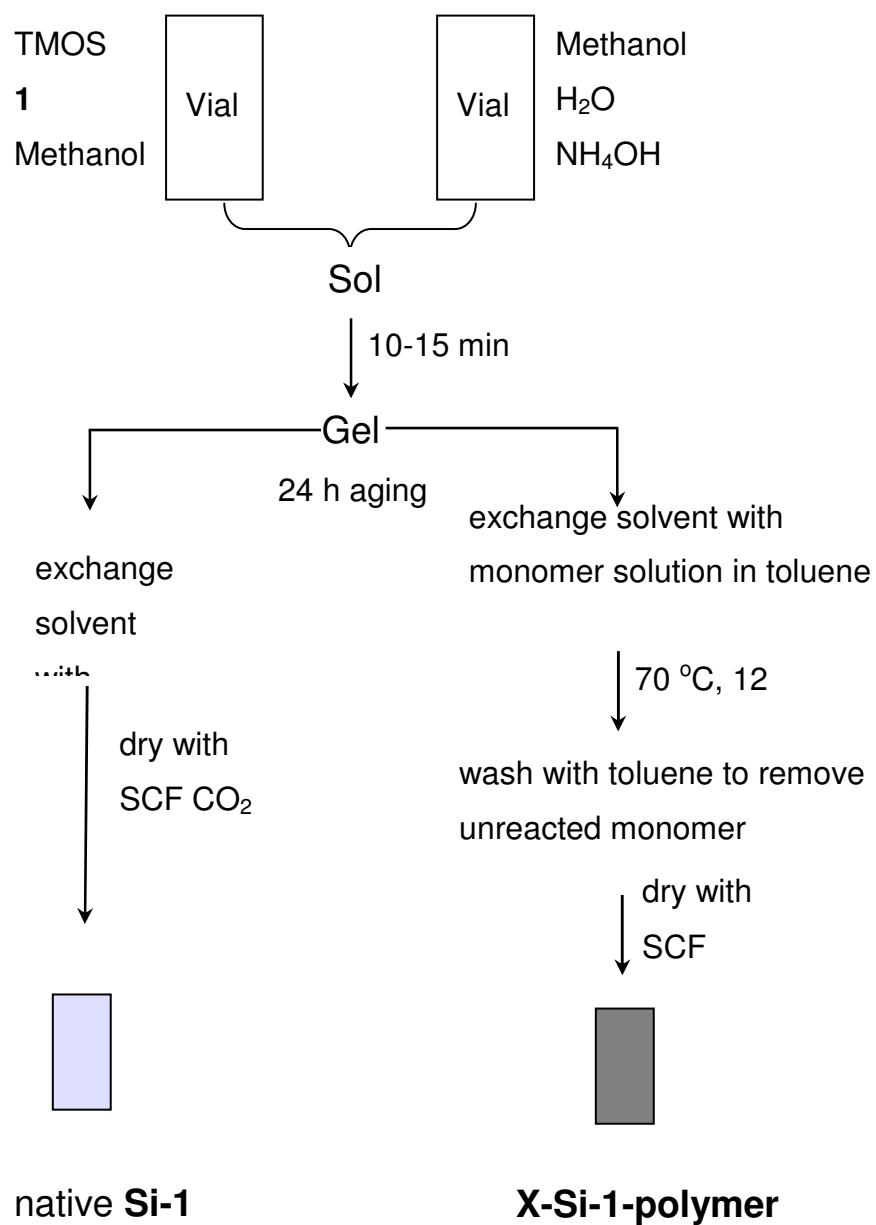
Typically, skeletal nanoparticles of silica aerogels are provided with functionality by co-gelation of tetramethoxy- or tetraethoxysilane (TMOS or TEOS, respectively) with appropriately modified trimethoxy- or triethoxysilanes.² In the same context, skeletal nanoparticles of base-catalyzed aerogels are modified with a bidentate free radical initiator by co-gelation of TMOS and **1**. The latter was synthesized in one pot according to Scheme 1 by activation of commercially available azobiscyanovaleric acid (**2**) with ethyl chloroformate (**3**) followed by amidization with 3-aminopropyltriethoxysilane (APTES).³¹ Two recrystallizations are necessary for removing acid impurities, which otherwise react and deactivate the base catalyst (NH₄OH) used in the gelation process. Product **1** is sensitive to moisture and tends to self-condense. To prolong its shelf-life (up to 2-3 weeks), facilitate handling and standardize processing, **1** was stored as a 0.112 M solution in anhydrous THF at 10 °C.

As with APTES, attempts to induce gelation of **1** by itself were not successful, probably because interference of its side chain with the Si-O-Si network formation. Thus, we resorted to co-gelation of **1** with TMOS (Scheme 2). The concentration of **1** was kept low (mol ratio of TMOS:**1** = 18:1) in order to reduce the initiation events and thus obtain crosslinking tethers with higher molecular weight.³³ Under those conditions gelation occurs in 10-15 min, which is not different from the gelation of TMOS by itself.³⁴

Scheme 1. Preparation of the bidentate initiator **1**.

Crosslinking was carried out by first filling the mesopores of the wet gels with various toluene solutions of inhibitor-free monomers (MMA, styrene or DVB), and subsequently by heating the samples at 70 °C for 12 h (Scheme 2). Unreacted monomer, and polymer formed in the mesopores by possible chain transfer processes were washed off with toluene and crosslinked monoliths were dried in an autoclave with CO₂ taken out supercritically at the end. Special attention has been paid for internal consistency throughout the process. Polymer crosslinked aerogels are denoted as **X-Si-1-polymer**, where the polymer is either PMMA, PS, or PDVB.

Scheme 2. Preparation of native silica aerogels incorporating **1** (native **Si-1**) and crosslinking with MMA, styrene or DVB into **X-Si-1-polymer**



4.2 Physical, chemical and morphological characterization of native and crosslinked aerogels

Key properties of all materials prepared for this study are summarized in Table 1.

4.2.1 Native silica aerogels incorporating **1** (Native Si-1)

Although the mol-content of **1** in **Si-1** is low (5.6%), the percent weight of **1** in native **Si-1** (assuming complete hydrolysis and condensation of all alkoxy groups of both TMOS and **1**) is relatively high (30.1% w/w – refer also to the discussion of TGA at the end of this section). Presence of **1**, however, does not seem to have an adverse effect on the samples in terms of their macroscopic appearance, bulk density and nanomorphology, compared to samples prepared with TMOS only using the same total mol silica content as in **Si-1**. (Data for such TMOS-only aerogels are also included in Table 1 for comparison.) SEM (Figure 1A) shows that native **Si-1** possesses the characteristic particulate structure of base-catalyzed mesoporous silica, where primary particles are the smallest entities discernible (two are pointed by arrows) and secondary particles consist of larger agglomerations of primary particles (one is shown in a circle). N₂ sorption porosimetry gives Type IV isotherms, characteristic of mesoporous materials (Figure 2A).³⁵ The BET surface area, σ , is similar to that of TMOS-only samples (~970 m²g⁻¹; refer to Table 1).^{4a,4b} Based on the relationship $r=3/\rho_s\sigma$ (where, r : nanoparticle radius; and, ρ_s : skeletal density of the native **Si-1** aerogels),³⁶ it is calculated that the nanoparticle diameter is 3.32 nm, corresponding to the primary particles.

The porosity, Π , calculated from bulk and skeletal densities according to eq 1,

$$\Pi = \frac{1/\rho_b - 1/\rho_s}{1/\rho_b} \times 100\% \quad (1)$$

indicates that native **Si-1** aerogels consist of 90% empty space. The average pore diameter is ~20 nm (by the $4 \times V_{\text{Total}} / \sigma$ method, where $V_{\text{Total}} = (1/\rho_b) - (1/\rho_s)$) and the pore-size distribution at half width is ~40 nm (Figure 2A, inset). The incorporation of **1** in the skeletal framework is confirmed spectroscopically. Indeed, the infrared (IR) spectrum of **1** is dominated by the absorption of the amide C=O stretch at 1640 cm^{-1} and the aliphatic C-H stretches in the $2970\text{-}2880 \text{ cm}^{-1}$ range (Figure 3). The broad absorption at $\sim 3500 \text{ cm}^{-1}$ (O-H stretch) is probably due to some hydrolysis of terminal $-\text{Si}(\text{OCH}_2\text{CH}_3)_3$ groups, while the weak $\text{C} \equiv \text{N}$ stretch appears at 2240 cm^{-1} . Now, the IR spectrum of native **Si-1** is dominated by the characteristic Si-O stretch of silica at 1100 cm^{-1} and by the broad absorption of surface -OHs in the 3500 cm^{-1} range; the C=O stretch at 1640 cm^{-1} is the only feature of **1** that is still clearly visible in **Si-1**. ^{13}C CPMAS NMR spectra of native **Si-1** aerogels show the carbonyl resonance at 173 ppm and resonances from several aliphatic carbons (Figure 4). The $-\underline{\text{C}}\text{N}$ carbon at 117 ppm is barely visible, while resonances at 16 and 58 ppm (marked with asterisks) correspond to a small amount of unhydrolyzed ethoxy groups, and the peak at 58 ppm (also marked with an asterisk) corresponds to residual methoxy groups from TMOS. (The sharp peak at 29.2 ppm is likely due to residual solvent -acetone- in the aerogel.) However, the most compelling evidence for the incorporation and covalent attachment of **1** comes from ^{29}Si CPMAS NMR (Figure 5). Thus Figure 5A shows the spectrum of a TMOS-only native silica aerogel: the trimodal resonance between -90 and -110 ppm is assigned to Q^4 (-108 ppm), Q^3 (-99 ppm) and Q^2 (-90.3 ppm) silicon atoms, participating in four, three and two Si-O-Si bridges, respectively.^{37,38} Figure 5B shows that the relative intensity for the Q^2 silicon

atoms in **Si-1** aerogels has been reduced, and the new resonances between -50 and -70 ppm are characteristic of T^{3-n} species ($n=0-2$) confirming incorporation of **1**.

In principle, **1** could have been partly buried in the interior of the particles. However, based on the fact that hydrolysis of TMOS is expected to be faster than hydrolysis of trialkoxysilanes,^{2,36} the probable location of **1** is at the surface of the TMOS-derived nanoparticles. This is consistent with the similar morphology shared by TMOS-only native silica and native **Si-1**. Now, in analogy to AIBN, upon heating, **1** undergoes a sharp mass loss (by TGA, Figure 6A) of ~5% w/w at ~120 °C, attributed to loss of N_2 (versus a theoretical mass loss of 4.08% w/w). The gradual mass loss preceding the sharp decomposition is probably due to residual THF in the sample. Native **Si-1** aerogels also show a TGA step below 120 °C (indicated by an arrow in Figure 6A, Inset), which again is assigned to loss of N_2 leaving behind two surface-bound radicals. Finally, in agreement with the expected residual inorganic weight of native **Si-1** (79.8 %) calculated assuming complete hydrolysis and condensation of the 18:1 mol ratio of TMOS:**1** in the sol, the overall TGA mass loss of native **Si-1** up to 750 °C is 21%.

4.2.2 Silica aerogels crosslinked with PMMA (X-Si-1-PMMA), PS (X-Si-1-PS) and PDVB (X-Si-1-PDVB)

All monoliths based on **X-Si-1-polymer** are opaque, white and hydrophobic. Figure 7 shows water droplets on flat surfaces created by cutting crosslinked cylinders vertical to their axis with a diamond saw. The contact angles on **X-Si-1-PMMA** and **X-Si-1-PS** are $72.6 \pm 1.3^\circ$ and $114.1 \pm 0.3^\circ$, respectively, indicating that the latter material is more hydrophobic than the former, as expected. For comparison, the contact angle of

water on PS-crosslinked samples by the “grafting to” method was 121°. ¹⁰ Overall, in terms of hydrophobicity “grafting to” and “grafting from” methods yield similar results; however, for reasons outlined in the Introduction, “grafting from” has certain distinct advantages.

The bulk density (ρ_b) of the three kinds of materials under **X-Si-1-polymer** depends on the chemical identity and the concentration of the monomer during incubation. All data have been summarized in Table 1. The amount of the polymer uptake is calculated either via the mass loss between 300 °C and 400 °C in TGA (Figure 6B), or via eq 2 that takes into consideration changes in density and volume after crosslinking.

$$\text{Polymer weight percent} = \left[1 - \left[\left(\frac{\text{diameter}_X}{\text{diameter}_{\text{native}}} \right)^3 \left(\frac{\rho_{b,X}}{\rho_{b,\text{native}}} \right) \right]^{-1} \right] \times 100 \quad (2)$$

The two methods yield comparable results, although TGA tends to give somewhat higher polymer contents, probably because it does not differentiate between polymer and residual organic material from TMOS and **1** (see discussion of ¹³C NMR data of native **Si-1** above). At any rate, the polymer content in the most dense samples of all three systems falls in the 60-75% w/w range. Now, it is noted that **X-Si-1-PMMA** samples prepared in 50% v/v MMA/toluene are more dense than **X-Si-1-PS** samples crosslinked in pure styrene. Similarly, **X-Si-1-PDVB** crosslinked in 50% v/v DVB are more than twice as dense as **X-Si-1-PS** crosslinked in 50% v/v styrene. These observations are attributed mainly to the higher stability (lower reactivity) of the styrene benzyl radicals. ³⁹ Furthermore, MMA may also develop hydrogen bonding with silanols on the silica surface creating a local high concentration of monomer in the vicinity of the initiator leading to faster accumulation of polymer. Now, for the same crosslinker (MMA, styrene

or DVB), as the monomer concentration increases, the bulk density (ρ_b) of the composite also increases while the skeletal density (ρ_s) decreases. Porosities were again calculated via eq 1 and selected values have been cross-checked gravimetrically, by weighting samples before and after dipping in cyclohexane (see Table 1). Porosities by the He pycnometry and the cyclohexane uptake methods agree within 3-7% from one another. Porosities correlate with the bulk densities for all three composites independently of the chemical identity of the polymer involved (Figure 8). This is consistent with a material with polymer confined and coating conformally a common skeletal nanostructure. The actual porosity values for the more dense composites are significantly reduced compared to the values of native silica: 36-38% for **X-Si-1-PMMA** ($\rho_b=0.807 \text{ g cm}^{-3}$) and **X-Si-1-PDVB** ($\rho_b=0.795 \text{ g cm}^{-3}$), versus a porosity of 90% for native **Si-1** ($\rho_b=0.189 \text{ g cm}^{-3}$). Despite the apparent reduction in void space, N_2 -sorption isotherms remain Type IV, indicating that the samples are still mesoporous (Figures 2B and 2C). Nevertheless, the BET surface area has been reduced upon crosslinking, from $973 \text{ m}^2 \text{ g}^{-1}$ for **Si-1** to $46 \text{ m}^2 \text{ g}^{-1}$ and $66 \text{ m}^2 \text{ g}^{-1}$ for **X-Si-1-PMMA** and **X-Si-1-PS** with $\rho_b = 0.807 \text{ g cm}^{-3}$ and 0.549 g cm^{-3} , respectively. At the same time, the average pore diameters of the same samples have been increased relative to native **Si-1** (to 41 nm and 63 nm for **X-Si-1-PMMA** and **X-Si-1-PS**, respectively, vs. 20 nm for **Si-1**). Similarly, the average particle diameter (by the $r=3/\rho_s\sigma$ method) is 100 nm and 72 nm for **X-Si-1-PMMA** and **X-Si-1-PS**, respectively (versus an average particle diameter in native **Si-1** before crosslinking of 3.32 nm, which represents the primary particles – refer to Section 3.2.a above.) Pore diameters and particle size calculations based on N_2 sorption porosimetry indicate that new material (i.e., polymer) accumulated on the skeletal nanoparticles blocks access of

the probe gas (N_2) to the smallest crevices of the native skeletal framework. Thus, in native **Si-1** N_2 sorption samples the primary particles while in **X-Si-1-PMMA** and **X-Si-1-PS** it samples the secondary ones. Also, another point worth noting is that while the average pore diameter of the **X-Si-1-PMMA** samples is still in the mesoporous range (<50 nm), the average pore diameter of the **X-Si-1-PS** samples is slightly over the upper limit of that range, falling into what is considered macropores. SEM corroborates with this model (Figures 1B and 1C); what is observed is that first, an open mesoporous structure is still preserved despite the heavy polymer loading; second, secondary particles are also clearly visible, but in agreement with our previous studies,⁴ the fine definition of the primary particles has been erased by the polymer coating; and third, **X-Si-1-PS** samples include macropores. It is speculated that the presence of the latter is the result of the stresses imposed on the skeletal framework by the mechanism of crosslinking, which in turn is related to the free radical chain termination step (see below).

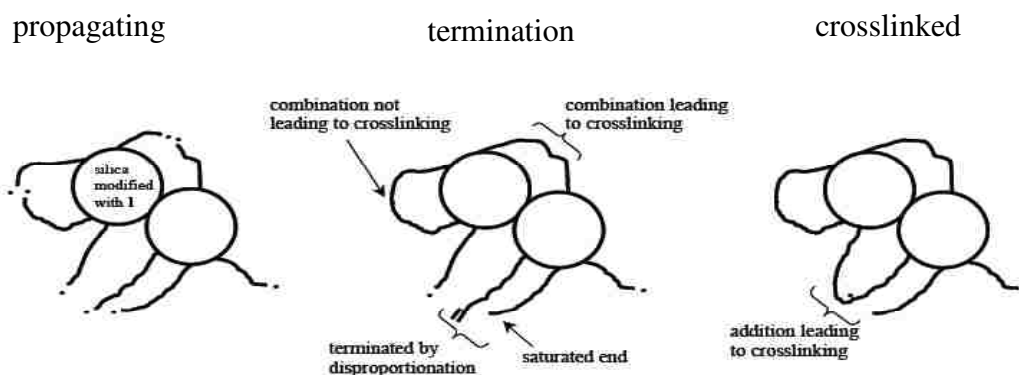
Spectroscopically, the IR features from silica at 1100 cm^{-1} (Si-O stretch) and at $\sim 3500\text{ cm}^{-1}$ (O-H stretch) and from PMMA at 1730 cm^{-1} (ester C=O stretch) and at $3000\text{--}2800\text{ cm}^{-1}$ (aliphatic C-H stretch) dominate the spectrum of **X-Si-1-PMMA**, while the amide stretch of the initiator at 1640 cm^{-1} is still visible (Figure 3). Similarly, **X-Si-1-PS** shows the characteristic absorption bands from PS and silica (Figure 3). The ^{29}Si NMR spectra of **X-Si-1-PMMA** (and **-PS**) are practically identical to the spectra of native **Si-1** (Figures 5C and 5D) as expected from the fact that radical formation and crosslinking should not alter the chemical adhesion of the initiator on the surface. On the other hand, ^{13}C CPMAS NMR provides the most direct evidence for the involvement of the surface-bound initiator in anchoring the crosslinker (Figure 4). If the monomer concentration in

the crosslinking bath (and the mesopores) is kept low (e.g. 10% v/v), the intensity of the polymer peaks remains low, while resonances owing to the surface bound initiator are still clearly visible. Thus, the initiator resonance at 72.27 ppm, which corresponds to the tertiary radical carbon, disappears completely even with small monomer concentrations, while a new resonance at ~19 ppm (pointed at by an arrow) corresponds to the same carbon after it has been added to the β -carbon of MMA or styrene. No new resonances in the aromatic range become evident, signifying no incorporation of toluene through possible chain transfer processes. At high monomer concentrations, all spectra are dominated by the corresponding polymers and they are indistinguishable from the spectra of commercially available pure materials (also shown for comparison). At high monomer concentrations, most of the resonances associated with the initiator are either buried underneath the strong resonances of the polymer, or remain visible albeit extremely weak (case of $\underline{\text{C}}\text{N}$ in **X-Si-1-PMMA**).

Obviously, polymerization proceeds by addition of surface-bound radicals to monomer from the solution filling the mesopores. Radicals at the tips of polystyrene chains are expected to terminate by combination, bridging particles directly.⁴⁰ However, radicals at the tips of propagating PMMA chains will terminate mostly by disproportionation, yielding a saturated group and a new terminal olefin.⁴⁰ Addition of a radical at the tip of a neighboring propagating PMMA chain to the newly formed terminal double bond leads to interparticle bridge formation and crosslinking. These processes are summarized in Scheme 3. It is plausible then that chains terminated by combination (case of PS) impose tensile stresses on their nanoparticle end-caps pulling the framework apart, creating macropores.

Finally, we have not been able to separate reproducibly the polymers from silica by treating **X-Si-1-polymer** with HF. Therefore, attempts to determine average molecular weights of surface bound polymers by gel permeation chromatography (GPC) were inconclusive. However, an upper and a lower limit for the polymer chain length can be calculated for PS in **X-Si-1-PS**, because that polymer is expected to be linear and terminated by two molecules of surface-bound initiator. Thus, based on the bulk density of **Si-1** ($\rho_b=0.189 \text{ g cm}^{-3}$) and the 18:1 mol ratio of TMOS:**1** in the sol (or 30.0% w/w of **1** in native **Si-1**), it is first calculated that the skeletal framework contains 1.22×10^{-4} mol of initiator per cm^3 of native **Si-1**. Next, the amount (mol) of styrene included in one cm^3 of **X-Si-1-PS** can be calculated based on the bulk density increase between native **Si-1** and crosslinked samples (the minor crosslinking shrinkage is ignored). At this point, there are two ways to calculate the number of styrene monomers per polymer chain: either by assuming that all initiator **1** is engaged in initiation events and therefore it finds itself bound at the ends of polymer chains, or by assuming that only the fraction of the initiator that is located on the outer surface of the secondary particles is able to create interparticle tethers. An estimate of the latter is obtained from the ratio of the BET surface area after crosslinking over the surface area of native **Si-1**. Thus, it is calculated that PS tethers consist of between 57 and 836 styrene monomer units. Evidently, in comparison with our previous “grafting to” free radical crosslinking method that yielded PS-crosslinked samples of $\rho_b \sim 0.46 \text{ g cm}^{-3}$ with 15 monomer units of styrene per polymer chain,¹⁰ the present “grafting from” method yields much longer polymers.

Scheme 3. Crosslinking through termination of chain reactions initiated by a bidentate free radical initiator on the mesoporous surfaces of 3D assemblies of silica nanoparticles



Interparticle polymer chains are expected to criss-cross and be stacked on top of one another, but according to SEM the conformal polymer layer should be very thin. Prior experience with this class of materials has shown that TEM is not a reliable tool to differentiate the polymer coating from the silica core.^{41,42} On the other hand, we are aware that the restricted mobility of polymeric layers in close proximity to surfaces brings about an increase in their glass transition temperatures (T_g).⁴³ Indeed (Figure 9) the T_g of PMMA is shifted from 110 °C for the pure isotactic polymer to 127 °C in **X-Si-1-PMMA** ($\rho_b=0.807$ g cm⁻³). Similarly, the T_g of PS is shifted from 95 °C to 108 °C in **X-Si-1-PS** ($\rho_b=0.549$ g cm⁻³). Those shifts are similar to those reported for polymer brushes made by surface initiated polymerization of MMA and styrene.^{44,45} In particular, according to Yamamoto *et al.*,⁴⁵ an increase of T_g in the order of 17 °C would correspond to a film thickness of ~10-12 nm. In turn, this corresponds to 9-11 layers of fully stretched PMMA with a van der Waals chain diameter of 1.15 nm (by modeling). In fact that film is what seals access to the space between primary particles, and thus the average

particle size as determined by N₂ sorption data increases from 3.32 nm in native **Si-1** to over 70 nm in **X-Si-1-PMMA** and **X-Si-1-PS**.

4.2.3 Mechanical properties of X-Si-1-polymer

As discussed in the introduction, practical use of aerogels has been hampered mainly by their fragility. Hydrophilicity also plays a negative role in strength: adsorbed water satisfies the dangling bonds created by Si-O-Si bridge breaking during crack propagation. Aerogels crosslinked with isocyanates and epoxides by the “grafting from” method are mechanically much stronger materials than native aerogels, but they are not hydrophobic.¹⁰ Aerogels crosslinked with polystyrene (and pentafluorostyrene) by the “grafting to” method are hydrophobic but not as strong mechanically as their isocyanate and epoxy counterparts.¹⁰ In order to keep our methodology internally consistent with our previous studies, the mechanical properties of selected aerogel samples crosslinked by the “grafting from” method of this study were tested by two methods: (a) a short beam three point flexural bending method; and, (b) a quasi-static compression testing method, as described in the Experimental section. In the first method, we employed samples of the same dimensions to those used previously for testing isocyanate and epoxy crosslinked samples (i.e., cylinders, *ca.* 5 cm in length, *ca.* 1 cm in diameter). As shown in Figure 10A, the most dense samples of **X-Si-1-PMMA** and **X-Si-1-PS** fail with several hundreds Newton, which is comparable with the values we have reported for isocyanate and epoxy crosslinked samples of similar densities.^{4e,10} For example, **X-Si-1-PMMA** with $\rho_b = 0.436 \text{ g cm}^{-3}$ fail with 270 N and **X-Si-1-PS** with $\rho_b = 0.549 \text{ g cm}^{-3}$ fail with 330 N (Table 1). Under the same configuration, isocyanate crosslinked base-catalyzed silica

samples of the same geometry having $\rho_b = 0.48 \text{ g cm}^{-3}$ fail with 190 N,^{4e} and “grafting to” PS-crosslinked samples with ρ_b in the range of 0.42-0.48 g cm^{-3} are much weaker, failing with only 42-72 N.¹⁰ Even “grafting to” PS-crosslinked samples with higher bulk densities (ρ_b in the range of 0.6-0.7 g cm^{-3}) still fail more easily with $\sim 150 \text{ N}$.^{4e}

From the short beam bend testing method with cylindrical samples, the flexural modulus, E , a measure of stiffness, is calculated via eq 3 and results are cited in Table 1

$$E = \frac{SL^3}{12\pi R^4} \quad (3)$$

(S is the slope of the linear –elastic– part of the load-deformation curve, L is the span and R is the sample radius).⁴⁶ **X-Si-1-polymer** samples with bulk densities similar to those of samples crosslinked with isocyanates, epoxies and “grafting to” polystyrene seem to have similar stiffness. This is because increasing the particle diameter of any two-particle system by accumulating material (polymer) on their surface increases their resistance to bending (see Scheme 4 for a qualitative description, and the Supporting Information for computer simulations of that effect). In that regard, similar bulk densities correspond to similar amounts of polymer accumulated on the skeletal nanoparticles, increasing resistance to bending by more or less the same amount. On the other hand, the increased strength by the present “grafting from” method vs. the polystyrene “grafting to” method is attributed to more effective interparticle tethering (crosslinking).

Under compressive stress (Figure 10B), **X-Si-1-polymer** samples are again decisively stronger than all previously tested isocyanate crosslined samples that rely on base-catalyzed silica of similar skeletal morphology.^{5,6} All stress-strain curves show a linear elastic region at small compressive strains (<6-8%), then exhibit yield behavior (up

to ~50% strain), followed by densification and inelastic hardening (Figure 10B). Samples do not buckle or bend during compression and the Poisson's ratio remains low (0.18).

Scheme 4. The effect of a conformal polymer coating on the stiffness of a two-particle system

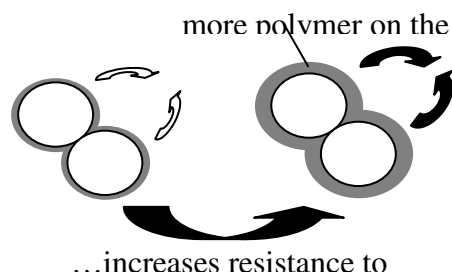


Figure 11 shows **X-Si-1-PMMA** and **X-Si-1-PS** samples before and after compression; samples turned transparent after compression at 96% strain, signifying a compact material with no voids that would scatter light. Typically, **X-Si-1-PS** with $\rho_b \sim 0.46 \text{ g cm}^{-3}$ show a compressive yield strength (the offset yield strength at 0.2% compressive strain) equal to 7.2 MPa, a compressive stress of 263 MPa at strain 86%, and a Young's modulus, E , of 148 MPa. (By comparison, isocyanate crosslinked samples with $\rho_b \sim 0.48 \text{ g cm}^{-3}$ show a compressive yield strength of 4.3 MPa, a compressive stress of 186 MPa at ~77% strain, and a Young's modulus of 129 MPa.^{5,6}) Remarkably, **X-Si-1-PMMA** samples with $\rho_b \sim 0.66 \text{ g cm}^{-3}$ show a compressive yield strength of 36.1 MPa, a compressive stress of 730 MPa at 96% strain (samples never broke into fragments), and a Young's modulus of 908 MPa. The specific energy absorption of about 194 J g^{-1} surpasses even that of the spider dragline silk (165 J g^{-1} , albeit under tension), which is considered as the toughest natural material.⁴⁷ In fact, the mechanical properties of **X-Si-1-PMMA** are similar to those of isocyanate-crosslinked vanadia as well as surfactant-

templated, acid-catalyzed sol-gel silica that possess totally different structural morphologies from what we have seen so far with **X-Si-1-polymer**, consisting of entangled nanoworms rather than nanoparticles.^{41,42,48} For instance, one such kind of material (**X-MP4-T045**) with $\rho_b \sim 0.67 \text{ g cm}^{-3}$ shows a compressive yield strength of 15.2 MPa, a compressive stress at failure equal to 804 MPa at 85% strain and a Young's modulus of 274 MPa, which are values practically identical to those of **X-Si-1-PMMA** of similar density. The increased strength of crosslinked aerogels consisting of nanoworms rather than nanoparticles has been attributed to a synergistic effect, whereas polymer crosslinking reinforces the contact points (necks) between the nanoworms, which hold the structure together even after several individual contacts between nanoparticles may have been broken. It is plausible that long interparticle polymer chains have a similar effect.

5. CONCLUSIONS

Casting a conformal polymer coating on 3D assemblies of sol-gel nanoparticles comprising the skeletal framework of a typical aerogel, results in new materials with greatly enhanced mechanical strength. The process is referred to as crosslinking and the materials as crosslinked aerogels. However, so far both the sol-gel and the crosslinking processes have been ionic, and therefore their reagents could not coexist. Hence, they have been introduced in tandem, adding time-consuming processing steps. In an effort to deconvolute the crosslinking from the gelation process, we synthesized the bidentate free radical initiator **1** and we incorporated it in sol-gel silica. Surface initiated polymerization (SIP) of MMA, styrene or DVB by **1** results in conformal polymer coatings on the

skeletal nanoparticles yielding mechanically very strong, hydrophobic materials. A clearly visible application for those new materials is in armor: with a relatively low modulus (e.g., $E=148$ MPa) and density ($\rho_b=0.46$ g cm³), it is calculated that the speed of sound ($c=(E/\rho_b)^{1/2}$) through **X-Si-1-PS** is $c=635$ m s⁻¹. The latter is very low for a solid material and therefore highly desirable, because it will extend the duration of an impact, thereby reducing the effective force on the material. The relatively low yield stress (7.2 MPa for **X-Si-1-PS** with $\rho_b=0.46$ g cm³) allows early activation of the energy absorption mechanism, while the long stress plateau allows for large energy absorption. The specific energy absorption at low strain rates that was reported above is 194 J g⁻¹; that value is much higher than that of polymethylacrylamide or Rohacell[®] foams that can achieve specific energy absorptions up to 35 J g⁻¹, which is often considered a high value.⁴⁹ Finally, although this research effort has been focused on aerogels, SIP with **1** paves the way for more innovative research at the interface of the sol-gel and polymer chemistry. Examples include improving adhesion of coatings, and more efficient preparation of covalently bonded, completely randomized 3D dispersions of nanoparticles as fillers in plastics.

6. ACKNOWLEDGMENTS

We acknowledge the University of Missouri Research Board (N.L.) and the NSF under CMMI-0653919 and CMMI-0653970 for financial support. We also thank Dr. Wei Wycoff for her assistance with solids NMR and Professor Douglas K. Ludlow for his assistance with N₂ adsorption porosimetry. We also thank Mr. Nitin P. Daphalapurkar for conducting the finite elemental analysis of two connected secondary silica nanoparticles.

7. REFERENCES

1. Morris, C. A.; Anderson, M. L.; Stroud, R. M.; Merzbacher, C. I.; Rolison, D. R. *Science* **1999**, *284*, 622-624.
2. (a) Hüsing, N.; Schubert, U. *Angew. Chem. Int. Ed. Engl.* **1998**, *37*, 22-45. (b) Pierre, A. C.; Pajonk, G. M. *Chem. Rev.* **2002**, *102*, 4243-4265.
3. Einarsrud, M.-A.; Nilsen, E.; Rigacci, A.; Pajonk, G. M.; Buathier, S.; Valette, D.; Durant, M.; Chevalier, B.; Nitz, P.; Ehrburger-Dolle, F. *J. Non-Cryst. Solids* **2001**, *285*, 1-7.
4. (a) Leventis, N. *Acc. Chem. Res.* **2007**, *40*, 874-884. (b) Leventis, N.; Sotiriou-Leventis, C.; Zhang, G.; Rawashdeh, A.-M. M. *Nano Lett.* **2002**, *2*, 957-960. (c) Zhang, G.; Rawashdeh, A.-M. M.; Sotiriou-Leventis, C.; Leventis, N. *Polym. Prepr.* **2003**, *44*, 35-36. (d) Bertino, M. F.; Hund, J. F.; Zhang, G.; Sotiriou-Leventis, C.; Tokuhira, A. T.; Leventis, N. *J. Sol-Gel Sci. Technol.* **2004**, *30*, 43-48. (e) Zhang, G.; Dass, A.; Rawashdeh, A.-M. M.; Thomas, J.; Council, J. A.; Sotiriou-Leventis, C.; Fabrizio, E. F.; Ilhan, F.; Vassilaras, P.; Scheiman, D. A.; McCorkle, L.; Palczer, A.; Johnston, J. C.; Meador, M. A. B.; Leventis, N. *J. Non-Cryst. Solids* **2004**, *350*, 152-164. (f) Leventis, N.; Palczer, A.; McCorkle, L.; Zhang, G.; Sotiriou-Leventis, C. *J. Sol-Gel Sci. Technol.* **2005**, *35*, 99-105. (g) Leventis, N.; Vassilaras, P.; Fabrizio, E. F.; Dass, A. *J. Mater. Chem.* **2007**, *17*, 1502-1508.
5. Katti, A.; Shimpi, N.; Roy, S.; Lu, H.; Fabrizio, E. F.; Dass, A.; Capadona, L. A.; Leventis, N. *Chem. Mater.* **2006**, *18*, 285-296.
6. Luo, H.; Lu, H.; Leventis, N. *Mech. Time-Depend. Mater.* **2006**, *10*, 83-111.

7. Capadona, L. A.; Meador, M. A. B.; Alunni, A.; Fabrizio, E. F.; Vassilaras, P., Leventis, N. *Polymer* **2006**, *47*, 5754-5761.
8. Meador, M. A. B.; Capadona, L. A.; McCorkle, L.; Papadopoulos, D. S.; Leventis, N. *Chem. Mater.* **2007**, *19*, 2247-2260.
9. Meador, M. A. B.; Fabrizio, E. F.; Ilhan, F.; Dass, A.; Zhang, G.; Vassilaras, P.; Johnston, J. C.; Leventis, N. *Chem. Mater.* **2005**, *17*, 1085-1098.
10. Ilhan, F.; Fabrizio, E. F.; McCorkle, L.; Scheiman, D. A.; Dass, A.; Palczer, A.; Meador, M. A. B.; Johnston, J. C.; Leventis, N. *J. Mater. Chem.* **2006**, *16*, 3046-3054.
11. Zhao, B; Brittain, W. J. *Prog. Polym. Sci.* **2000**, *25*, 677-710.
12. Ou, D. L.; Gould, G. L.; Stepanian, C. J. *U.S. Pat. Appl. Publ. US 2005192366 A1*, **2005**.
13. Keller, S. W.; Johnson, S. A.; Brigham, E. S.; Yonemoto, E. H.; Mallouk, T. E. *J. Am. Chem. Soc.* **1995**, *117*, 12879-12880.
14. Caruso, F.; Lichtenfeld, H.; Giersig, M.; Möhwald, H. *J. Am. Chem. Soc.* **1998**, *120*, 8523-8524.
15. Caruso, F.; Caruso, R. A.; Möhwald, H. *Science* **1998**, *282*, 1111-1114.
16. Caruso, F. *Adv. Mater.* **2001**, *13*, 11-22.
17. Werne, V.; Patten, T. *J. Am. Chem. Soc.* **2001**, *123*, 7497-7505.
18. Jiang, W.; Irgum, K. *Anal. Chem.* **2002**, *74*, 4682-4687.
19. Sulitzky, C.; Rückert, B.; Hall, A. J.; Lanza, F.; Unger, K.; Sellergren, B. *Macromolecules* **2002**, *35*, 79-91.

20. Fan, X.; Xia, C.; Fulghum, T.; Park, M.-K.; Locklin, J.; Advincula, R. C. *Langmuir* **2003**, *19*, 916-923.
21. Carlier, E.; Guyot, A.; Revillon, A. *React. Polym.* **1992**, *16*, 115-124.
22. Fan, X.; Xia, C.; Advincula, R. C. *Langmuir* **2005**, *21*, 2537-2544.
23. Huang, X.; Brittain, W. J. *Macromolecules* **2001**, *34*, 3255-3260.
24. Meier, L. P.; Shelden, R. A.; Caseri, W. R.; Suter, U. W. *Macromolecules* **1994**, *27*, 1637-1642.
25. Prucker, O.; Ruhe, J. *Langmuir* **1998**, *14*, 6893-6898.
26. Boven, G.; Oosterling, M. L. C. M.; Challa G.; Schouten, A. J. *Polymer* **1990**, *31*, 2377-2383.
27. Tsubokawa, N.; Kogure, A.; Maruyama, K.; Sone, Y.; Shimomura, M. *Polym. J.* **1990**, *22(9)*, 827-833.
28. Ellsworth, M. W.; Novak, B. M. *J. Am. Chem. Soc.* **1991**, *113*, 2756-2758. (b) Novak, B. M.; Davies, C. *Macromolecules* **1991**, *24*, 5481-5483. (c) Ellsworth, M. W.; Novak, B. M. *Chem. Mater.* **1993**, *5*, 839-844. (d) Novak, B. M.; Auerbach, D.; Verrier, C. *Chem. Mater.* **1994**, *6*, 282-286.
29. Prucker, O.; Ruhe, J. *Macromolecules* **1998**, *31*, 592-601.
30. Fricke, J.; Reichenauer, G. *J. Non-Cryst. Solids* **1987**, *95&96*, 1135-1142.
31. Although the diester analogue of **1** is known,³⁰ here we decided to work with **1**, because its one-pot synthesis is more attractive than the three-step literature method for the preparation of its diester analogue.
32. Parvole, J.; Billon, L.; Montfort, J. P. *Polym. International* **2002**, *51*, 1111-1116.

33. It is noted that by increasing the concentration of **1** in the sol, the gelation time increases, presumably owing to remaining traces of acid impurities that deactivate the base catalyst.
34. Leventis, N.; Elder, I. A.; Rolison, D. R.; Anderson, M. L.; Merzbacher, C. I. *Chem. Mater.* **1999**, *11*, 2837-2845.
35. Sing, K. S. W.; Everett, D. H.; Haul, R. A. W.; Moscou, L.; Pierotti, R. A.; Rouquerol, J.; Siemieniewska, T. *Pure and Applied Chemistry* **1985**, *57*, 603-619.
36. Hüsing, N.; Schubert, U.; Mezei, R.; Fratzl, P.; Riegel, B.; Kiefer, W.; Kohler, D.; Mader, W. *Chem. Mater.* **1999**, *11*, 451-457.
37. Ek, S.; Iiskola, E. I.; Niinistö, L.; Vaittinen, J.; Pakkanen, T. T.; Root, A. *J. Phys. Chem. B* **2004**, *108*, 11454-11463.
38. Bonhomme, C.; Coelho, C.; Baccile, N.; Gervais, C.; Azais, T.; Babonneau, F. *Acc. Chem. Res.* **2007**, *40*, 738-746.
39. Flory, P. J. *Principle of Polymer Chemistry*, Cornell University Press, Limited; Tenth Printing, 1989, p195.
40. (a) Wyzgoski, F. J.; Polce, M. J.; Wesdemiotis, C.; Arnould, M. A. *J. Polym. Sci. Part A: Polym. Chem.* **2007**, *45*, 2161-2171. (b) Buback, M.; Frauendorf, H.; Günzler, F.; Vana, P. *Polymer* **2007**, *48*, 5590-5598.
41. Leventis, N.; Mulik, S.; Wang, X.; Dass, A.; Sotiriou-Leventis, C.; Lu, H. *J. Am. Chem. Soc.* **2007**, *129*, 10660-10661.
42. Leventis, N.; Mulik, S.; Wang, X.; Dass, A.; Patil, V.; Sotiriou-Leventis, C.; Lu, H.; Churu, G.; Capecehatro, A. *J. Non-Cryst. Solids* **2007**, DOI: 10.1016.

43. (a) Porter, C. E.; Blum, F. D. *Macromolecules* **2000**, *33*, 7016-7020. (b) Porter, C. E.; Blum, F. D. *Macromolecules* **2002**, *35*, 7448-7452. (c) Metin, B.; Blum, F. D. *J. Chem. Phys.* **2006**, *125*, 054707/1-9.
44. Vyazovkin, S.; Dranca, I.; Fan, X.; Advincula, R.; *J. Phys. Chem. B* **2004**, *108*, 11672-11679.
45. Yamamoto, S.; Tsujii, Y.; Fukuda, T. *Macromolecules* **2002**, *35*, 6077-6079.
46. Gere, J. M.; Timoshenko, S. P. *Mechanics of Materials, Fourth Ed.*, PWS Publishing, Boston, MA: **1997**.
47. Vollrath, F.; Knight, D. P. *Nature* **2001**, *410*, 541-548.
48. Leventis, N.; Sotiriou-Leventis, C.; Mulik, S.; Dass, A.; Schnobrich, J.; Hobbs, A.; Fabrizio, E. F.; Luo, H.; Churu, G.; Zhang, Y.; Lu, H. *J. Mater. Chem.* **2008**, *18*, 2475-2482.
49. Gibson, L. J.; Ashby, M. F. *Cellular Solids, Structure and Properties*, Second Edition, Cambridge University Press, New York, N. Y. 1997.
- S1 Juvinall, R. C.; Marshek, K.M., *Fundamentals of Machine Component Design, 3rd Edition*, John Wiley & Sons, Inc., **2000**.

8. FIGURES

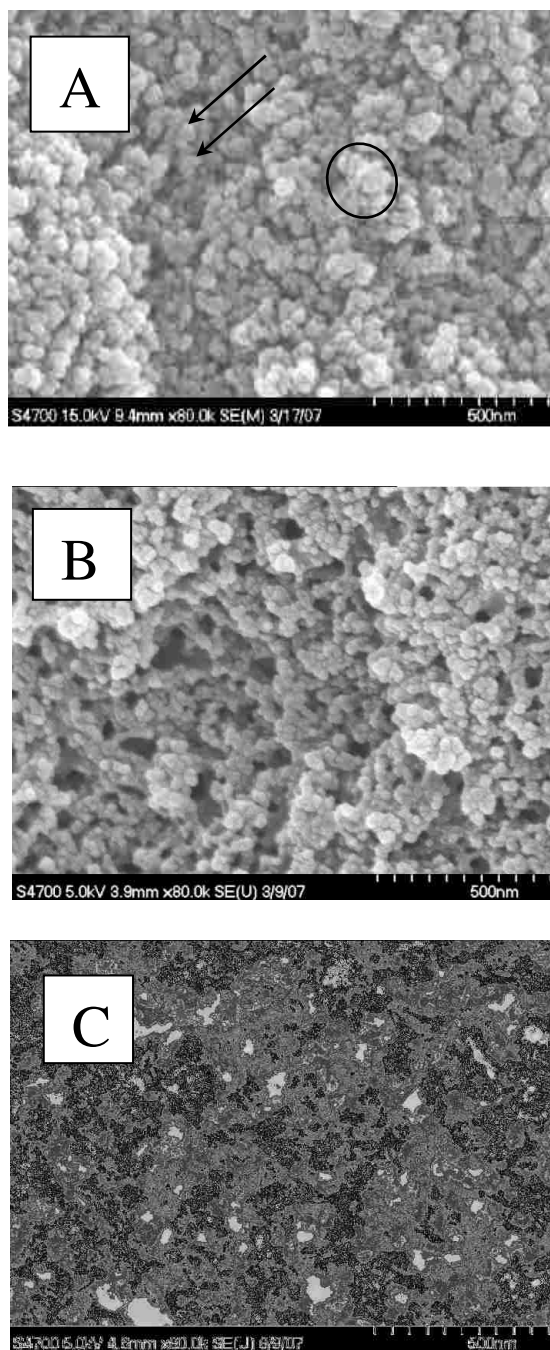


Figure 1. Scanning Electron Micrographs of: (A) native **Si-1** ($\rho_b=0.189 \text{ g cm}^{-3}$); (B) **X-Si-1-PMMA** (i.e., **Si-1** crosslinked with PMMA, $\rho_b=0.807 \text{ g cm}^{-3}$); and, (C) **X-Si-1-PS** (i.e., **Si-1** crosslinked with PS, $\rho_b=0.549 \text{ g cm}^{-3}$).

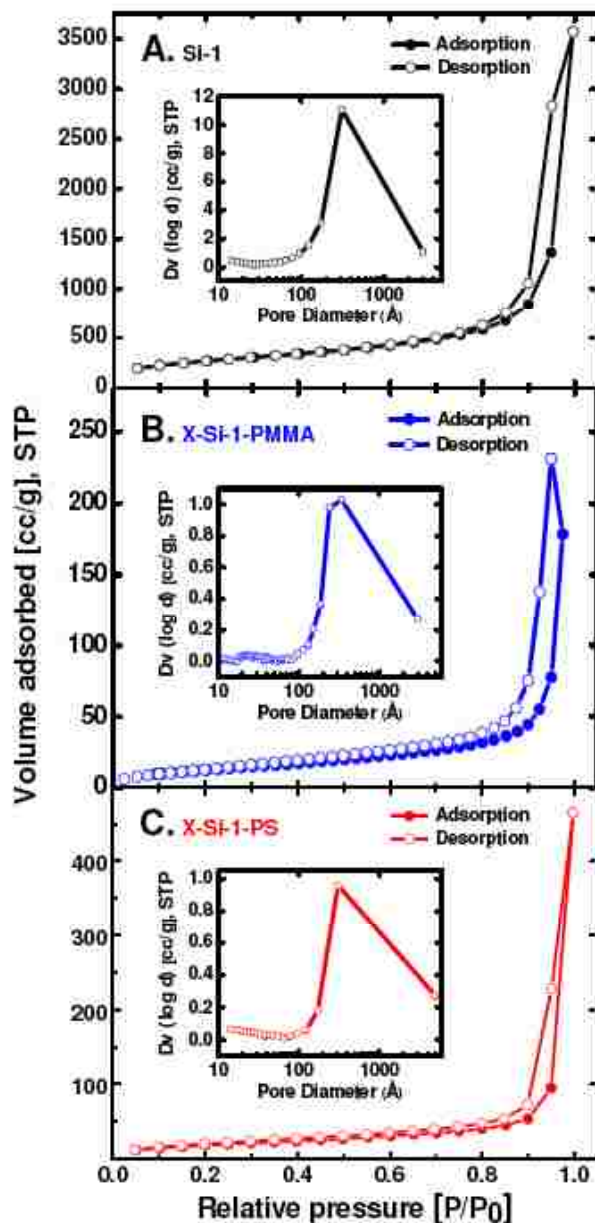


Figure 2. Nitrogen sorption porosimetry. (A) Adsorption-desorption isotherms for a native **Si-1** aerogel ($\rho_b=0.189 \text{ g}\cdot\text{cm}^{-3}$; BET surf. area= $973 \text{ m}^2\cdot\text{g}^{-1}$; Avg. pore dia = 29 \AA). (B) Adsorption-desorption isotherms for **X-Si-1-PMMA** aerogel ($\rho_b = 0.807 \text{ g}\cdot\text{cm}^{-3}$; BET surf. area = $46.1 \text{ m}^2\cdot\text{g}^{-1}$; Avg. pore dia. = 39 \AA). (C) Adsorption-desorption isotherms for a **X-Si-1-PS** aerogel ($\rho_b=0.549 \text{ g}\cdot\text{cm}^{-3}$; BET surf. area= $66.0 \text{ m}^2\cdot\text{g}^{-1}$; Avg. pore dia. = 42 \AA). Insets: Pore-size distribution by the BJH method applied on the desorption isotherm.

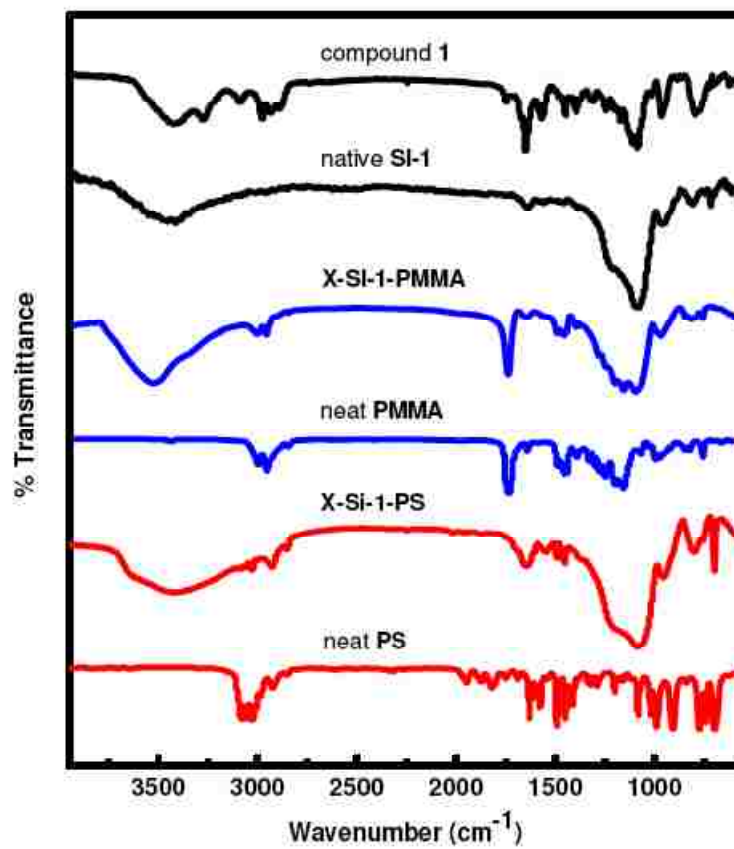


Figure 3. FTIR spectra (in KBr) of compound 1, native Si-1 and crosslinked aerogels X-Si-1-PMMA and X-Si-1-PS in comparison with neat PMMA and PS.

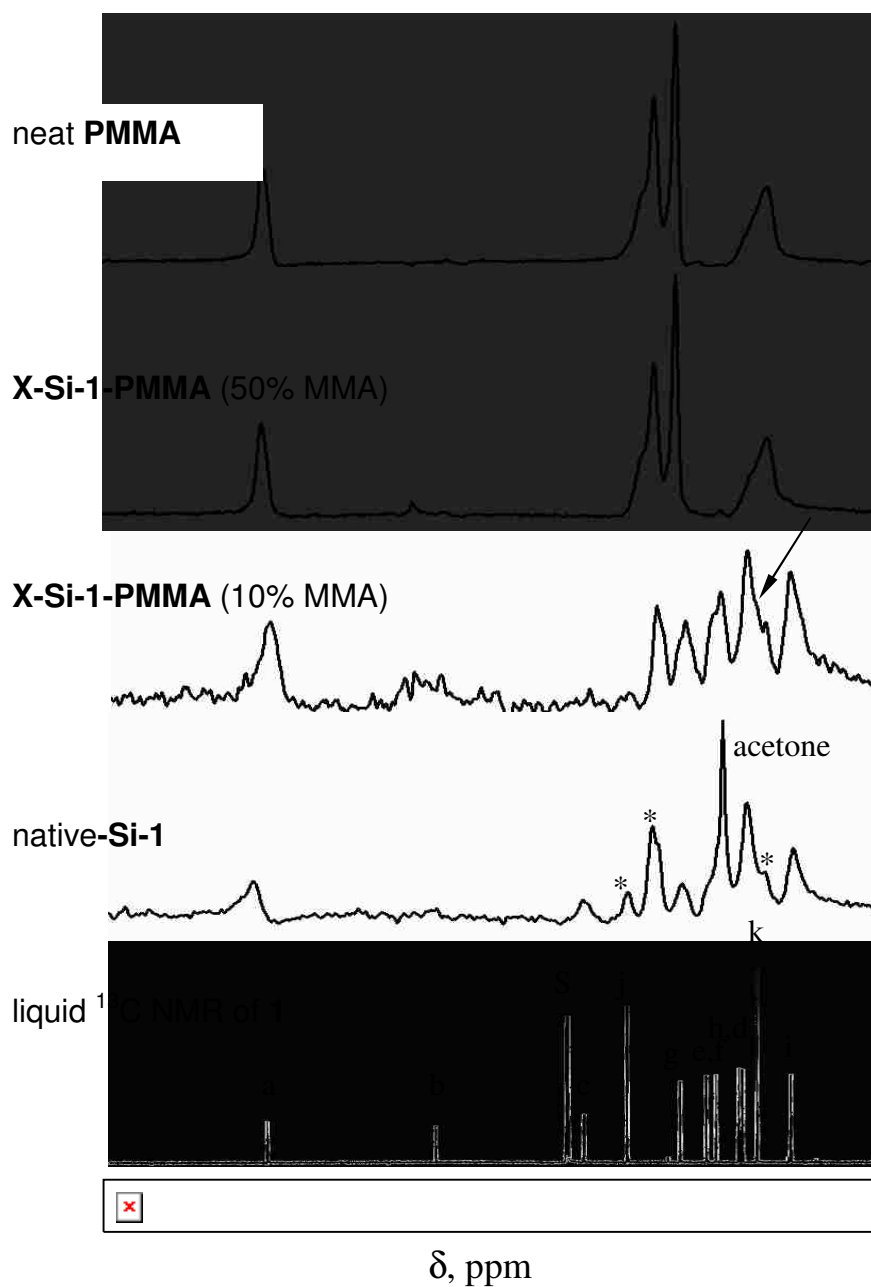


Figure 4A. Liquid ^{13}C NMR of **1** in CDCl_3 (marked as “S”). For peak assignments see structure of **1** in the text. Next four spectra: solid ^{13}C CPMAS NMR of samples as indicated. The monomer concentrations in the crosslinking bath are shown in parentheses.

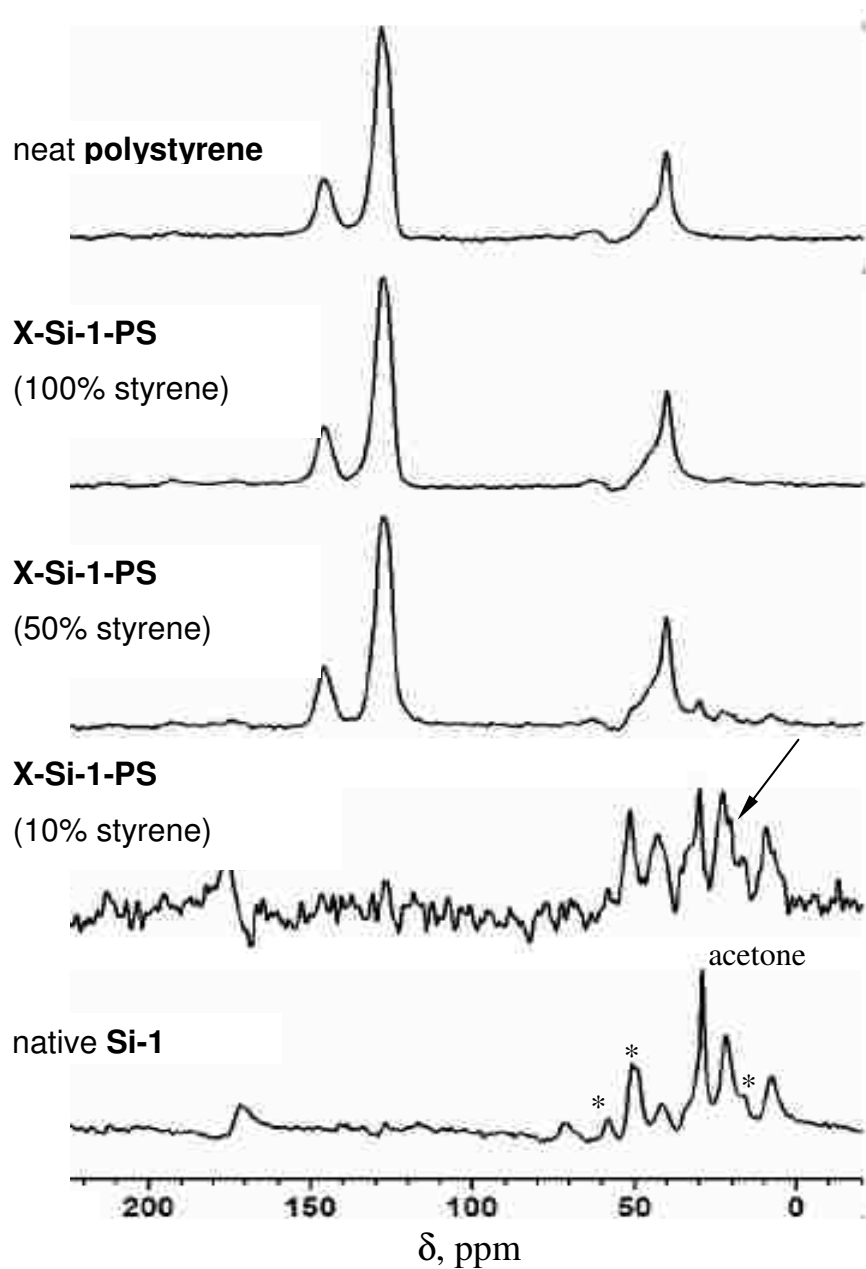


Figure 4B. Solid ^{13}C CPMAS NMR of samples as indicated. The monomer concentrations in the crosslinking bath are shown in parentheses. Top spectra in both parts: neat polymers obtained commercially – (Peaks marked with asterisks correspond to unhydrolyzed methoxy and ethoxy groups from TMOS and **1**. The shoulder and the peak shown by arrows corresponds to the α -carbon of the initiator after it has been attached to the β -carbon of MMA or styrene.)

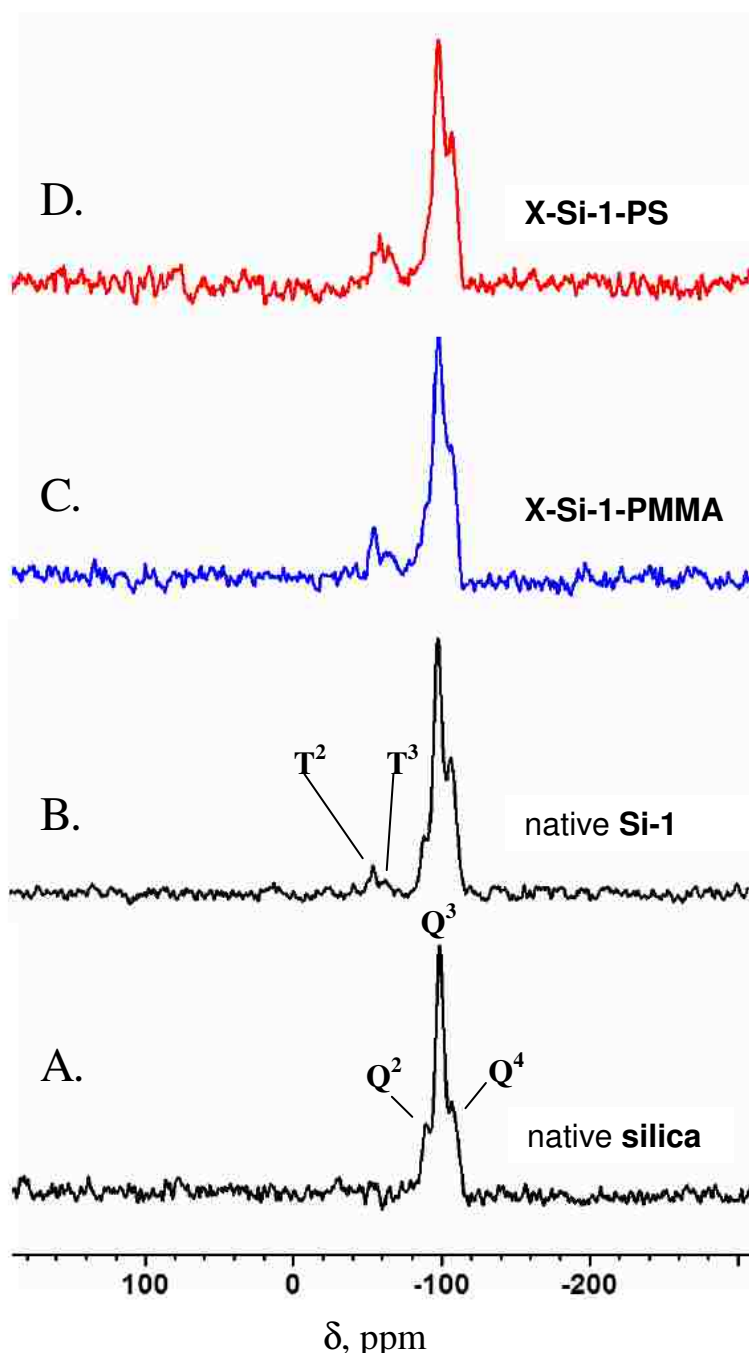


Figure 5. Solid state ^{29}Si CPMAS NMRs of: (A) base-catalyzed, TMOS-only native silica (silica aerogel prepared with traditional method); (B) native Si-1 (silica aerogel prepared by co-gelation of TMOS and **1**); (C) X-Si-1-PMMA (that is Si-1 crosslinked with PMMA); and, (D) X-Si-1-PS (that is Si-1 crosslinked with styrene).

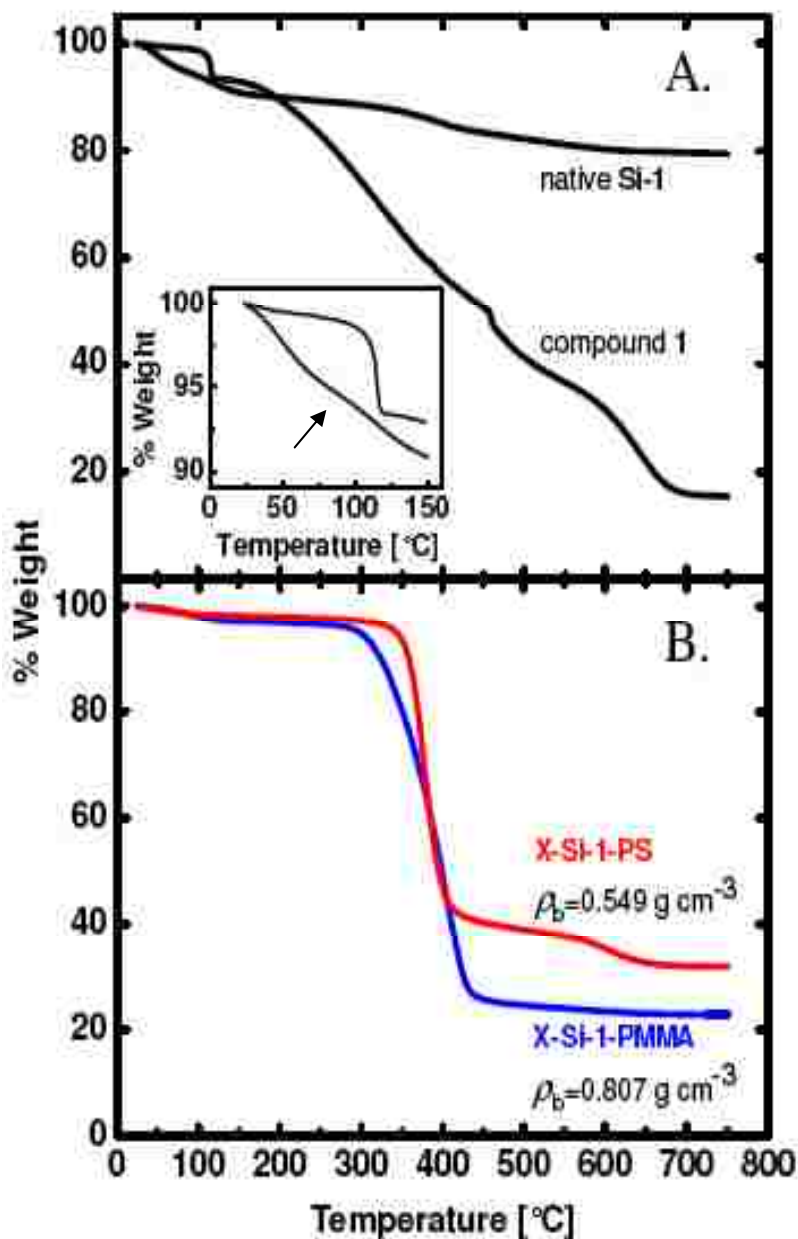


Figure 6. Thermogravimetric analysis (TGA) at $10 \text{ }^\circ\text{C min}^{-1}$ in air of: (A) compound **1** and native **Si-1**; (B) crosslinked samples of **X-Si-1-PMMA** and **X-Si-1-PS** at the densities shown. The total mass loss by **Si-1** ($\sim 20\%$ w/w) correlates well with the 18:1 mol ratio of TMOS:1 used in the sol (see text). The total mass loss by **X-Si-1-polymer** also correlates well with the amount of polymer calculated by the density increase and monolith size decrease upon crosslinking via eq 3 (see Table 1).

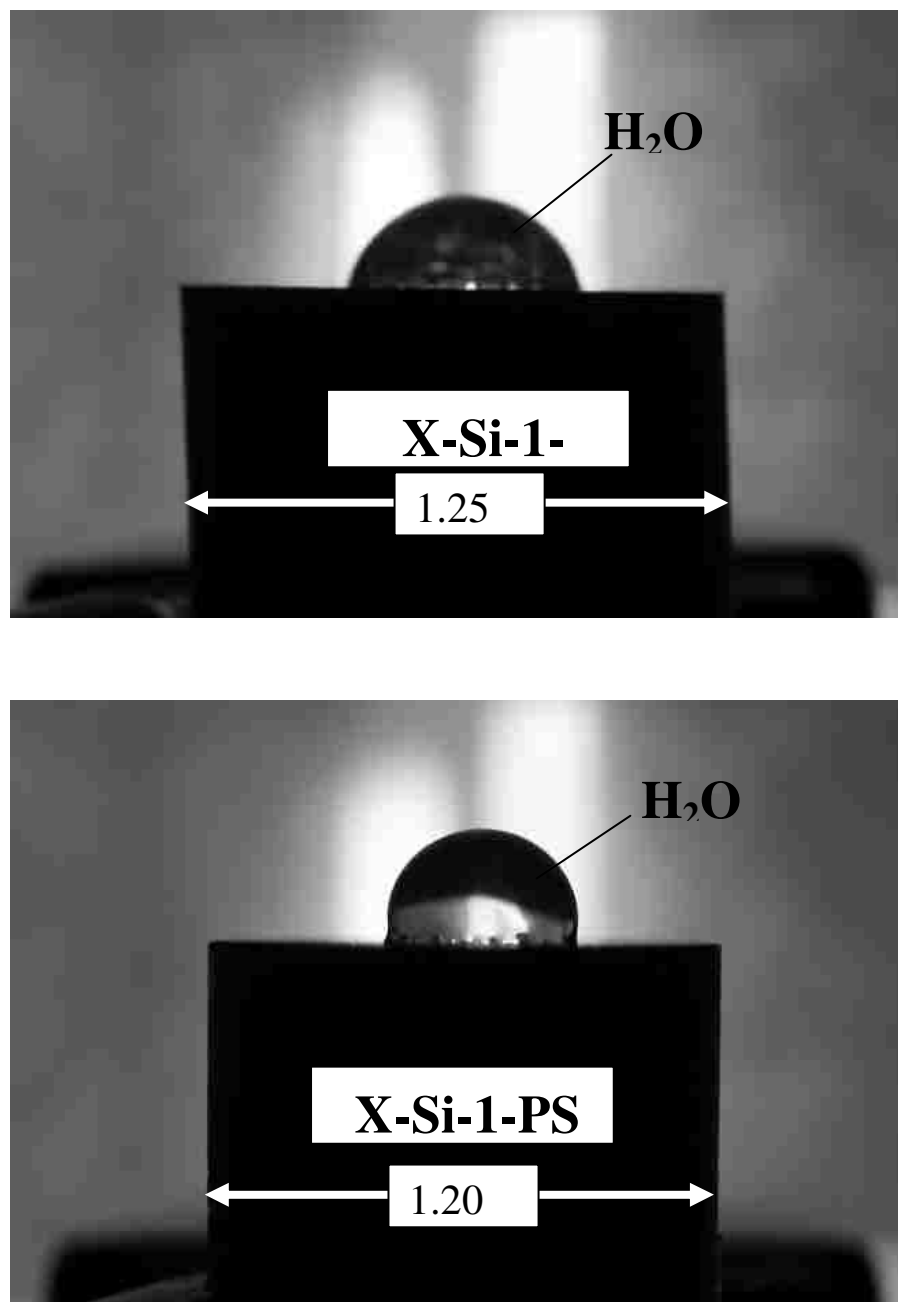


Figure 7. Back-illuminated water droplets on flat surfaces cut off from cylinders of **X-Si-1-PMMA** ($\rho_b=0.66 \text{ g cm}^{-3}$) and of **X-Si-1-PS** ($\rho_b=0.48 \text{ g cm}^{-3}$), as indicated. In both cases the materials are hydrophobic and the water droplets are not taken up by the pores, being stable indefinitely.

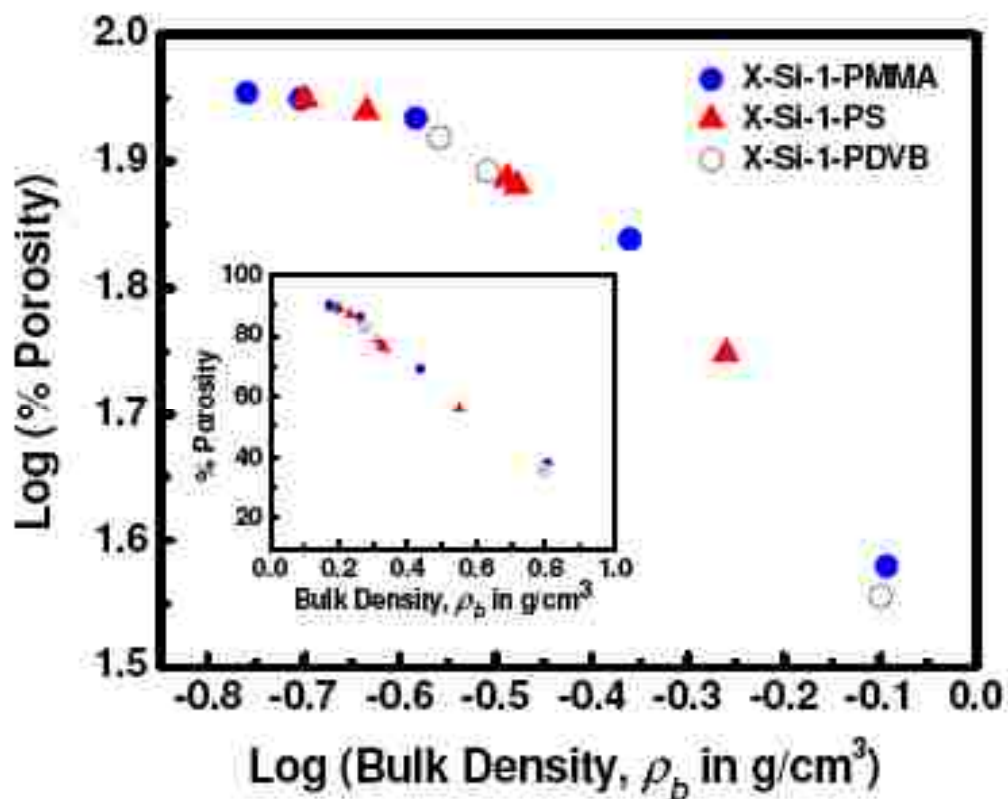


Figure 8. Log(Porosity) as a function of Log(Bulk Density) for all samples prepared. Inset: the same quantities plotted on a linear scale. The two quantities correlate with one another independently of the crosslinker, indicating that porosity is a materials property as expected by the design of **X-Si-1-polymer** whereas the polymer coats the skeletal framework conformally.

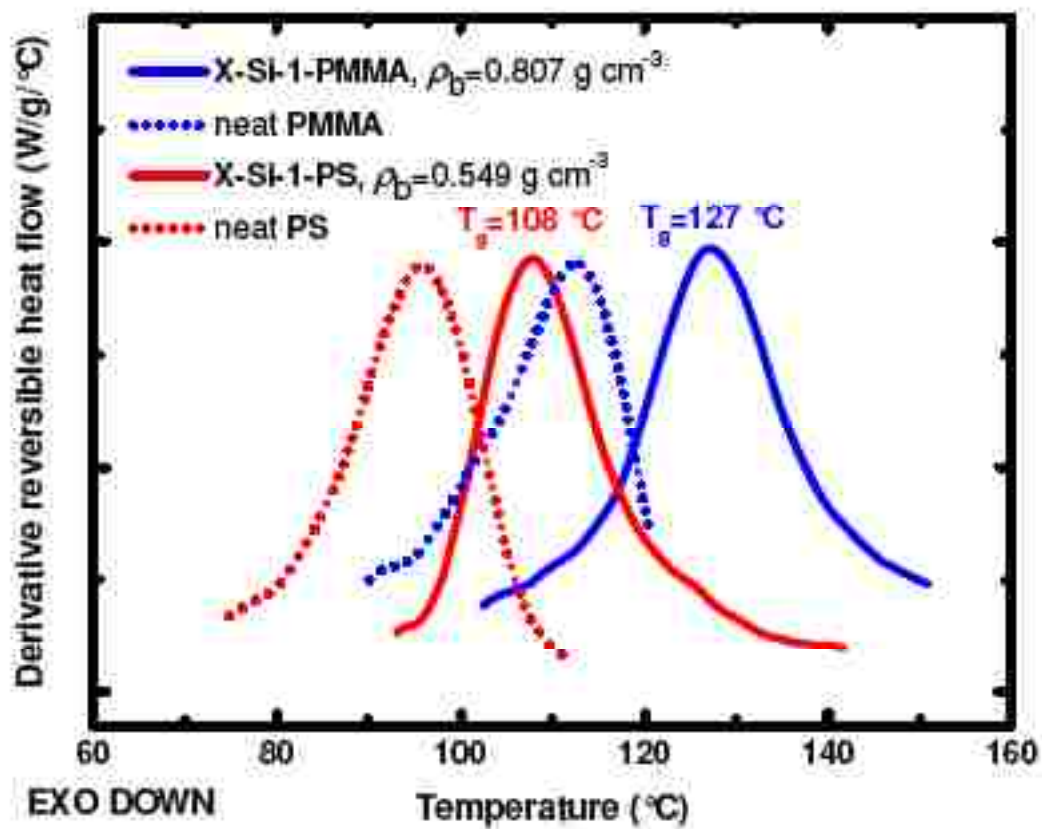


Figure 9. Shift in glass transition temperature (T_g) of PMMA and PS coated conformally and covalently bonded on the skeletal nanoparticles of **X-Si-1-PMMA** and **X-Si-1-PS**, in comparison to the neat polymers.

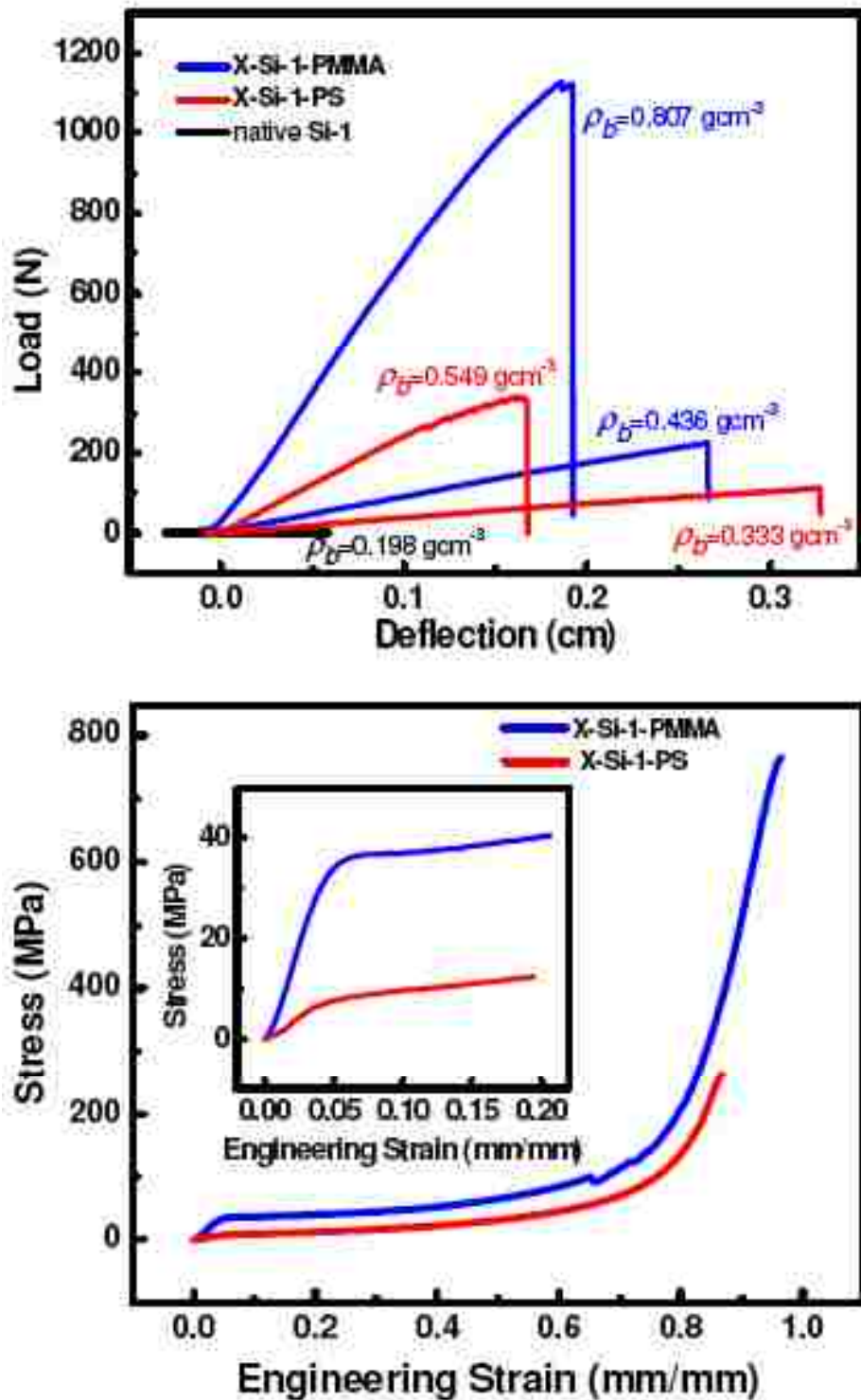


Figure 10. Mechanical characterization of X-Si-1-PMMA and X-Si-1-PS. Top: by a short beam three point flexural testing method. Bottom: by quasi-static compression.

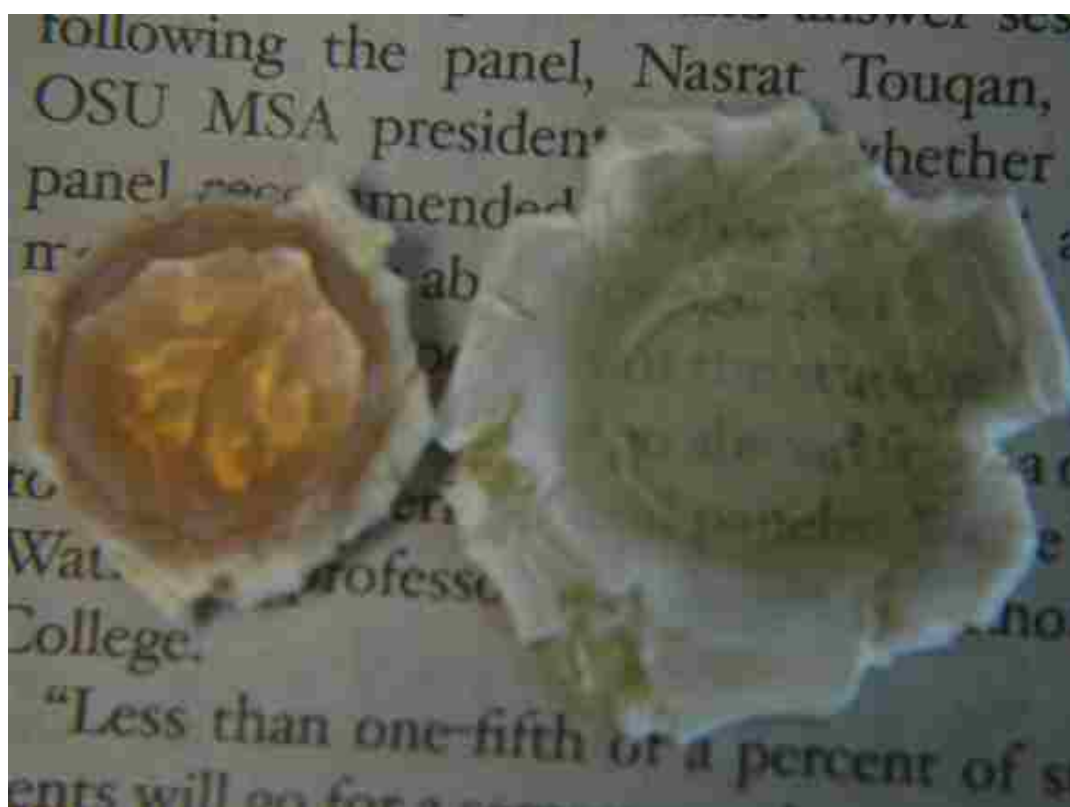
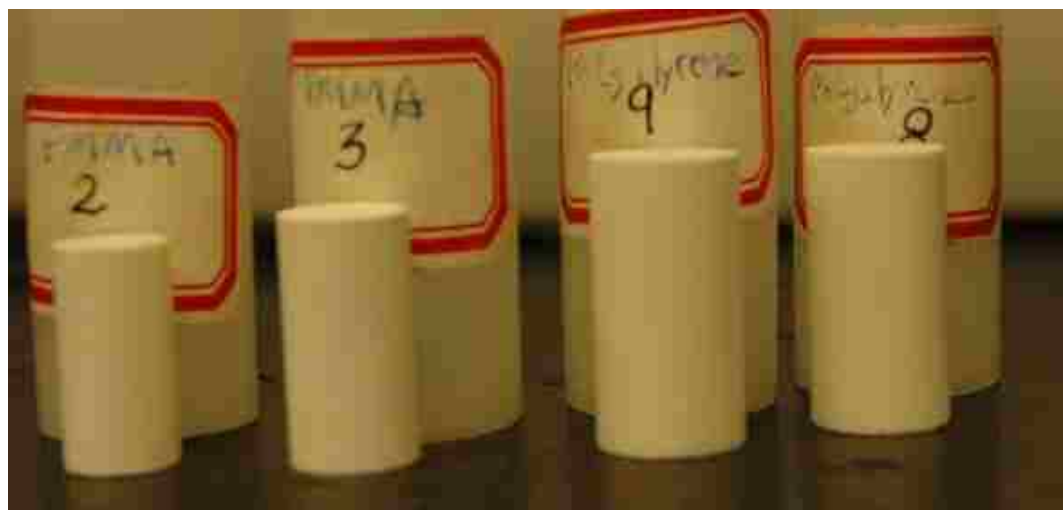


Figure 11. Top: Samples before compression, left: **X-Si-1-PMMA**, ($\rho_b=0.66 \text{ g/cm}^3$); right: **X-Si-1-PS**, ($\rho_b=0.46 \text{ g/cm}^3$). Bottom: Samples after compression, left: **X-Si-1-PMMA**, (compressed by 86% strain); right: **X-Si-1-PS**, (compressed by 96% strain).

9. SUPPORTING INFORMATION

Simulation of the bending process of a two nanoparticle system demonstrating that the Young's modulus of an aerogel monolith increases by accumulation of polymer on the skeletal framework.

Typical base-catalyzed aerogels consist of 3D assemblies of secondary silica nanoparticles forming pearl-necklace-like structures. In those structures, secondary particles are connected through circular cross-sections, referred to as "necks." It has been well known that under compression such structures will deform [S1], and the spring rate, a measure of microscopic stiffness of the pearl-necklace-like structure, is defined as the ratio of the applied force to the resulting deflection. Spring rate defined that way is also proportional to the bending stiffness of the macroscopic structure. Consequently, the Young's modulus, which represents the stiffness of the monolithic aerogel, is proportional to the bending stiffness of the connected secondary nanoparticles. For the calculation of the bending stiffness, we conducted finite element analysis on two identical connected secondary nanoparticles (Figure 1S) using the ABAQUS/Standard software package.

For calculation of the bending stiffness, the lower half of the bottom spherical particle was fixed and a small horizontal displacement, $\delta = 0.1$ nm was applied at the center of the top particle as indicated by the horizontal arrow at the center of the sphere at the top. The ratio of the resulting reaction force to the applied displacement gives the spring rate, which is proportional to the bending stiffness. For the native secondary silica nanoparticles (i.e., nanoparticles without a polymer coating) the radius R was set at 35 nm (based on the SEM data shown in the main article). The density of the silica spheres

was set at $\rho_s = 1.852 \text{ g cm}^{-3}$ as determined by He pycnometry, and their Young's modulus was taken as $E_s = 70 \text{ GPa}$. A similar analysis was also conducted with polymer nanoencapsulated silica secondary nanoparticles. For the polymer coating, the Young's modulus was set at $E_s = 1 \text{ GPa}$ and the density at $\rho_{\text{polymer}} = 1.2 \text{ g cm}^{-3}$.

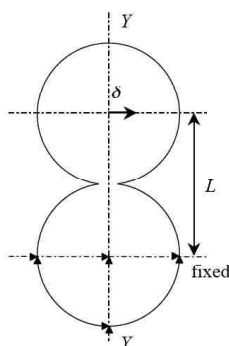


Figure 1S. A two-sphere model for two secondary particles connected to each other. The bottom half of the lower sphere is fixed. A displacement δ is applied at the center of the sphere at the top. “L” represents the center-to-center distance between the two spheres.

A parametric study was carried out by varying the neck diameter between the two nanoparticles. (The neck diameter is the diameter of the circular contact area between two identical secondary spherical nanoparticles.) Figure 2S shows an example of the normal stress distribution in the Y direction as a result of the applied displacement (for the specific example $L = 68 \text{ nm}$, and the coating thickness = 10 nm). It is noteworthy that with the polymer coating applied, the size of the high stress zones, as indicated in Figure 2S(b), becomes smaller than that in the native silica, shown in Figure 2S(a).

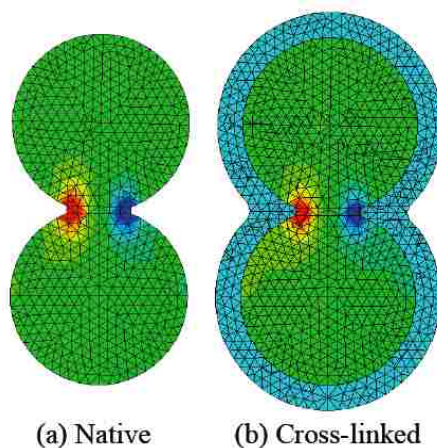


Figure 2S. Contours of the normal stresses in the Y direction (blue: compressive stress; red: tensile stress).

Figure 3S shows the ratio of the bending stiffness of two connected polymer encapsulated secondary nanoparticles to the bending stiffness of two connected native secondary silica nanoparticles, as a function of the dimensionless contact diameter, defined as the contact diameter divided by the secondary nanoparticle diameter. The results show that for all contact diameters, the bending stiffness increases when the secondary nanoparticles are coated with a conformal polymer layer. When the contact diameter is small, the bending stiffness of the two-spheres is small, so that the width increase of the necks due to the polymer nanoencapsulation will contribute to a large increase in bending stiffness. When the contact diameter of the native spheres is large, the bending stiffness of the two secondary silica nanoparticles is also relatively high. But yet, the polymer nanoencapsulation will still contribute to a large increase in the bending stiffness. Finally, for a fixed contact diameter, the polymer layer thickness was varied to determine its effect on the bending stiffness and Young's modulus. It is emphasized that

the Young's modulus increase is proportional to the increase of bending stiffness of crosslinked aerogels with slender necks. Figure 4S plots the bending stiffness ratio of the polymer encapsulated to native silica two-sphere model as a function of the density due to the increase of nanoencapsulated polymer thickness. The dimensionless contact diameters were fixed at 0.2774, 0.3364, and 0.3992, respectively, while the polymer thickness varies from 2 nm to 22 nm. At an initial dimensionless contact diameter of 0.2774, the bending stiffness (and also the Young's modulus) is anticipated to improve from 26% to 138%. At a dimensionless contact diameter of 0.3992, the stiffness increases from 3% to 35% when the polymer encapsulation thickness varies from 2 nm to 22 nm. A larger increase in stiffness is anticipated when the initial contact diameter of the native nanoparticles is small. This seems to be the case for our actual polymer crosslinked aerogel samples: the modulus of the native aerogels is relatively low, therefore the contact diameter should be relatively small; after polymer nanoencapsulation we observe a large increase in the Young's modulus implying that the contact diameter increases dramatically.

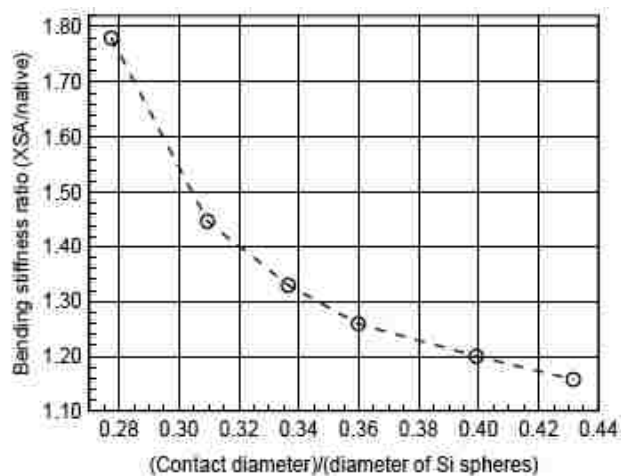


Figure 3S. Bending stiffness ratio of polymer nano-encapsulated secondary silica nanoparticles as a function of the dimensionless contact diameter of the secondary silica nanoparticles.

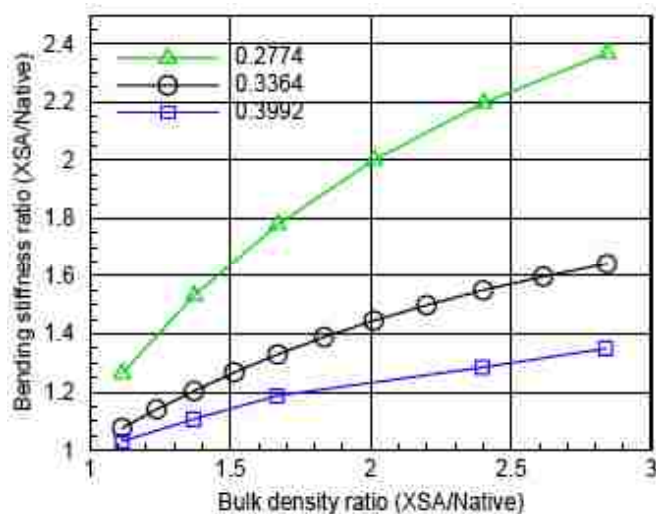


Figure 4S. Bending stiffness ratio of polymer encapsulated secondary silica nanoparticles to the neat silica nanoparticles for dimensionless contact diameters of 0.2774, 0.3364, and 0.3992, as a function of the increase in densities of cross-linked samples due to polymer nanoencapsulation.

PAPER II**TIME-EFFICIENT ACID-CATALYZED SYNTHESIS OF RESORCINOL-FORMALDEHYDE AEROGELS**

Sudhir Mulik, Chariklia Sotiriou-Leventis* and Nicholas Leventis*

Department of Chemistry, University of Missouri-Rolla, Rolla, MO 65409

Published in *Chemistry of Materials* **2007**, 25(19), 6138-6144.

1. ABSTRACT

Resorcinol (R) – formaldehyde (F) aerogels are pursued as precursors of carbon aerogels, which are electrically conducting. They are usually prepared via a week-long base-catalyzed gelation process from an aqueous sol. For this work, we reasoned that since both the reaction of R with F and the condensation of the resulting hydroxymethyl resorcinol with R are both electrophilic aromatic substitutions, therefore they should proceed easily by acid-catalysis in one pot. Thereby, we have developed and report an HCl-catalyzed gelation process in CH₃CN, which is completed in about 2 h at room temperature or in 10 min at 80 °C. The final aerogels are chemically indistinguishable (by IR and ¹³C CPMAS NMR) from typical base-catalyzed samples. In analogy to phenol-formaldehyde resin formation, the mechanism may involve *o*-quinone methide intermediates (hence the red color prevailing throughout the process). The effect of aging is discussed in terms of shrinkage and is attributed to further reaction and incorporation of more formaldehyde into wet gels, followed by syneresis (reaction with one another of dangling oligomeric appendices on the skeletal framework).

2. INTRODUCTION

Aerogels comprise a special class of low-density open cell foams with large internal void space, which is responsible for useful materials properties such as low thermal conductivity, high surface area and high acoustic impedance.¹ Chemically, most aerogels consist of inorganic networks of metal and semimetal oxide nanoparticles, usually silica. On the other hand, resorcinol-formaldehyde (RF) aerogels are the most well-known organic aerogels, and are pursued not only for their typical aerogel properties, but also most importantly as precursors to electrically conducting carbon aerogels.² Typically, RF aerogels are prepared via Pekala's method that involves base (Na_2CO_3)-catalyzed gelation of aqueous solutions of resorcinol with formaldehyde, followed by aging and drying from supercritical fluid (SCF) CO_2 .³⁻⁶ RF aerogels exhibit high porosity (>80%), high surface area (>400 m^2g^{-1}), ultrafine cell size (<500 Å) and densities as low as 0.03 g cm^{-3} . Mechanistically, the role of the base catalyst has been explained in terms of deprotonation of the -OH group of resorcinol to $-\text{O}^-$, which is a strong electron donor and thus an effective activator of the aromatic ring towards electrophilic aromatic hydroxymethylation via reaction with formaldehyde. In turn, formation of hydroxymethyl derivatives of resorcinol is followed by condensation to methylene ($-\text{CH}_2-$) and methylene ether ($-\text{CH}_2-\text{O}-\text{CH}_2-$) bridges. Within the context of this mechanism, the effect of the preparation conditions on the aerogel nanostructure has been studied extensively. The R:C mol ratio is typically varied in the 50-300 range. For high resorcinol-to-catalyst ratio (e.g., R:C~1,500) formation of interconnected microspheres has been reported.^{7,8} Smaller particles connected with large necks were observed with low R:C ratios (e.g., 50).⁹ The final pore structure depends strongly on the

sol pH.¹⁰ The major drawback of the base-catalyzed method seems to be the long gelation time, which typically extends up to 7 days at 85 °C, and is followed by aging for at least another 3 days in CF₃COOH at 45 °C.

The extensive literature on base-catalyzed RF aerogels overshadows the few reports on acid-catalyzed processes. Those include gelation in HClO₄/acetone at 45 °C followed by 3 days of aging,¹¹ in aqueous HNO₃ at 80 °C (two day gelation, 7 days aging),¹² and in acetic acid at room temperature (one day gelation, 3 days of aging at 50 °C and 3 days at 90 °C).¹³ The general observation is that processes involving acid-catalysis are shorter. In that regard, the shortest process we are aware of is a hybrid method where resorcinol and propanal are first incubated with triethylamine (Et₃N) in CH₃CN for 1 h at 80 °C, followed by addition of HCl and room temperature gelation within 1-2 minutes.¹⁴ However, when we attempted the same process for the synthesis of RF gels, addition of HCl at the prescribed amounts caused precipitation of triethylammonium chloride, contaminating the gels. At that point we questioned the need for Et₃N, and more generally the effectiveness of the base-catalyzed route: our reasoning was that on one hand -O⁻ is a better electron donor than -OH, but not very much so ($\sigma_{p,O^-} = -0.81$ vs. $\sigma_{p,OH} = -0.37$).¹⁵ On the other hand, addition of formaldehyde is an electrophilic aromatic substitution reaction, and as such it should be accelerated by acid catalysis. In fact, chloromethylation of aromatic systems (i.e., addition of -CH₂Cl) using stoichiometric amounts of formaldehyde and HCl is an efficient and well-known reaction.^{16a} By using only a catalytic amount of HCl, the reaction should proceed as hydroxymethylation (Lederer-Manasse reaction),^{16b} adding the same functionality (-CH₂OH) as the base-catalyzed route. Furthermore, acid catalysis should also promote in

one-pot a subsequent condensation step by protonation of the newly formed $-\text{CH}_2\text{OH}$ groups leading to Bakelite-type resins.^{16b} Based on this line of reasoning, we have developed and describe here an HCl-catalyzed gelation process that is completed in minutes rather than days, yielding gels indistinguishable from those obtained by the usual base-catalyzed process in a week. Importantly, RF gels processed with no aging at all shrink significantly less and therefore they are lower density materials than gels aged for a few days.

3. EXPERIMENTAL

3.1 Materials

Formaldehyde (37% w/w aqueous solution methanol stabilized) and acetone (anhydrous) were used as received from Aldrich Chemical Co. Acetonitrile (ACS reagent grade) and hydrochloric acid (12.1 N) were purchased from Fisher Scientific. Syphon grade CO_2 was obtained from BOC Gases, Murray Hill, N.J. supplied locally by Ozarc Gases.

HCl-catalyzed RF gels were prepared using resorcinol (R) and formaldehyde (F) in four different R:F mol ratios (1:2, 1:3, 1:5 and 1:10; sols made with R:F=1:20 did not gel). For example, RF gels with 1:2 mol ratio were prepared by mixing at room temperature two solutions: solution "A" containing 0.337 g (3.06 mmol) of resorcinol, 0.477 mL (6.29 mmol) of the commercially available formaldehyde solution and 11.5 mL CH_3CN ; and, solution "B" containing 0.636 mL CH_3CN and 0.03 mL (0.363 mmol) of concentrated (12.1 N) HCl (R:C=8.4). The mixture (sol) was poured into polypropylene molds (Wheaton polypropylene Omni-Vials, part No. 225402, ~1 cm in diameter) and

gelled within two hours at room temperature or in about 10 min at 80 °C. Although it might not be an advantage, typically, the resulting gels were aged in their molds at room temperature for 24 h, subsequently they were washed with acetone (3×, 8 h, 20 mL of acetone each time) and were dried in an autoclave with liquid CO₂. Thus, liquid CO₂ at 14 °C first extracts the pore-filling solvent (acetone with traces of CH₃CN) out of the wet gels, and when there is no more solvent coming out of the gels, the temperature and the pressure of the autoclave are taken above the critical point of CO₂ (32 °C, 73.8 bar), which is then vented off isothermally at 40 °C.

For comparison, Na₂CO₃-catalyzed RF gels were made from an aqueous solution at 85 °C according to Pekala's method using R:F and R:C ratios equal to 1:2 and 72.5, respectively (200 mL of H₂O, 6.39 g of R (0.29 M), 8.64 mL of the 37% aq. solution of F (0.57 M), and 0.23 g Na₂CO₃).³ Gelation took place in 7 days. Although in Pekala's method gels were aged for 3 additional days in a 0.125% w/w CF₃COOH in H₂O at 45 °C, here for our purposes some gels were aged for 3 days in their original molds for comparison. At the end, all gels, either aged in their original molds or in aqueous CF₃COOH were solvent-exchanged with acetone (4 washes, 8 h each time) and were dried with CO₂ taken out supercritically. Gels aged in their molds swell to about double their size in acetone; they are also extremely fragile and they do not survive the transfer to the autoclave in one piece. Na₂CO₃-catalyzed gels aged in CF₃COOH are much sturdier and behave like the 10 min HCl gels of this study.

3.2 Methods

The early stages of the reaction between resorcinol and formaldehyde were investigated by: (a) recording ^{13}C NMR spectra under various conditions using a 400 MHz Varian Unity Inova NMR instrument; (b) carrying out the reaction in a UV-cuvette placed in a Beckman DU 640B UV-Vis spectrophotometer; and, (c) monitoring the viscosity of the sol according to ASTM Designation D 562-01 “Standard Test Method for Consistency of Paints Measuring Krebs Unit (KU) Viscosity Using a Stormer Type Viscometer.” Supercritical fluid CO_2 drying was conducted using an autoclave (SPI-DRY Jumbo Supercritical Point Drier, SPI Supplies, Inc., West Chester, PA). Chemical characterization of RF aerogels was conducted with infrared and ^{13}C NMR spectroscopies. Infrared spectra were obtained in KBr pellets using a Nicolet-FTIR Model 750 Spectrometer. Solid ^{13}C NMR spectra were obtained with samples ground in fine powders on a Bruker Avance 300 Spectrometer with 75.475 MHz carbon frequency using magic angle spinning (7 kHz) with broad band proton suppression and the CPSELTICS pulse sequence for spin sideband suppression. Spectra were externally referenced to the carbonyl of glycine (196.1 ppm relative to tetramethylsilane). Bulk densities were calculated from the weight and the physical dimensions of the samples. Skeletal densities were determined by helium pycnometry using Micromeritics AccuPyc 1330 instruments. Mesoporous surface areas and pore size distributions were measured by nitrogen adsorption/desorption porosimetry using a Micromeritics ASAP 2000 Surface Area/Pore Distribution analyzer. Samples for surface area and skeletal density determination were outgassed at 80 °C for 24 h before analysis. Scanning electron

microscopy was conducted with samples coated with Au using a Hitachi S-4700 field emission microscope.

4. RESULTS

4.1 Reaction of resorcinol with formaldehyde in HCl-catalyzed CH₃CN solutions

On the basis of our working hypothesis, namely that both electrophilic aromatic hydroxymethylation and the subsequent condensation of the resulting aromatic systems should both be favored by acid catalysis, it was first decided to compare the reaction of resorcinol with formaldehyde in acetonitrile with an acid catalyst (HCl), a base catalyst (Et₃N) and with no-catalyst at all. The progress of the reaction was monitored with ¹³C-NMR in CD₃CN 15 min after mixing R with F using a 1:2 molar ratio R:F (Fig. 1). Peak assignment was based on Werstler's analysis,¹⁷ and our own spectra simulations. By comparing Figures 1A and 1B (HCl-catalyzed, vs. non-catalyzed reaction, respectively) we see clearly that the position of the phenolic carbon has been shifted upfield (152.8 ppm, Fig. 1A) relative to the non-catalyzed solution (158.5 ppm, Fig. 1B), and the carbon in the meta position relative to both phenols (carbon b) has been shifted slightly downfield (to 132.2 ppm from 130.6 ppm). The intensity of the aromatic carbons of resorcinol designated as "c" and "d" at 107.5 and 102.7 ppm respectively (Fig. 1B) has been decreased and a new peak partially merging with acetonitrile has appeared at ~120 ppm (Fig. 1A). The peak at ~83.1 ppm, present in both reaction mixtures, is assigned to methylene glycol from formaldehyde, while peaks in the 85-86 ppm range are attributed to condensation products of formaldehyde (e.g., -O-CH₂-O-CH₂-O-). Both reaction mixtures (Fig. 1A and 1B) show small peaks at 54.5 ppm corresponding to aromatic CH₂OH carbons, but the spectrum of the HCl-catalyzed mixture (Fig. 1A) is dominated

by the peak at 29.5 ppm, which is assigned to $-\underline{\text{C}}\text{H}_2-$ carbons sandwiched between two aromatic rings. Certainly, this resonance supports fast condensation of hydroxymethylated resorcinol with resorcinol, and is completely absent from the spectrum of the non-catalyzed reaction mixture. Similarly to the non-catalyzed mixture of Fig. 1B, base-catalyzed reactions kept at room temperature show a small peak at 54.5 ppm assigned to aromatic $\underline{\text{C}}\text{H}_2\text{OH}$ (data not shown), and if heated at 80 °C they show an additional new resonance at 66.0 ppm (Fig. 1C) assigned to aromatic $\underline{\text{C}}\text{H}_2\text{-O-CH}_2\text{OH}$. No signals of bridging $-\text{CH}_2-$ groups at ~30 ppm are visible. Overall, ^{13}C NMR data confirm that the RF reaction proceeds faster under HCl-catalyzed conditions. But, is this faster reaction rate of any practical consequence?

HCl-catalyzed RF-solutions in CH_3CN quickly develop a characteristic red color ($\lambda_{\text{max}}=543$ nm, Fig. 2) and gel. Gelation was followed by viscosity measurements with a Stormer-type paddle viscometer both at room temperature and at 80 °C. As shown in Fig. 3, HCl-catalyzed RF solutions in CH_3CN gel within 2 h at room temperature and within 10 min at 80 °C. By comparison, non-catalyzed or Et_3N -catalyzed mixtures do not gel at 80 °C in at least a day. The aqueous Na_2CO_3 -catalyzed sol kept at 85 °C gels in 7 days, consistently with the literature.³

4.2 Time-efficient preparation and characterization of RF aerogels

The qualitative findings of section 3a were formalized as shown in Scheme 1. The absolute amounts of R and catalyst (see experimental section) were chosen to match those of the Baumann's $\text{Et}_3\text{N}/\text{HCl}$ method of gelation of R with propanal.¹⁴ The R:F mol ratio was varied from 1:2 to 1:10. Wet gels made with 1:2, 1:3 and 1:5 R:F molar ratio are red and clear, gels prepared with 1:10 R:F molar ratio are pink and opaque. In

general, wet gels were aged in their molds for 24 h, then they were removed, washed with acetone and dried with liquid CO₂ taken out supercritically. Appearance-wise, HCl-catalyzed RF gels made within 10 min in CH₃CN using a R:F mol ratio equal to 1:2 as shown in Scheme 1 are pretty similar to samples made through the week-long process in aqueous Na₂CO₃. All samples were characterized for shrinkage by comparing their physical dimensions relative to their mold (whenever possible). All pertinent physical characterization data are summarized in Table 1. Since at 80 °C HCl-catalyzed sols gel in only 10 min, a subsequent long aging period creates an asymmetry in the whole process and is not practical. For this, representative R:F=1:2 gels were also processed without aging and relevant data are also included in Table 1.

Scheme 1. Time-Efficient Synthesis of Resorcinol-Formaldehyde Aerogels

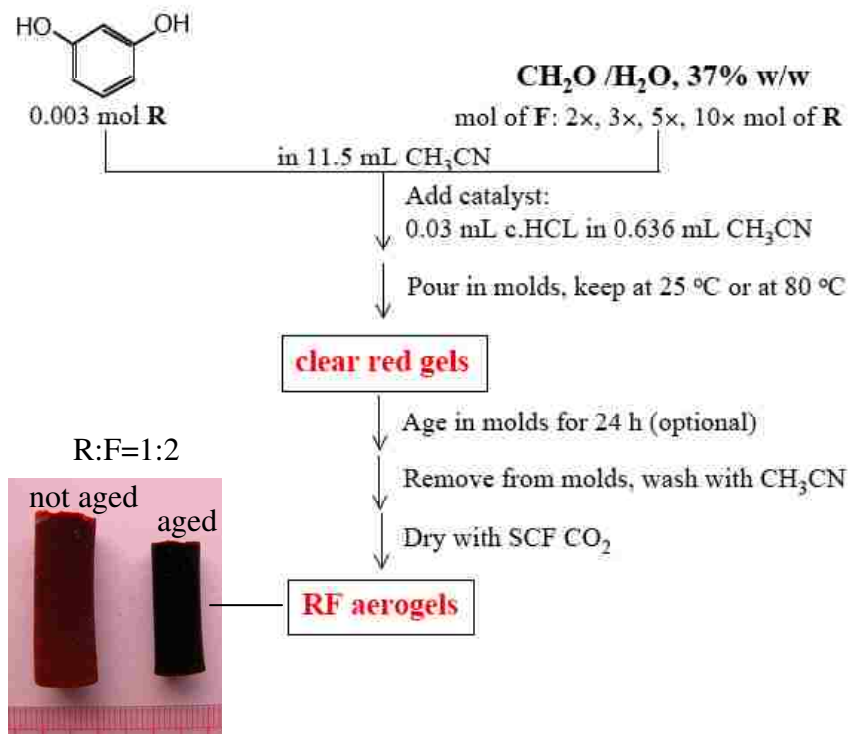


Table 1. Physical characterization data for RF aerogels processed under various conditions

R:F	Aging Time (days)	Diameter (cm)	% Shrinkage ^f	Bulk Density (g cm ⁻³)	Skeletal Density (g cm ⁻³)	Porosity (% void space)	BET Surf. Area [Av. Pore Diam. ^g] (m ² g ⁻¹ [nm])	particle diameter (nm) ^h
via HCl-catalyzed gels in CH₃CN								
1:2 ^a	0 ^j	0.94±0.02 ^c	29	0.101±0.007	1.492±0.006 ^e	93.2±0.9	314 [22.9; 118]	12.8
1:2 ^b	1 ^j	0.65±0.02 ^d	38	0.136±0.008	1.363±0.056	90.0±0.8	318 [14.7; 83.3]	13.8
1:2 ^a	5 ^j	0.81±0.01 ^c	39	0.157±0.004	1.459±0.002 ^e	89.2±0.9	512 [12.6; 44.4]	8.03
1:3 ^b	1 ^j	0.63±0.02 ^d	39	0.175±0.008	1.386±0.030	87.4±0.4	437 [15.0; 45.6]	9.91
1:5 ^b	1 ^j	0.63±0.01 ^d	39	0.159±0.005	1.368±0.021	88.4±0.2	363 [14.6; 61.2]	12.0
1:10 ^b	1 ^j	0.63±0.00 ₁ ^d	39	0.164±0.010	1.565	90.2±0.2	351 [10.8; 51.7]	10.9
via Na₂CO₃-catalyzed gels in water³								
1:2 ⁱ	3 ^j	1	1	1	1.481±0.004	1	818 [19.4]	4.95
1:2 ⁱ	3 ^k	1.52±0.04 ^m	40	0.173±0.006	1.458±0.006	88.1±0.5	744 [15.3; 27.4]	5.53

Where,

a: Average of 5 samples;

b: Average of 3 samples;

c: Made in 1.33 cm diameter cylindrical molds;

d: Made in 1.04 cm diameter cylindrical molds;

e: Those skeletal densities were determined on a different instrument at a different time;

f: All shrinkage is observed after drying with SCF CO₂. Gels do not show shrinkage relative to the molds;

g: by the $4V_{\text{Total}}/\sigma$ method (where V_{Total} : mass specific total pore volume, σ : mass specific surface area by the BET method). V_{Total} has been calculated by two methods, hence the two numbers cited for the Average Pore Diameter: first automatically by the system software from single point volume measurements of N₂ adsorbed (from the N₂ adsorption curves, e.g., see Figure 5), and second manually from the bulk and skeletal densities via $V_{\text{Total}}=(1/\rho_b)-(1/\rho_s)$, where ρ_b and ρ_s represent the bulk and skeletal densities, respectively);

h: Diameter=2×r, where $r=3/\sigma\rho_s$ (r: particle radius);

i: Average of 2 samples;

j: Aged in the molds;

k: Aged in aqueous CF₃COOH (see experimental section);

l: Gel is too fragile, does not survive transfer to the autoclave;

m: Made in 2.50 cm diameter cylindrical molds.

While wet gels made with the HCl-catalyzed process do not seem to shrink relative to the molds, RF aerogels do shrink relative to their wet gels upon drying with SCF CO₂. The shrinkage is not related to the R:F ratio, but it does depend on the aging time. Gels processed with no aging at all shrink less (~29%), while gels aged for a prolonged period (1-5 days) shrink more (~39%). Shrinkage is reflected on the bulk density, which is found lowest for samples processed with no aging at all. Skeletal densities are about equal to one another for the different R:F ratios, and porosity (% empty space), Π , calculated from the bulk and skeletal densities (ρ_b and ρ_s , respectively) via $\Pi=100\times[(1/\rho_b)-(1/\rho_s)]/(1/\rho_b)$ is in the 87%-93% range. RF aerogels with the lowest bulk density (those processed with no aging at all) are the ones with the highest porosity. For comparison purposes, Table 1 also includes data for Na₂CO₃-catalyzed gels made here by adhering closely to Pekala's procedure.³ It is noted that such aerogels produced without the prescribed 3-day aging in CF₃COOH do not have the strength required to yield monoliths. On the other hand, gels gone through the CF₃COOH aging process show similar processability to those made by the HCl-catalyzed process in CH₃CN.

Microscopically, HCl-catalyzed RF aerogels consist of a bead-like structure, pretty similar to both the structure of base-catalyzed RF aerogels,¹⁸ and to the typical pearl-necklace-like structure of common base-catalyzed mesoporous silica.^{19,20} Figure 4 compares the SEMs of a HCl-catalyzed RF aerogel and a base-catalyzed silica aerogel. In agreement with SEM, N₂ sorption porosimetry yields characteristic type IV isotherms for mesoporous materials (Fig. 5). The average pore size was calculated by the $4V_{\text{Total}}/\sigma$ method, using values for V_{Total} calculated by two methods: via a single point measurement of the volume of N₂ adsorbed, and via the bulk and skeletal densities (ρ_b

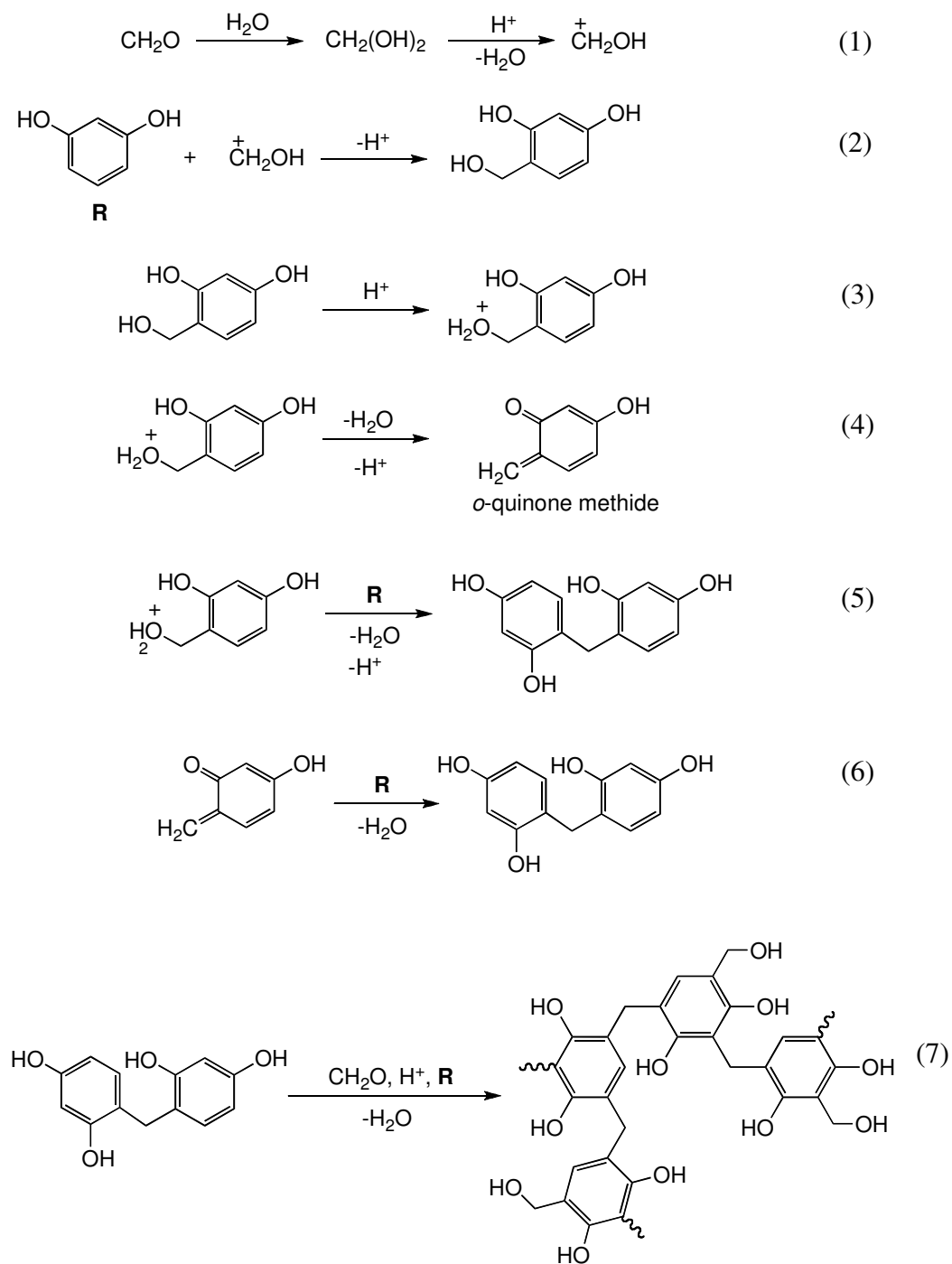
and ρ_s , respectively, see footnote “g” in Table 1). The single point N_2 adsorption method tends to underestimate V_{Total} significantly,²¹ but average pore sizes calculated by that method are still included here for comparison with previously reported data for other kinds of aerogels. Thus, the average pore size by the N_2 adsorption method is in the same range (12-23 nm) as for base-catalyzed mesoporous silica aerogels.²⁰ From Table 1, there is a clear correlation between average pore size, bulk density and porosity: the lower the bulk density, the higher the porosity and the larger the average pore sizes. By the same token, however, specific surface areas, σ , of our HCl-catalyzed RF aerogels measured by the BET method are lower than those of the corresponding base-catalyzed not only RF but also silica aerogels of similar density and pore sizes: 300-500 m^2g^{-1} for HCl-catalyzed RF aerogels versus 700-800 m^2g^{-1} for Na_2CO_3 -catalyzed RF aerogels (Table 1) and $\sim 1000 \text{m}^2\text{g}^{-1}$ for base-catalyzed silica aerogels.^{20b} From the specific BET surface area, σ , and skeletal density, ρ_s , we can calculate the average particle radius r ($=3/\rho_s\sigma$).²² The particle diameters ($=2\times r$) are included in Table 1, and there is a good agreement with the particle sizes observed with SEM and with the particle sizes both calculated (Table 1) and reported for typical base-catalyzed RF aerogels.³

The chemical make up of our HCl-catalyzed RF aerogels was investigated with IR and ^{13}C NMR. The IR spectrum of a typical RF aerogel (Fig. 6) shows the same features to those shown by Na_2CO_3 -catalyzed aerogels,³ with bands at 2942, 2842 and 1479 cm^{-1} associated with the $-\text{CH}_2-$ stretching and bending vibrations, whereas the broad band at 3382 cm^{-1} includes the aromatic OH groups of resorcinol. The band at 1614 cm^{-1} comes from aromatic ring stretches, while medium to weak absorption bands at 1222 cm^{-1} and 1092 cm^{-1} indicate that methylene ether linkages between resorcinol rings are present but

not dominant. Fig. 7 compares the CPMAS ^{13}C NMR spectra of the two extreme compositions of this study, one made with a molar ratio of R:F=1:2 and another one with R:F=1:10. Peak assignment was based on Fig. 1 and reference 23. The resonance at 152 ppm is assigned to phenolic carbons of substituted resorcinol. On the other hand, RF aerogels may include aromatic rings with one-, two- and three-bridges to adjacent rings, giving rise to broad asymmetric resonances. Thus, the peak at 121 ppm with a shoulder at 114 ppm is assigned to aromatic carbons of mono- and di-substituted resorcinols bearing $-\text{CH}_2-$ groups in all *ortho*-positions relative to the phenolic $-\text{OHs}$ (c',d'-carbons). Consistent with the IR spectrum, the smaller peak at 59 ppm is assigned to a small amount of $\text{CH}_2\text{-O-CH}_2$ bridges that apparently decreases as the relative amount of formaldehyde is increased. The broad peak at 30 ppm with shoulder at 24 ppm is assigned to the different types of $-\text{CH}_2-$ bridges. As the relative amount of formaldehyde is increased the intensity of the bridging $-\text{CH}_2-$ carbon increases, indicating incorporation of more formaldehyde into the gel. Integration of the aromatic phenolic carbon peak at 152 ppm vs. the broad peak at 20-40 ppm shows incorporation of 2.5 \times more formaldehyde per aromatic ring in gels made with R:F=1:10 mol ratio, than in gels made with R:F=1:2. Overall, the spectra of both kinds of aerogels (i.e. those made with R:F=1:2 and R:F=1:10) are qualitatively similar to those reported for the Na_2CO_3 -catalyzed RF aerogels at high resorcinol-to-catalyst ratios (R:C=200 and R:C=500),²³ indicating a similar distribution of substitution sites.

5. DISCUSSION

In contrast to the base-catalyzed route to RF aerogels, which is based on activation of the aromatic ring towards electrophilic aromatic substitution by increasing the electron donating ability of the substituents (from $-\text{OH}$ to O^-), the acid-catalyzed route is based on acceleration of the reaction by increasing the positive charge of the electrophile. Comparative data shown in Figures 1 and 3 support this hypothesis: in the same solvent system (CH_3CN) HCl-catalyzed R/F mixtures react and/or gel much faster than non- or base-catalyzed mixtures with a given reactant concentration. But, the choice of solvent is also important: for example, running the same HCl-catalyzed process in acetone rather than in CH_3CN , leads to much slower gelation, presumably because of cross-aldol condensation type of equilibria between the solvent (acetone) and formaldehyde. Scheme 2 summarizes the proposed mechanism for the HCl-catalyzed gelation of resorcinol with formaldehyde. Protonation of formaldehyde (eq 1) is followed by nucleophilic attack by the π -system of resorcinol (eq 2) leading to hydroxymethylation. Subsequently, protonation of a hydroxymethyl group (eq 3) forms $-\text{OH}_2^+$, a good leaving group, that may cleave either unimolecularly (eq 4) leading to *o*-quinone methide-type intermediates (also referred to as *o*-quinomethanes), or bimolecularly (eq 5) after direct attack at the $-\text{CH}_2\text{OH}_2^+$ carbon by the π -system of another resorcinol molecule. The latter process results directly into $-\text{CH}_2-$ bridge formation between phenyl rings at three possible positions. On the other hand, *o*-quinone methides are quite unstable species, having been observed only as transients during pulse radiolysis experiments,²⁴ or in solid argon matrices.²⁵

Scheme 2. Proposed Mechanism for RF Gel Formation under Acid (HCl) Catalysis

At higher temperatures (e.g., ~ 30 °C) *o*-quinone methides start Diels-Alder reactions with one another and form spiro dimers and trimers.^{25b,26} *o*-Quinone methides have been suggested as intermediates in the base-catalyzed condensation of phenol with formaldehyde,²⁷ and their involvement in the HCl-catalyzed RF gel formation is supported by the red color ($\lambda_{\text{max}}=543$ nm, Fig. 2) developing during the process.^{24,28} Thus, *o*-quinone methides may also be attacked by the resorcinol π -system,²⁷ leading also to $-\text{CH}_2-$ bridge formation (eq. 6). At this point it is speculated further that the brick-red color of the RF aerogels may be also associated with a small amount of configurationally locked *o*-quinone methide and/or their spiro derivatives. This hypothesis is consistent with the visual observation that RF aerogels made using a mol ratio of R:F=1:10 are much lighter in color than their 1:2 counterparts, signifying less residual *o*-quinone methides. Further support for this hypothesis comes from the fact that submerging RF aerogels in an aqueous NaBH_4 solution decolorizes them completely, presumably by reduction of *o*-quinone methides to phenols.²⁸ Indeed, after washing to remove NaBH_4 and exposure to the air, gels re-develop their original red color fairly fast. Finally, we need to point out that the acid-catalyzed gelation of our R/F mixtures is exothermic and molds warm up somewhat. But, owing to the small size of our samples no runaway conditions were ever encountered as has been oftentimes reported during synthesis of novolak resins by the acid-catalyzed reaction of phenol with formaldehyde.²⁹

According to the nanomorphology observed in SEM, it seems that polymerization leads to particle formation, followed by phase separation and gelation. SEM results and particle size calculations based on BET surface areas and skeletal densities (Table 1) are internally consistent. Although appearance-wise RF and silica aerogels are very similar

(Fig. 4), surface areas of RF aerogels are significantly lower than those of silica of similar mesostructure (Table 1), reflecting most probably a less elaborate intraparticle structure, for instance a simpler primary-secondary particle hierarchy.

Aging seems to be an important factor for shrinkage and therefore for the bulk density of RF aerogels. It is quite remarkable that Na_2CO_3 -catalyzed gels not gone through the CF_3COOH -treatment swell a lot in acetone and show little structural integrity. On the contrary, similar gels seem more durable after aging in CF_3COOH and although they do not swell in acetone, nevertheless they do shrink as much as our HCl -catalyzed gels having gone through aging. Undoubtedly, swelling of the RF networks indicates flexibility. Now, in silica, where the effect of aging has been studied extensively, there are two well-understood processes taking place during aging: syneresis and dissolution/precipitation of silica at points of negative curvature (the interparticle necks).³⁰ Syneresis (reaction with one another and immobilization of dangling structures on the skeletal backbone) leads to shrinkage, while dissolution/precipitation leads to higher mechanical strength. The dissolution/precipitation process is not possible in the case of RF gels because the $-\text{CH}_2-$ link formation is not reversible. On the other hand, a syneresis-like mechanism via reaction of dangling $-\text{CH}_2\text{OH}$ groups or *o*-quinone methides with neighboring resorcinol moieties is quite possible. Meanwhile, the ratio of $-\text{CH}_2-$ groups in 1:2 and 1:10 RF aerogels (by ^{13}C NMR) shows that at least with 1:2 RF gels, reaction of R with F is not stoichiometrically complete. Therefore, aging allows also for incorporation of more formaldehyde into the network,³¹ which in combination with syneresis results in more $-\text{CH}_2-$ bridging, and thus in a higher degree of contraction when all pore-filling solvents have been removed. This model is consistent with the

trends in shrinkage as a function of the aging time, as well as with the relatively narrow range of surface areas and the particle sizes. No clear trends, however, are identifiable in the skeletal densities, which all fall in the 1.4-1.5 g cm⁻³ range.

6. CONCLUSIONS

Given the technological relevance of RF aerogels as precursors of carbon aerogels, the long preparation process of the former comprises a bottleneck for the use of the latter. Therefore, accelerating the synthesis of RF aerogels is a very important objective.³² Resorcinol-formaldehyde gels chemically similar to those obtained by the usual week-long base-catalyzed aqueous gelation process, can be made within minutes by acid (HCl) catalysis in CH₃CN. It is reasonable to expect that the major impact of this work will be in the availability and cost of carbon aerogels.

7. ACKNOWLEDGEMENTS

We thank the University of Missouri Research Board for financial support.

8. REFERENCES

1. Pierre, A. C.; Pajonk, G. M. *Chem. Rev.* **2002**, *102*, 4243-4265.
2. Ritter, J. A.; Al-Muhtaseb, S. A. *Adv. Mater.* **2003**, *15*, 101-114.
3. Pekala, R. W. *J. Mater. Sci.* **1989**, *24*, 3221-3227.
4. Pekala, R. W.; Alviso, C. T.; Kong, F. M.; Hulsey, S. S. *J. Non-Cryst. Solids* **1992**, *145*, 90-98.
5. Pekala, R. W. U.S. Patent 4,873,218 **1989**.
6. Pekala, R. W.; Schaefer, D. W. *Macromolecules* **1993**, *26*, 5887-5893.
7. Saliger, R.; Bock, V.; Petricevic, R.; Tillotson, T.; Geis, S.; Fricke, J. *J. Non-Cryst. Solids* **1997**, *221*, 144-150.
8. Job, N.; Panariello, F.; Marien, J.; Crine, M.; Pirard, J.-P.; Leonard, A. *J. Non-Cryst. Solids* **2006**, *352*, 24-34.
9. Lu, X.; Caps, R.; Fricke, J.; Alviso, C. T.; Pekala, R. W. *J. Non-Cryst. Solids* **1995**, *188*, 226-234.
10. Lin, C.; Ritter, J. A. *Carbon* **1997**, *35*, 1271-1278.
11. Barbieri, O.; Ehrburger-Dolle, F.; Rieker, T. P.; Pajonk, G. M.; Pinto, N.; Venkateswara Rao, A. *J. Non-Cryst. Solids* **2001**, *285*, 109-115.
12. Merzbacher, C. I.; Meier, S. R.; Pierce, J. R.; Korwin, M. L. *J. Non-Cryst. Solids* **2001**, *285*, 210-215.
13. (a) Brandt, R.; Fricke, J. *J. Non-Cryst. Solids* **2004**, *350*, 131-135. (b) Brandt, R.; Petricevic, R.; Pröbstle, H.; Fricke, J. *J. Porous Mater.* **2003**, *10*, 171-178.
14. Baumann, T. F.; Satcher, J. H. Jr.; Gash, A. E. U.S. Patent Application Publication No. US 2002/0173554 A1.

15. Hansch, C.; Leo, A.; Taft, R. W. *Chem. Rev.* **1991**, *91*, 165-195.
16. (a) March, J. *Advanced Organic Chemistry, Reactions Mechanisms and Structure Fourth Edition*, Wiley: New York, 1992, p 550. (b) March, J. *Advanced Organic Chemistry, Reactions Mechanisms and Structure Fourth Edition*, Wiley: New York, 1992, p 548.
17. Werstler, D. D. *Polymer* **1986**, *27*, 757-764.
18. Lee, J.-Y.; Lee, K.-N.; Lee, H.-J.; Kim, J.-H. *J. Ind. Eng. Chem.* **2002**, *8*, 546-551.
19. Brinker, C. J.; Scherer, G. W. *Sol-Gel Science. The Physics and Chemistry of Sol-Gel Processing*, Academic Press: New York, 1990.
20. (a) Leventis, N.; Elder, I. A.; Rolison, D. R.; Anderson, M. L.; Merzbacher, C. I. *Chem. Mater.* **1999**, *11*, 2837-2845. (b) Leventis, N.; Sotiriou-Leventis, C.; Zhang, G.; Rawashdeh, A.-M. M. *NanoLett.* **2002**, *2*, 957-960. (c) Meador, M. A. B.; Capadona, L. A.; MacCorkle, L.; Papadopoulos, D. S.; Leventis, N. *Chem. Mater.* **2007**, *19*, 2247-2260. (d) Leventis, N. *Acc. Chem. Res.* **2007**, *40*, 874-884.
21. Fricke, J.; Reichenauer, G. *J. Non-Cryst. Solids* **1987**, *95&96*, 1135-1142.
22. Hüsing, N.; Schubert, U.; Mezei, R.; Fratzl, P.; Riegel, B.; Kiefer, W.; Kohler, D.; Mader, W. *Chem. Mater.* **1999**, *11*, 451-457.
23. (a) Ward, R. L.; Pekala, R. W. *Polym. Prepr.* **1990**, *31*, 167-169. (b) Moudrakovski, I. L.; Ratcliffe, C. I.; Ripmeester, J. A.; Wang, L.-Q.; Exarhos, G. J.; Baumann, T. F.; Satcher, J. H. *J. Phys. Chem. B* **2005**, *109*, 11215-11222.
24. Cooksey, C. J.; Garratt, P. J.; Land, E. J.; Ramsden, C. A.; Riley, P. A. *Biochem. J.* **1998**, *333*, 685-691.

25. (a) Morawietz, J.; Sander, W.; Traubel, M. *J. Org. Chem.* **1995**, *60*, 6368-6378.
(b) GuangHua Qiao, G.; Lenghaus, K.; Solomon, D. H.; Reisinger, A.; Bytheway, I.; Wentrup, C. *J. Org. Chem.* **1998**, *63*, 9806-9811.
26. Chiba, K.; Hirano, T.; Kitano, Y.; Taba, M. *Chem. Commun.* **1999**, 691-692.
27. Vollhard, K. P. C.; Schore, N. E. *Organic Chemistry Structure and Function, Fourth Edition*, W.H. Freeman and Company, 2003, p 992.
28. Daquino, C.; Foti, M. C. *Tetrahedron* **2006**, *62*, 1536-1547.
29. Lu, K.-T.; Luo, K.-M.; Lin, S.-H.; Su, S.-H.; Hu, K.-H. *Process Saf. Environ. Prot.* **2004**, *82(B1)*, 37-47.
30. (a) Scherer, G. W. *Langmuir* **1996**, *12*, 1109-1116. (b) Strom, R. A.; Masmoudi, Y.; Rigacci, A.; Petermann, G.; Gullberg, L.; Chevalier, B.; Einarsrud, M.-A. *J. Sol-Gel Sci. Techn.* **2007**, *41*, 291-298.
31. Despetis, F.; Barral, K.; Kocon, L.; Phalippou, J. *J. Sol-Gel Sci. Technol.* **2000**, *19*, 829-831.
32. Wiener, M.; Reichenauer, G.; Scherb, T.; Fricke, J. *J. Non-Cryst. Solids* **2004**, *350*, 126-130.

9. FIGURES

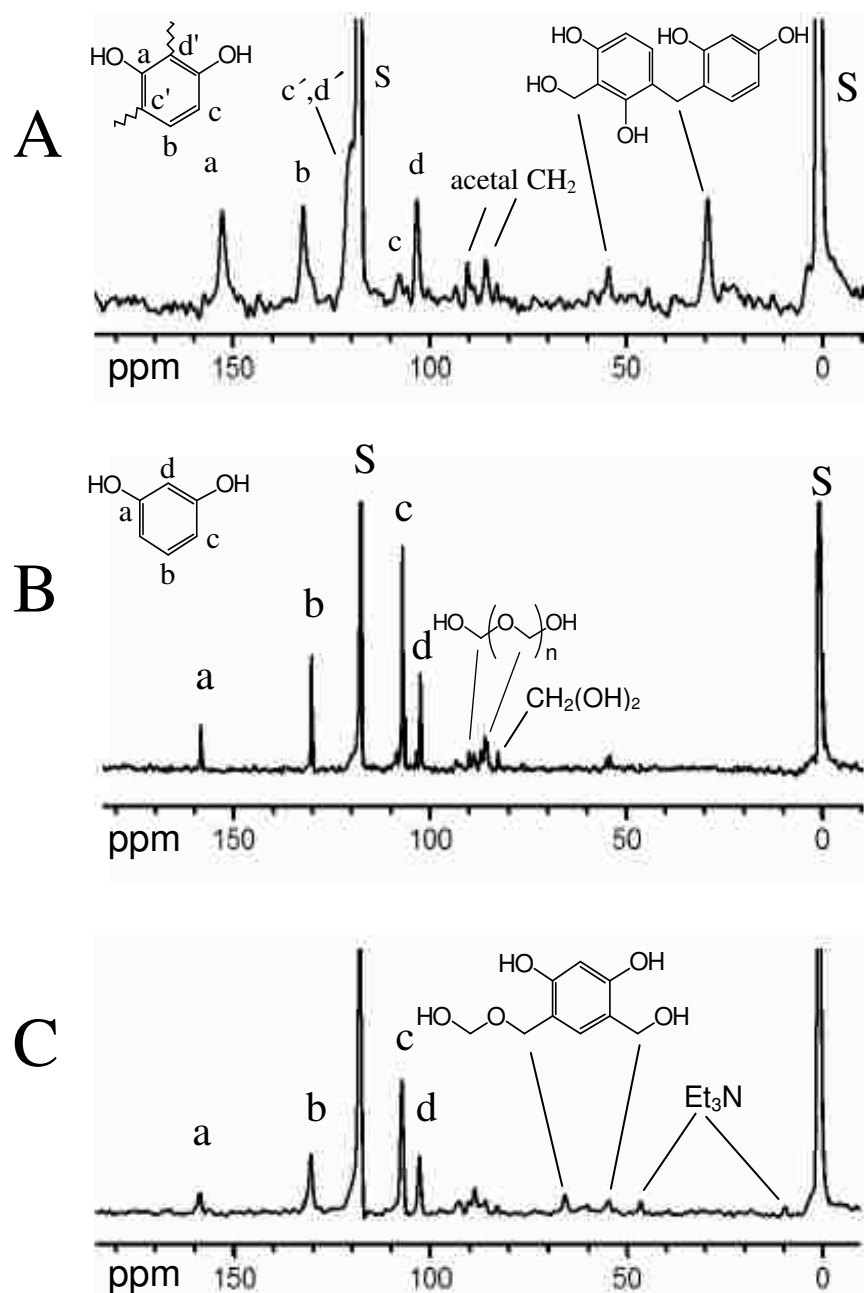


Figure 1. Solution ^{13}C NMR of resorcinol/formaldehyde mixtures in 1:2 mol ratio in CD_3CN . (A) 15 min after mixing, using HCl as catalyst, at room temperature; (B) 15 min after mixing, without any catalyst, at room temperature; and (C) 75 min after mixing, with Et_3N as catalyst, at 80°C . (S: Solvent.)

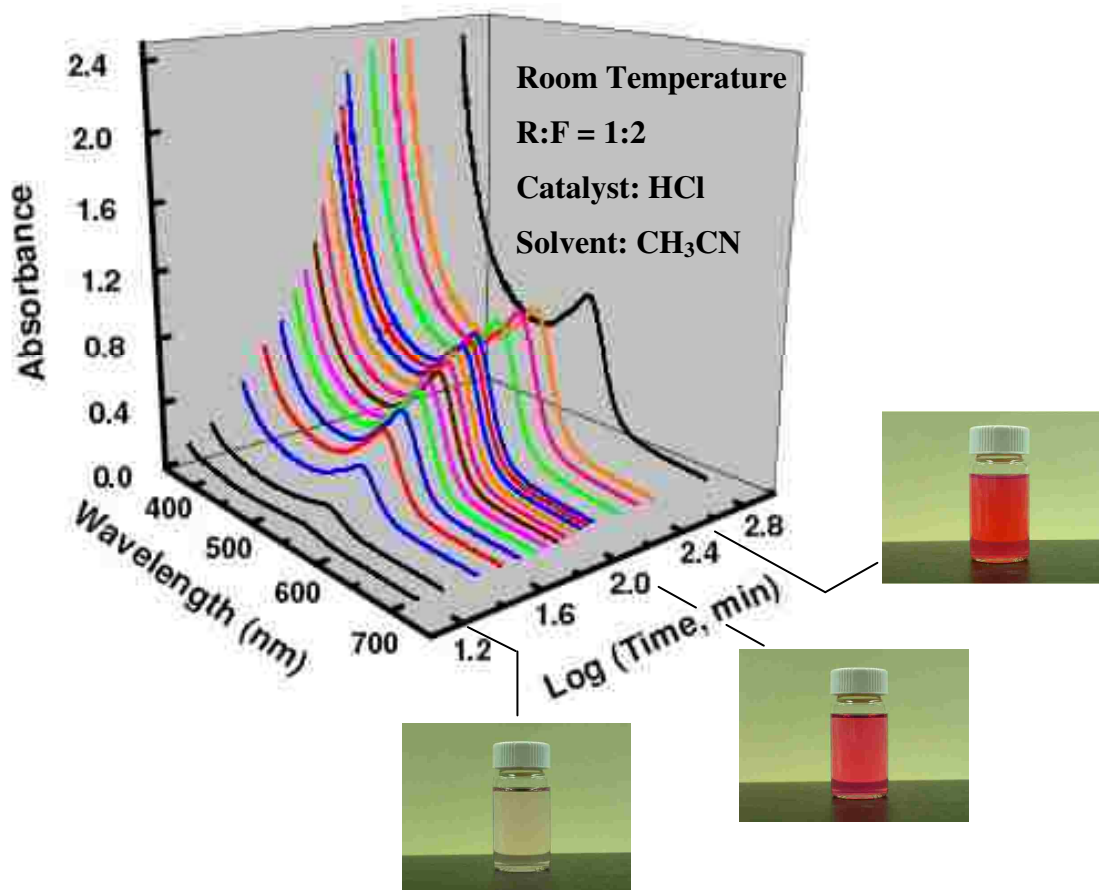


Figure 2. Evolution of the absorbance of a resorcinol/formaldehyde mixture at 1:2 mol ratios in CH₃CN at room temperature. Pictures show snapshots of the red color at the specified points in time

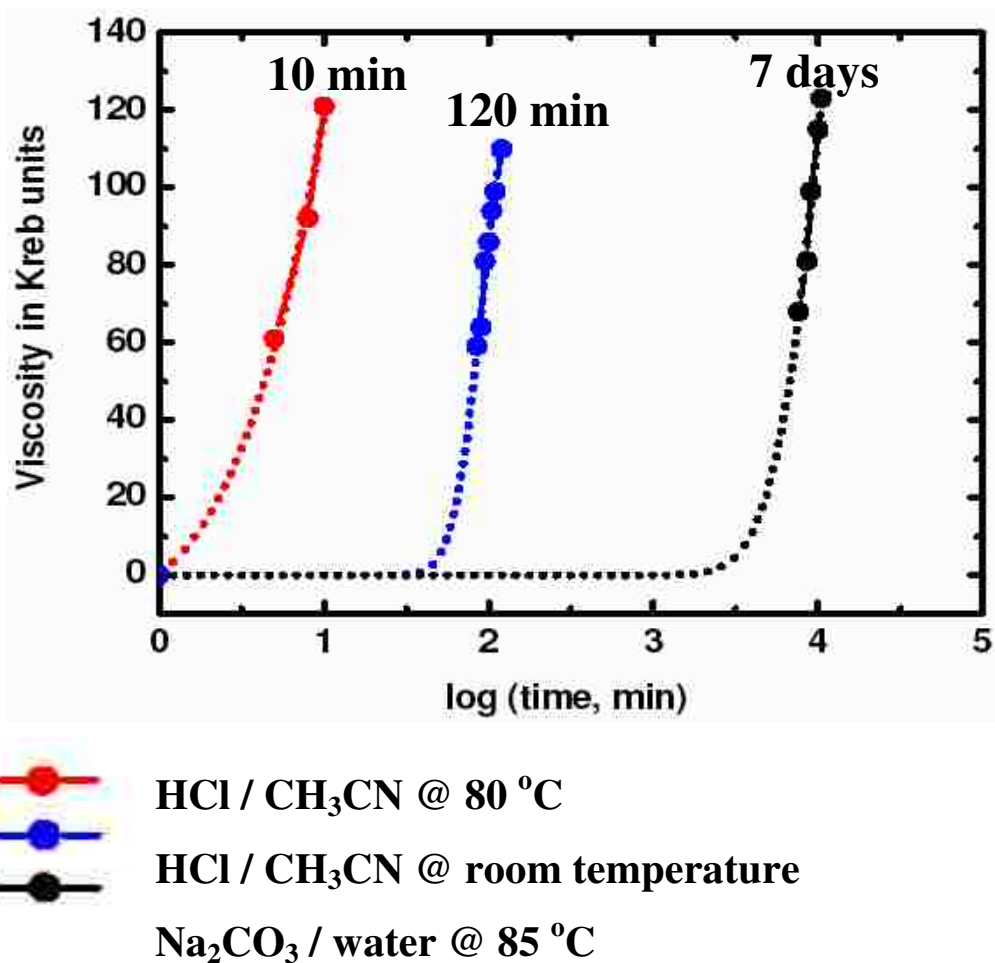


Figure 3. Viscosity evolution of three solutions as indicated, according to ASTM D 562-01. The Stormer Type Viscometer employed was able to register data only above 59 Krebs units. Data collection stopped at the gel point.

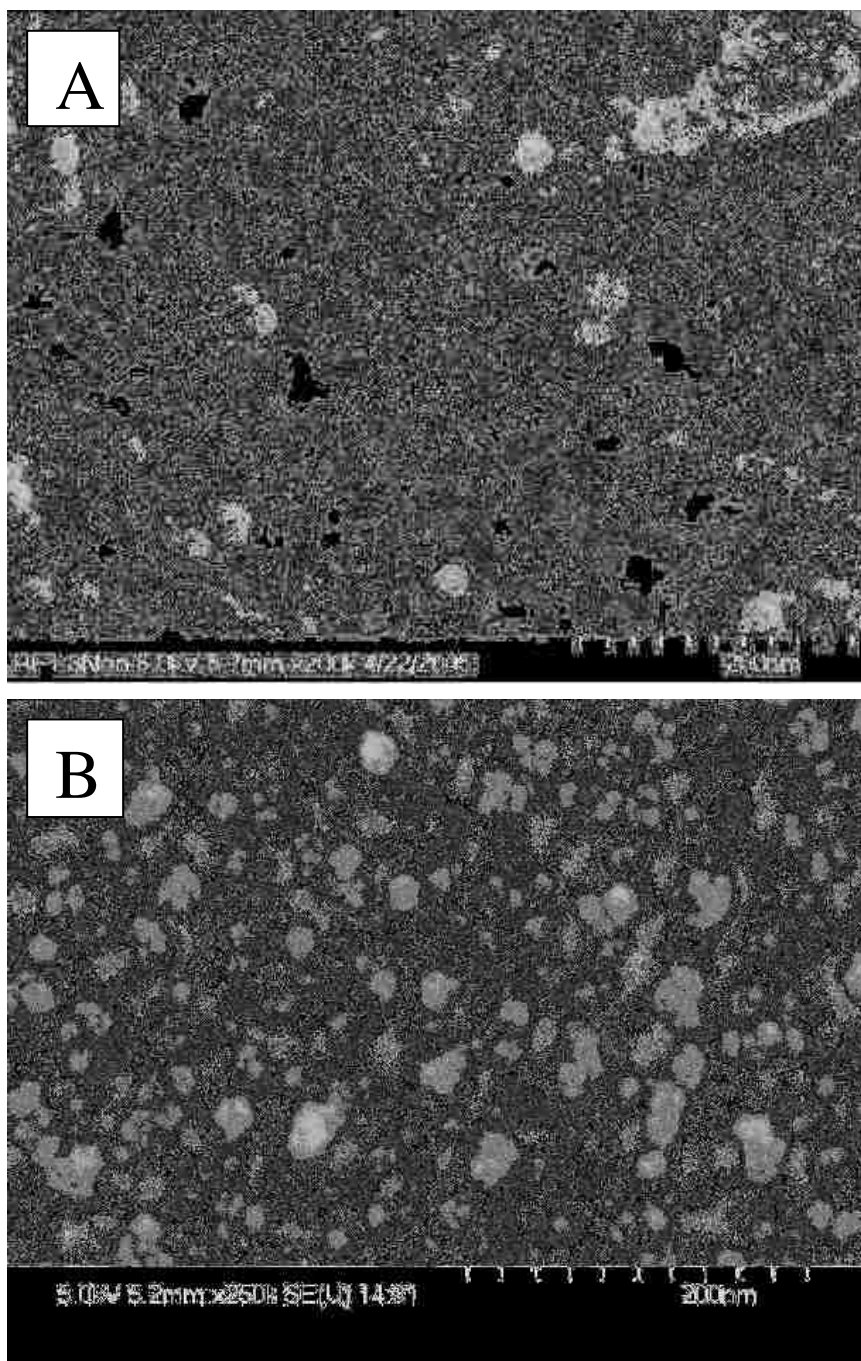


Figure 4. (A) SEM of a RF aerogel (bulk density $\rho_b = 0.175 \pm 0.008 \text{ g cm}^{-3}$) prepared according to Scheme 1, using a mol ratio of R:F=1:3. (B) For comparison, SEM of a native silica aerogel of similar density ($\rho_b = 0.169 \pm 0.004 \text{ g cm}^{-3}$).^{20b}

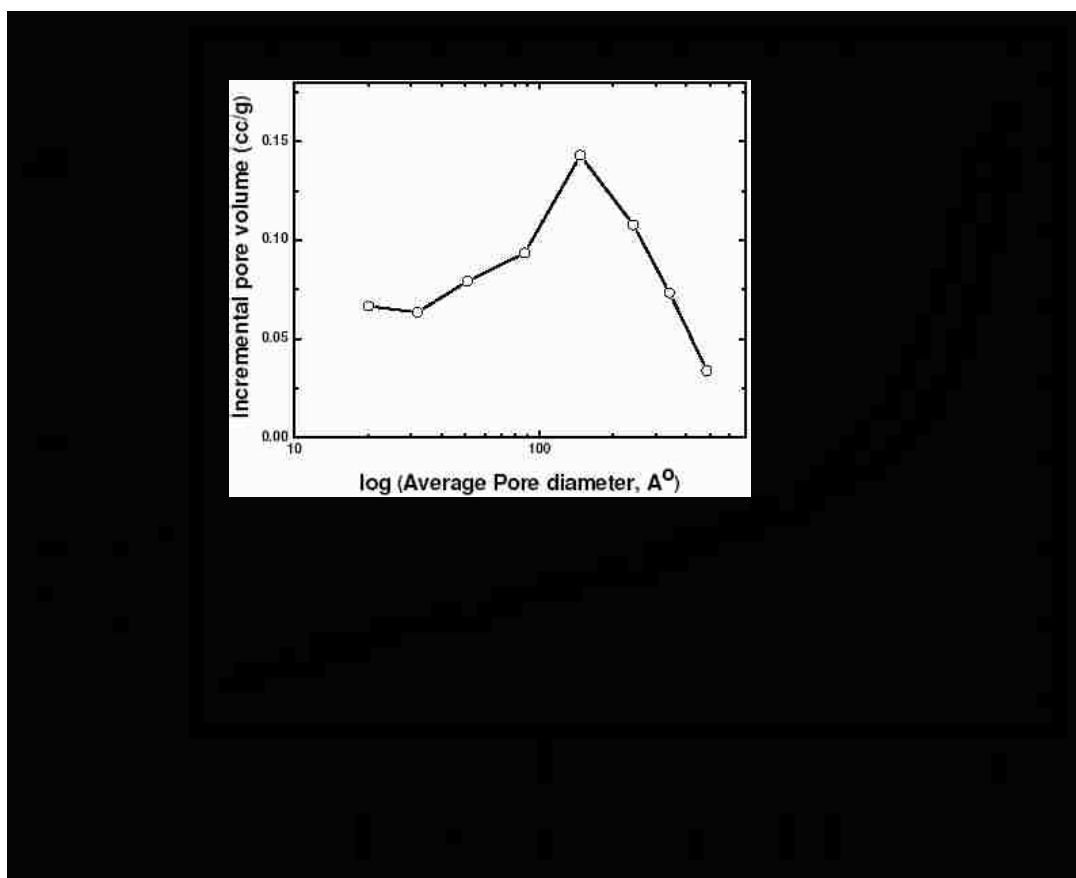


Figure 5. Nitrogen sorption isotherms for a RF aerogel prepared according to Scheme 1 using R:F=1:2 at room temperature, 1 day aging ($\rho_b=0.136\pm 0.008$ g cm⁻³).

Adsorption: ● ; desorption: ○ Inset: BJH-desorption pore size distribution. Results in good agreement with the $4V_{\text{Total}}/\sigma$ by BET method, where V_{Total} was calculated via the single point volume measurement of N₂ adsorption method (Table 1).

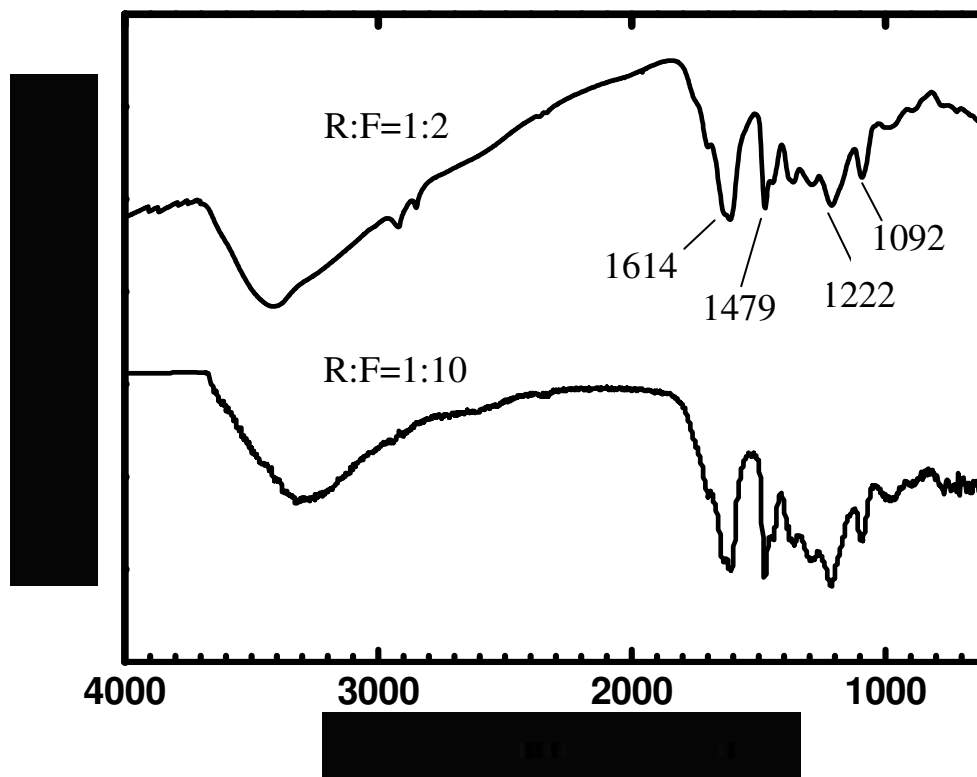


Figure 6. Infrared spectra (in KBr) of two RF aerogels prepared with the R:F ratios indicated.

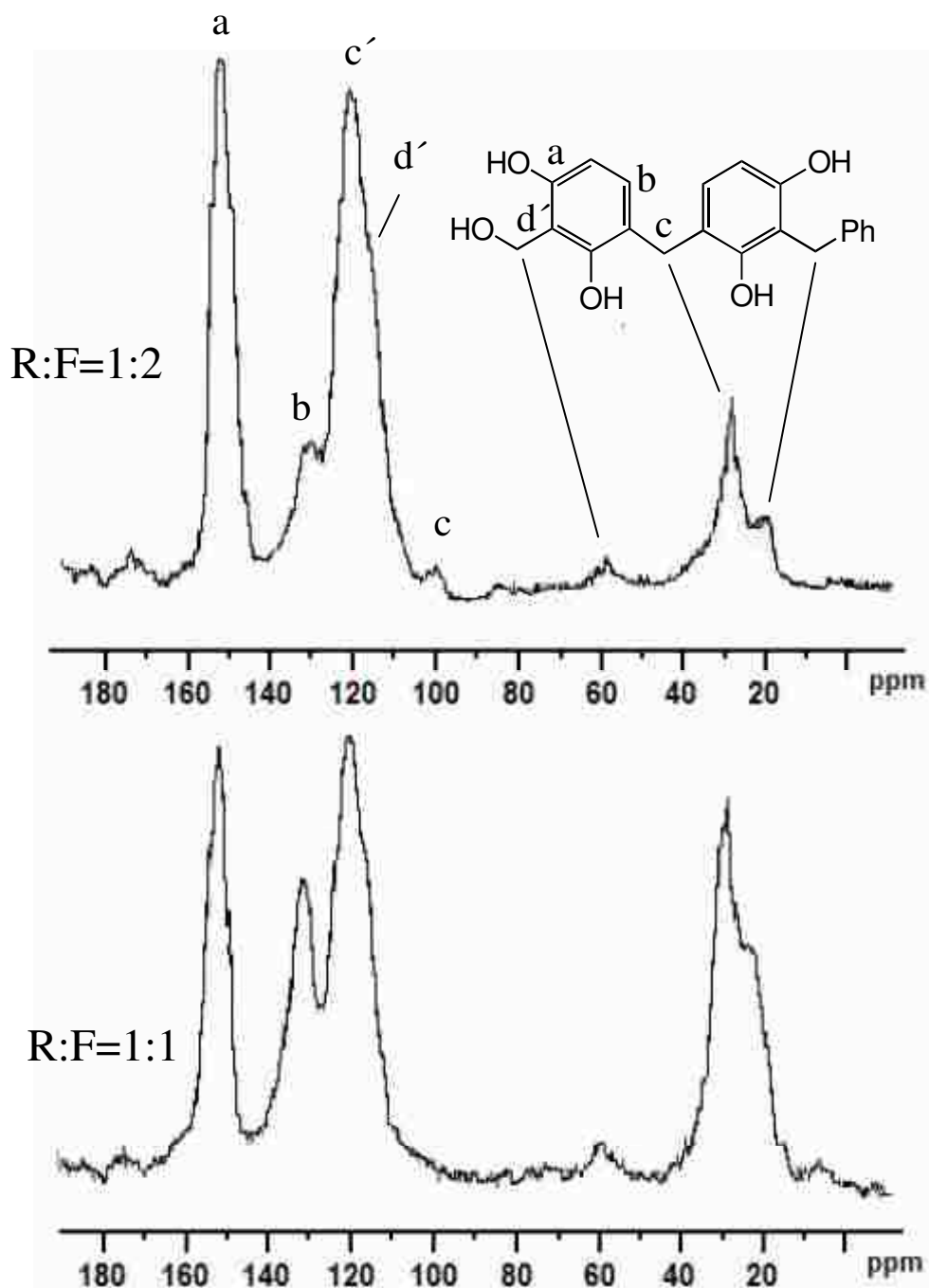


Figure 7. ^{13}C CPMAS NMR of two RF aerogels as indicated. Higher content of formaldehyde in the sol results in more $-\text{CH}_2-$ bridges. Relative integration of the resonances at 152 and 30 ppm indicates that gels prepared with 1:10 R:F ratio incorporate 2.5 times more bridging $-\text{CH}_2-$ than gels prepared with 1:2 R:F ratio.

PAPER III**MACROPOROUS ELECTRICALLY CONDUCTING CARBON NETWORKS BY
PYROLYSIS OF ISOCYANATE-CROSSLINKED RESORCINOL-
FORMALDEHYDE AEROGELS**

Sudhir Mulik, Chariklia Sotiriou-Leventis* and Nicholas Leventis*

Department of Chemistry, Missouri University of Science and Technology
(formerly, University of Missouri-Rolla), Rolla, MO 65409.

Prepared for Publication in *Chemistry of Materials*.

1. ABSTRACT

Carbon (C-) aerogels are made by pyrolysis under Ar of resorcinol-formaldehyde (RF) aerogels, and combine electrical conductivity with a high open mesoporosity. Nevertheless, since macropores are known to facilitate mass-transfer, they could be beneficial for applications in separations or in fuel cell and battery electrodes. Macropores are typically incorporated in C-aerogels during gelation of the RF precursors by using either “hard” templating with silica or polystyrene beads, or “soft” templating with self-assembled surfactants. Here, we report an alternative method, where an open macroporosity is introduced by pyrolysing RF aerogels whose skeletal nanoparticles have been crosslinked chemically with an isocyanate-derived polymer that coats conformally the entire RF framework. The structural, physical and chemical evolution of the X-RF network was monitored at various stages during pyrolysis by DSC, TGA, SEM, N₂ adsorption porosimetry and ¹³C-NMR. The accumulated evidence shows that the crosslinker first loses its chemical bonding with the skeletal nanoparticles, then it melts

before it decomposes exerting surface tension forces on the RF framework, which cause a partial structural collapse that creates macropores. A xerogel-like internal texture of the macroporous walls is responsible for close contact of the carbon skeletal nanoparticles, resulting in an about 7× lower bulk electrical resistivity of the macroporous material relative to the corresponding mesoporous network obtained by pyrolysis of native (i.e., non-crosslinked) RF aerogels. The new macroporous material was evaluated electrochemically for possible application as an electrode in batteries and fuel cells.

2. INTRODUCTION

Carbon (C-) aerogels are made by pyrolysis (also referred to as carbonization) of resorcinol-formaldehyde (RF) aerogels at 600-2100 °C under inert atmosphere.¹ Since C-aerogels combine electrical conductivity with typical aerogel properties such as low density, open mesoporosity (pore sizes less than 50 nm) and high surface area,² they are considered for a wide variety of applications ranging from media for separations (e.g., HPLC), to non-reflective panels, to materials for hydrogen storage, to anodes in lithium ion batteries or electrodes for supercapacitors.³⁻⁸

Providing monolithic carbon or films with either stereoregular (ordered or periodic) mesoporosity or macroporosity (pore diameters > 50 nm) can be beneficial for applications ranging from fuel cell electrodes to photonic crystals.^{9,10,11} Ordered mesoporosity and macroporosity are typically introduced by using templating agents during gelation, like for example monodispersed beads of polystyrene or silica, which are removed from the wet gels by dissolving in toluene or HF, respectively, or self-

assembled surfactant aggregates, which decompose during carbonization of the surrounding RF matrix.^{12,13}

In this paper, we discuss an alternative method for producing robust macroporous carbon aerogels by pyrolysis of isocyanate-crosslinked RF aerogels. The logic behind our process design was based on prior thermogravimetric analysis data for isocyanate-crosslinked silica aerogels showing complete decomposition of the polymeric crosslinker,¹⁴ thereby suggesting that pyrolysis of RF aerogels in intimate contact with an isocyanate-derived polymer would yield carbon perforated by the voids created from gases evolving during decomposition of the crosslinker. As it turns out, our working hypothesis was only partially correct. First, crosslinking of RF wet gels proceeds smoothly in analogy to silica. The process stabilizes the RF skeletal framework against shrinkage, yielding sturdy lightweight materials with densities lower even than those of their native counterparts. Subsequently, during pyrolysis the crosslinker melts before it decomposes, thereby exerting surface tension forces, which transform the mesoporous RF network into a macroporous one that upon carbonization is converted to a new electrically conducting material with morphology and properties different from those of typical carbon aerogels obtained from native (non-crosslinked) RF aerogels. The new macroporous carbon aerogels were evaluated electrochemically for possible application as electrode materials in batteries and fuel cells.

3. EXPERIMENTAL

3.1 Materials

Formaldehyde (37% aqueous solution methanol stabilized) and acetone (anhydrous) were used as received from Aldrich Chemical Co. Acetonitrile (ACS reagent grade) and hydrochloric acid (12.1 N) were purchased from Fisher Scientific. Resorcinol received from Aldrich was sublimed before use. Triethylamine was obtained from Acros Chemicals and was further purified by distillation over calcium hydride. Diisocyanate crosslinkers Desmodur N3200 and Desmodur N3300 were obtained courtesy of Bayer Corporation (Pittsburg, PA). Siphon grade CO₂ was obtained from BOC Gases, Murray Hill, N.J. supplied locally by Ozarc Gases. For electrochemistry, a platinum disk working electrode (2.0 mm diameter, 0.0314 cm²) and a Ag/AgCl/aqueous KCl (3 M) reference electrode were purchased from CH Instruments, Inc. (Austin, TX). The counter electrode was constructed from a Pt mesh (Aldrich). Disk working electrodes were polished successively with 6, 3, and 1 μm diamond paste (Struers Inc., Westlake, OH), washed with water and acetone, and air-dried. Ferrocene (Aldrich-sublimed) was used as a reference redox system. Platinum electrodeposition was carried out using potassium tetrachloroplatinate (Aldrich) as the Pt source. Tetrabutylammonium perchlorate (TBAP) was used as supporting electrolyte and was prepared as described previously.¹⁵

3.1.1 Preparation of native RF aerogels

RF wet gels with a 1:2 mol R:F ratio were prepared by mixing at room temperature solution “A” containing 0.337 g (0.003 mol) of resorcinol, 0.477 mL (0.006 mol) of the commercially available formaldehyde solution and 11.5 mL CH₃CN, with

solution “B” containing 0.636 mL CH₃CN and 0.03 mL (0.363 mmol) of concentrated HCl as catalyst, as we reported recently.¹⁶ The mixture (sol) was poured into molds (either Wheaton polypropylene Omni-Vials, part No. 225402, 1.04 cm in diameter, or 10 mL AirTite Norm-Ject syringes without needles supplied by Fisher) and gelation occurs within two hours at room temperature or in about 10 min at 80 °C. Typically, the resulting gels were aged in their molds at room temperature for 24 h, and subsequently they were washed with acetone (3×, 8 h, 4× the volume of the gel each time) and they were dried in an autoclave with liquid CO₂, taken out at the end supercritically to obtain native RF aerogels.

3.1.2 Preparation of isocyanate-crosslinked RF aerogels

The crosslinking solution was prepared by mixing 11 g of isocyanate oligomer (Desmodur N3200 or Desmodur N3300A) in 94 mL of anhydrous acetone with or without 0.117 mL (0.1% w/w) of anhydrous triethylamine (TEA) as a catalyst. After wet gels were washed with acetone (3×, 8 h, 4× the volume of the gel each time), they were placed in the crosslinking solution and the isocyanate crosslinker was allowed to diffuse into the pores of the wet gels and to equilibrate for 24 h. After heating at 55 °C for another 24 h, the containers were cooled to room temperature and gels were removed and placed in fresh acetone. After further washing with acetone (3×, 8 h, 4× the volume of the gel each time) wet gels were dried in an autoclave with liquid CO₂, taken out at the end supercritically to form crosslinked RF aerogels (X-RF aerogels).

3.1.3 Preparation of polyurea aerogels

Control polyurea aerogels were prepared by mixing at room temperature 11 g of Desmodur N3300A, 94 mL of acetonitrile or acetone, 0.19 mL of distilled water and 0.35 mL (0.3 % weight per total weight of Desmodur N3300A plus solvent) of triethylamine (TEA). The resulting sol undergoes gelation within 30 min. After 24 h of aging, wet polyurea gels were washed with acetone (3×, 8 h, 4× the volume of the gel each time) and dried in an autoclave with liquid CO₂, taken out supercritically.

3.1.4 Preparation of carbon aerogels

Native RF aerogels and their X-RF counterparts crosslinked with either Desmodur N3200 or Desmodur N3300A were pyrolyzed at 800 °C for 3 h in a tube furnace under a flowing stream of Ar. Prior to pyrolysis, the tube was purged with Ar for 10 min before heating was initiated at a rate of 5 °C min⁻¹. At the end of the heating period, the power to the furnace was disconnected and the tube was allowed to cool slowly back to room temperature under flowing Ar. For control purposes, pyrolysis of X-RF aerogels was also conducted at 200 °C, 250 °C and 300 °C under the same conditions.

3.2 Methods

Supercritical fluid (SCF) CO₂ drying was carried out using an autoclave (SPI-DRY Jumbo Supercritical Point Drier, SPI Supplies, Inc., West Chester, PA). Bulk densities were calculated from the weight and the physical dimensions of the samples. In cases of irregularly shaped samples, where measurement of the physical dimensions was not possible, sample volumes were determined using the mercury displacement method.

Skeletal densities were determined by helium pycnometry using a Micromeritics AccuPyc II 1340 instrument. Mesoporous surface areas and pore size distributions were measured by nitrogen adsorption/desorption porosimetry using a Quantachrome Autosorb-1 Surface Area/Pore Distribution analyzer. Samples for surface area and skeletal density determination were degassed at 80 °C for 24 h before analysis. Scanning electron microscopy (SEM) and energy-dispersive x-ray spectroscopy (EDS) were conducted with a Hitachi S-4700 field emission microscope. RF aerogel samples for SEM were sputter-coated with Ag/Pd for 2 min to avoid charging; that treatment was not necessary for carbon aerogels because they were electrically conducting. Chemical characterization of native as well as crosslinked RF aerogels was based on IR and solid state ^{13}C -NMR. Infrared spectra were obtained in KBr pellets using a Nicolet-FTIR Model 750 Spectrometer. Solid ^{13}C -NMR spectra were obtained with samples ground in fine powders on a Bruker Avance 300 Spectrometer with 75.475 MHz carbon frequency, using magic angle spinning (5 kHz) with broad band proton suppression and the CPMAS TOSS pulse sequence for spin sideband suppression. ^{13}C -NMR spectra were externally referenced to the carbonyl of glycine (196.1 ppm relative to tetramethylsilane). Thermogravimetric analysis (TGA) was conducted under nitrogen with a TA Instrument, model Hi-Res-TGA 2950 using a heating rate of 10 °C min⁻¹. Modulated Differential Scanning Calorimetry (MDSC) was conducted under nitrogen from 30 °C to 300 °C with a TA Instrument Model 2920 apparatus at a heating rate of 10 °C min⁻¹. The mass of each sample was approximately 8-12 mg.

Four-point-probe conductivity measurements were conducted on flat surfaces of rectangular blocks of carbon aerogel samples (made with a fine sand paper) using an

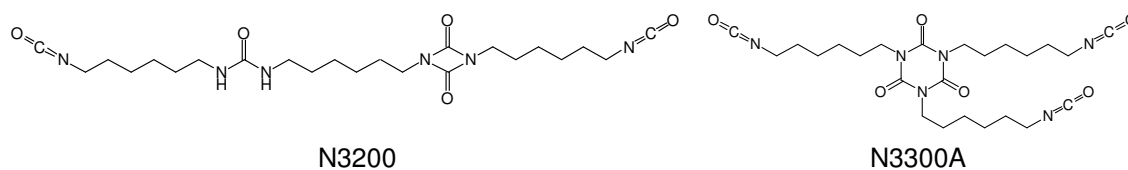
Alesis contact probe station Model CPS -06 with a Cascade Microtech electrode Model C4S-44/5S. The reliability of the probe was confirmed with silicon wafers and indium-tin-oxide coated glass slides of known sheet resistance. Electrochemical evaluation of carbon aerogels was conducted using standard millielectrode cyclic voltammetry with a Pt disk electrode (2 mm diameter), an EG&G 263A potentiostat controlled by the EG&G model 270/250 software and ferrocene (3 mM) in CH₃CN/0.1 M TBAP as a reference redox system. Platinum electrodeposition using carbon aerogels as working electrodes was conducted potentiostatically (at 0.0 V versus aq. Ag/AgCl) from a potassium tetrachloroplatinate solution (II) (3 mM) in CH₃CN/0.1 M TBAP (using a minimal amount of water in order to dissolve K₂PtCl₄) and the charge passed was calculated by integration of the current-time trace recorded on a Kipp & Zonen X-Y recorder.

4. RESULTS AND DISCUSSION

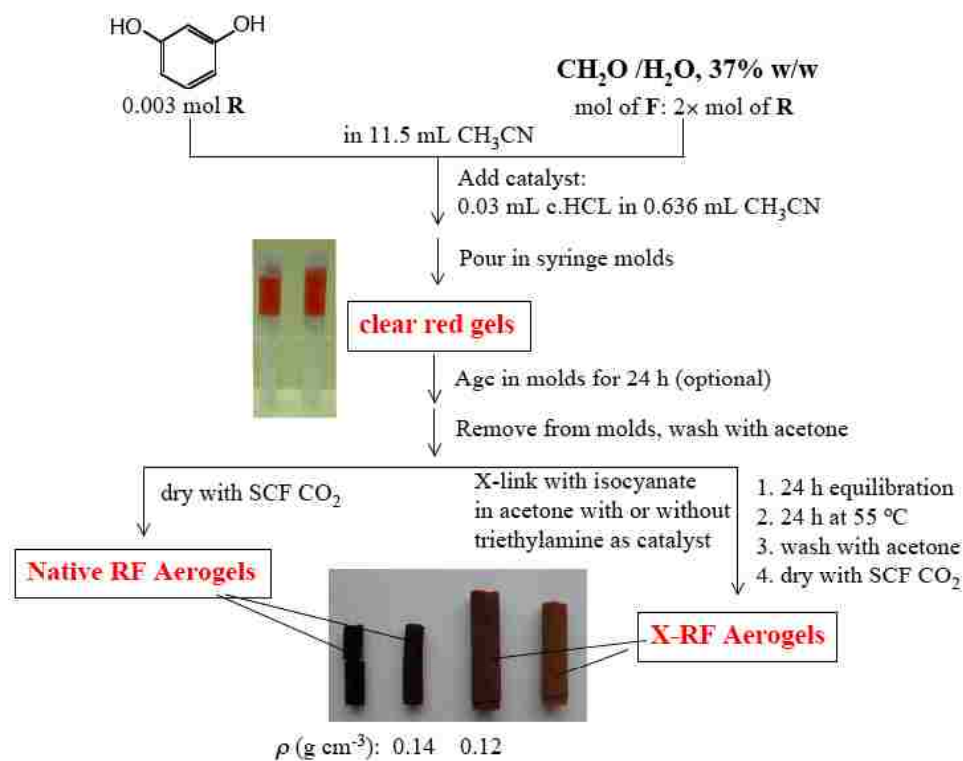
4.1 Native RF aerogels and their crosslinking with isocyanates

Native RF wet gels were prepared using our recently reported time-efficient HCl-catalyzed route in CH₃CN (Scheme 1).¹⁶ By that method gelation takes place at room temperature within 2 h (or in 10 min at 80 °C), as opposed to the usual aqueous base-catalyzed gelation that requires a week-long incubation at 80 °C.¹ Native RF aerogels were obtained by SCF CO₂ drying of RF wet gels, and microscopically they are indistinguishable from typical base-catalyzed silica aerogels,¹⁶ consisting of a pearl-necklace-like structure of secondary particles (40-70 nm), which in turn consist of primary particles (10-12 nm in diameter – see Figure 1A). Furthermore, by TGA native RF aerogels show a mass loss of 6% up to 80 °C, with a simultaneous DSC endotherm at

65 °C (Figure 2). This behavior is identical to the one exemplified by native silica aerogels and indicates gelation water remaining adsorbed (presumably through hydrogen bonding) on the nanoparticles even after the SCF CO₂ drying process. Water remaining adsorbed on silica has been used extensively for crosslinking the skeletal nanoparticles with polyurea;¹⁴ for this, di- or tri-isocyanates are introduced in the mesopores and they first get anchored to the skeletal silica network via carbamates formed by reaction with surface silanols. Subsequently, dangling isocyanates are hydrolyzed by the gelation water remaining adsorbed on the skeletal silica framework yielding amines, which in turn react with more isocyanate in the mesopores, resulting in interparticle polymeric bridges of polyurea.¹⁴ Since the surface of the RF particles has both hydroxyls (from resorcinol and from terminal -CH₂OH groups) and adsorbed water, a similar crosslinking chemistry to that working on silica was adopted for RF aerogels (Scheme 1): RF wet gels were placed in acetone solutions of Desmodur N3200 (a diisocyanate) or Desmodur N3300A (a triisocyanate), and they were left to equilibrate for 24 h at room temperature before they were heated at 55 °C for another 24 h. In a preferred modified version of this process the crosslinking reaction was catalyzed by triethylamine (TEA). The amount of the catalyst is important, because it turns out that a small excess of catalyst in the presence of a low concentration of water catalyzes the gelation of the crosslinker itself (see Experimental section and Section 3.2 below). After crosslinking, unreacted isocyanate was removed from the mesopores by washing with acetone and crosslinked wet gels were dried into crosslinked X-RF aerogels in a similar fashion as their native counterparts. Key properties of RF and X-RF aerogels are cited in Table 1.



Scheme 1. Synthesis of native and isocyanate crosslinked resorcinol-formaldehyde aerogels (RF and X-RF, respectively)



Both native and crosslinked RF aerogels shrink during the SCF drying process. Shrinkage is quantified by comparing a linear dimension such as the diameter of monolithic samples relative to their molds. As shown by the photographs of Scheme 1,

native RF aerogels shrink significantly (up to 39%), while all crosslinked samples shrink much less (Table 1). Furthermore, crosslinking in the presence of a catalyst (TEA) produces X-RF aerogels that shrink even less (13-15%) than X-RF aerogels prepared with no catalyst (21-22%). The latter is attributed to a more extensive crosslinking (see same section below).

Thermogravimetric analysis is not reliable for the determination of the amount of the material uptaken during crosslinking. In contrast to crosslinked inorganic aerogels (e.g., silica, rare earths, vanadia), where the backbone is thermally stable,^{14,17} in X-RF aerogels both the RF backbone and the material uptaken by crosslinking are heat-sensitive and the decomposition of the latter is convoluted with the decomposition of the former. Instead, the amount of material uptaken by the crosslinking process is calculated via eq. 1, which is based on the relative density and volume data of the native versus the X-RF samples. The results are included in Table 1 (see % polymer w/w column).

$$\text{polymer weight percent} = \left[1 - \left[\left(\frac{\text{diameter}_X}{\text{diameter}_{\text{native}}} \right)^3 \left(\frac{\rho_X}{\rho_{\text{native}}} \right) \right]^{-1} \right] \times 100 \quad (1)$$

Despite that X-RF aerogels consist of 46-59% w/w of new material uptaken during treatment with isocyanate their bulk density is generally lower than that of the native RF aerogel samples (Table 1); this is attributed directly to the fact that X-aerogels shrink less. For the same reason, the porosity of all samples, either native or crosslinked, remains about constant. Microscopically, X-RF aerogels show an identical morphology to the native samples (Figure 1B), signifying that the isocyanate-derived material is added

conformally on the skeletal nanoparticles, as designed. According to SEM, both native and crosslinked samples include pores in the threshold of mesopores and macropores (50 nm range). N₂ sorption isotherms do not reach saturation but they can still be classified as Type IV characterizing mesoporous materials (Figure 3). The internal surface area, σ , is derived from the linear lower partial pressure part of the isotherms according to the Brunauer, Emmett, Teller (BET) method¹⁸ and results are also cited in Table 1. Crosslinked samples have up to 20% *higher* surface areas than their native counterparts. This is opposite to what has been observed before with any other kind of polymer crosslinked aerogels, and most probably it is due to two reasons: (a) the fact that X-RF aerogels experience significantly less drying shrinkage than their native counterparts; and (b) the crosslinker derived coating is porous. Average particle diameters were calculated based on skeletal density and BET surface area data (see footnote \underline{e} in Table 1)¹⁹ and they all fall in the 12-14 nm range, in agreement with the primary particles observed by SEM. Average pore diameters have been calculated via the $4 V_{Total} / \sigma$ method using V_{Total} values calculated either via a single-point measurement of the (highest) volume of N₂ adsorbed, or via the bulk and skeletal density of the material (see footnote d in Table 1). The single-point method tends to underestimate V_{Total} .¹⁶ The average pore diameters via V_{Total} calculated using the densities method fall in the 70-80 nm range, in agreement with SEM. Chemical changes brought about by the crosslinking process have been followed with CPMAS solids ¹³C-NMR spectroscopy. Figure 4A shows the ¹³C-NMR spectrum of a typical native RF sample with peak assignment as shown.¹⁶

Table 1. Physical characterization of native and isocyanate crosslinked RF aerogels processed under various conditions.

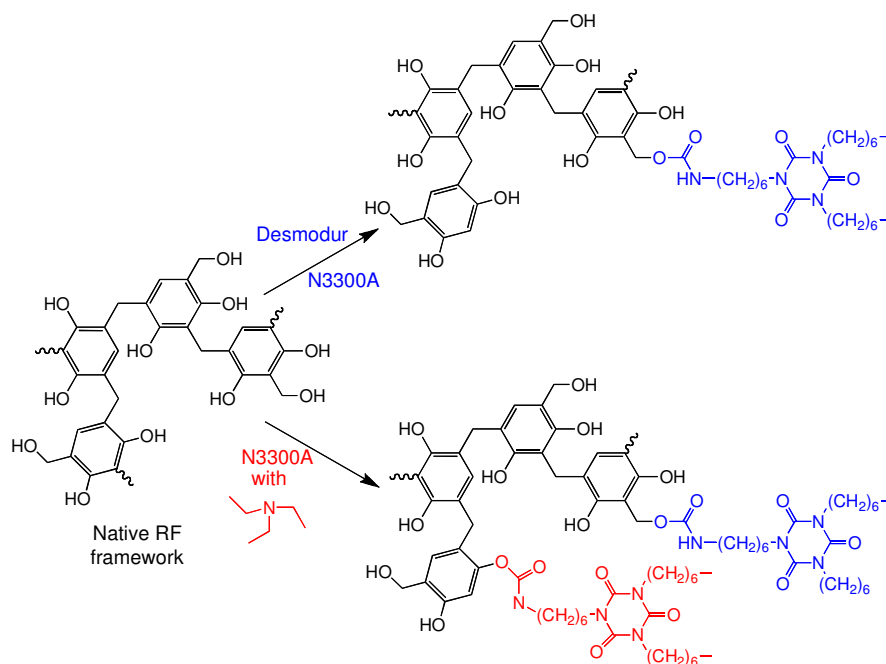
Crosslinker and Conditions	Monolith Diam. ^{a,b} (cm)	Monolith Dia. Shrinkage %	Bulk Density ^b (ρ_b , g cm ⁻³)	Skeletal Density ^c (ρ_s , g cm ⁻³)	% Polymer (w/w)	Porosity, Π (% void space) ^d	BET surf. Area, σ [Av. Pore Diam. ^e] (m ² g ⁻¹ [nm])	Particle Dia. ^f (nm)
-	0.65 ± 0.02	39	0.136 ± 0.008	1.363 ± 0.056	-	90	318 [14.7,83.3]	13.8
N3200	0.83 ± 0.02	21	0.135 ± 0.005	1.288 ± 0.032	52	90	363 [7.5,73.1]	12.8
N3200 + 0.1% w/w TEA	0.89 ± 0.01	15	0.126 ± 0.004	1.234 ± 0.017	58	90	396 [8.3,72.0]	12.3
N3300A	0.82 ± 0.01	22	0.125 ± 0.006	1.323 ± 0.039	46	91	387 [8.4,74.9]	11.7
N3300A + 0.1% w/w TEA	0.91 ± 0.01	13	0.120 ± 0.005	1.196 ± 0.023	59	90	396 [7.8,75.7]	12.7

a: Mold diameter = 1.04 cm. *b*: Average of 3 samples. *c*: One sample, average of 50 measurements. *d*: Porosity, $\Pi = [(1/(\rho_b) - 1/(\rho_s))/(\rho_b)] \times 100$. *e*: By the $4V_{Total}/\sigma$ method, where V_{Total} is the mass specific total pore volume, and has been calculated by two methods, hence the two numbers cited for the Average Pore Diameter: first automatically by the system software from a single point volume measurement of the N_2 adsorbed, and second manually from the bulk and skeletal densities via $V_{Total} = (1/\rho_b) - (1/\rho_s)$. *f*: Particle Diameter = $6/\rho_s\sigma$.

If there were any unreacted isocyanate groups from N3300A they should appear at 128 ppm overlapping with the 130/120 ppm pattern of RF.^{14,16} However, no unreacted isocyanate has been detected by IR (shown in Supporting Information). In fact, the characteristic pattern of RF in the 120-130 ppm range remains unchanged after crosslinking with no catalyst (Figure 4B), meaning that interaction of the isocyanate with the RF framework has taken place only at the terminal $-\text{CH}_2\text{OH}$ groups on its surface. Finally, the sharp, symmetric resonance of the phenolic carbon ($\underline{\text{C}}\text{-OH}$) of RF at 151 ppm (Figure 4A) is expected to partially overlap with the isocyanurate carbonyls at ~ 148 ppm, and both the carbamate and the urea carbonyls at 157 ppm and at 159 ppm, respectively.¹⁴ Indeed, after crosslinking, the 151 ppm peak becomes broad and asymmetric with shoulders at 158 ppm (carbamate and urea) and at 148 ppm (isocyanurate of N3300A). By using TEA as a catalyst, the spectrum changes drastically (Figure 4C). The relative intensity of the hexamethylene groups of N3300A is increased, meaning a higher incorporation of N3300A derived polymer, in agreement with the conclusions arrived at via eq 1. A second observation is that the aromatic carbon pattern in the 130-120 ppm range has changed dramatically: the intensity of the 120 ppm resonance has decreased and the whole pattern has become broader. Those changes are attributed to a direct involvement of the phenolic hydroxyls in reactions with the isocyanate to form carbamates. Changes observed in the carbonyl range 160-150 ppm are consistent with this argument: a new peak at 156 ppm can be explained by the newly formed carbamates via reaction of isocyanates with phenolic hydroxyls on the surface of the RF nanoparticles. Phenolic $\underline{\text{C}}\text{-OH}$ carbons are not expected to move more than a couple of ppm by forming carbamates,²¹ thus the 152 ppm resonance is assigned to both kinds of

aromatic $\underline{\text{C}}\text{-OH}$ and $\underline{\text{C}}\text{-O-CO-NH-}$ carbons. The shoulder at 148 ppm is again assigned to the isocyanurate carbonyls of N3300A. Overall, $^{13}\text{C-NMR}$ confirms an increased uptake of polymer by using TEA as a crosslinking catalyst and indicates a higher degree of crosslinking involving more active sites on the skeletal framework. That in turn explains the lower shrinkage of X-RF aerogels prepared in the presence of TEA (Table 1). Similar results have been obtained by crosslinking with Desmodur N3200 in the presence of TEA (refer to the Supporting Information). Scheme 2 summarizes the crosslinking chemistry with and without TEA.

Scheme 2. Crosslinking of an RF network with and without TEA as crosslinking catalyst.



4.2 Preparation of polyurea aerogels

Results obtained by pyrolysis of X-RF aerogels (see Section 3.3 below) render necessary an investigation of the behavior under similar conditions of the material

derived by hydrolysis and condensation of Desmodur N3200 and N3300A by themselves. Thus, triethylamine was added as a catalyst in acetone/water solutions of Desmodur N3200 and Desmodur N3300A. Desmodur N3200 produced only precipitates while solutions of N3300A gelled. Drying those gels from SCF CO₂ yields robust, opaque-white low-density aerogels that shrink to about the same extent as the X-RF aerogels relative to their molds (~20%), they maintain a high porosity (88%) and surface area (189 m² g⁻¹), and they consist of an entangled network of nanoworms (see Figure 5) very analogous to what has been observed with vanadia and templated silicas.^{22,23} Table 2 summarizes the relevant material properties of those aerogels. Chemically, the material is polyurea (see Section 3.4a below).

Table 2. Material characterization data of polyurea aerogels derived from Desmodur N3300A.

Bulk Density ^{a,b} (ρ_b , g cm ⁻³)	Skeletal Density ^c (ρ_s , g cm ⁻³)	Porosity, Π (% void space) ^d	BET surf. Area, σ [Av. Pore Diam. ^e] (m ² g ⁻¹ [nm])	% shrinkage
0.144 ± 0.024	1.201 ± 0.005	88	189 [45.3]	20.4

a: Mold diameter = 2.0 cm. *b:* Average of 3 samples. *c:* One sample, average of 50 measurements. *d:* Porosity, $\Pi = [(1/(\rho_b) - 1/(\rho_s)) / (1/(\rho_b))] \times 100$. *e:* By the $4V_{Total}/\sigma$ method, where $V_{Total} = (1/\rho_b) - (1/\rho_s)$.

4.3 Pyrolysis of native RF, X-RF and polyurea aerogels

Figure 6 compares the thermogravimetric analysis data under inert atmosphere (N₂) of the three types of materials. Polyurea aerogels decompose almost completely

above 500 °C yielding a ~5% w/w solid residue and, obviously, mostly gaseous products. The onset of decomposition is around 300 °C. On the contrary, native RF aerogels yield a residue of about 20% of the original mass. X-RF samples behave similarly, yielding a residue of about the same mass as the native samples. However, when those findings were translated into pyrolysis of large samples at 800 °C under Ar in a tube furnace in order to produce sizable carbon aerogel monoliths, it was realized that both the macroscopic and the microscopic appearance of the resulting materials were quite different. The tiny black flakes from pyrolysis of N3300A-derived polyurea are featureless, both macroscopically and microscopically, and consist of carbon (100% w/w by EDS). The black material obtained from pyrolysis of native RF aerogels comes in monolithic form, it is quite brittle, and dull (non-reflective; Figure 7). Microscopically, it looks identical to its native RF aerogel precursor (compare Figure 8A with Figure 1A). On the contrary, the black material from pyrolysis of X-RF aerogels crosslinked with N-3300A is much sturdier, glassy with metallic luster in appearance, and macroporous microscopically (Figures 7 and 8B). The material from pyrolysis of X-RF aerogels crosslinked with N-3200 is again extremely brittle, but it has metallic luster and its pores are visible to the naked eye (Figure 8C). All C-aerogels produced from native RF and X-RF aerogels consist exclusively of carbon (100% w/w by EDS). In XRD they show a very broad reflection with maximum at the graphite angle of $2\theta = 25^\circ$ (see Supporting Information). Type IV N₂ sorption isotherms from C-aerogels derived from native RF aerogels confirm the mesoporous nature of those materials, while Type II isotherms from C-aerogels derived from X-RF aerogels are characteristic of macro- or non-porous materials (Figure 9). Material properties of all C-aerogels are summarized in Table 3. The

porosities of C-aerogels from native versus X-RF aerogels are comparable, however, their BET surface areas are very different: the mesoporous C-aerogels from native RF aerogels have surface areas in the $600 \text{ m}^2\text{g}^{-1}$ range (i.e., higher even than those of their parent RF aerogels), while the surface areas of the macroporous C-aerogels are much smaller: $17 \text{ m}^2\text{g}^{-1}$ for C-aerogels derived from X-RF-N3300A, and only $2.3 \text{ m}^2\text{g}^{-1}$ for C-aerogels derived from X-RF-N3200. Average pore diameters calculated by the $4V_{Total}/\sigma$ method agree well with the microscopic appearance of the materials. Similarly, particle size calculations show that the mesoporous material consists of nanoparticles about the same size as the parent native RF aerogels, while the elementary building blocks of the macroporous material (the term “particle” is not accurate in that case) are much larger. All C-aerogels are electrically conducting. The sheet resistance was measured with a four-point probe on flat surfaces produced by polishing larger monoliths with sand paper. Owing to their extreme fragility, that was not possible with C-aerogels from X-RF-N3200 samples. The bulk resistivity was calculated by multiplying the sheet resistance with the sample thickness and the results are cited in Table 3. Both macroporous and mesoporous C-aerogels are significantly more resistive than graphite ($1,375 \mu\Omega \text{ cm}$). This is not surprising given the large fraction of their empty space. However, while the macroporous network is ~ 360 times more resistive than graphite, the mesoporous network is $\sim 5,000$ times more so. At first approximation, the different conductivities of the two materials can be reconciled by the fact that in the mesoporous network the main contributor in the bulk resistance is the contact resistance between particles (Figure 8A), while in the macroporous network the main contributor is the resistance of the skeletal filaments (Figure 8B). This model, however, is refined further in Section 3.4.B below.

Table 3. Characterization of carbon aerogels derived from native RF and X-RF aerogels.

C-aerogel derived by pyrolysis of:	Bulk Density ^a (ρ_b , g cm ⁻³)	Skeletal Density ^b (ρ_s , g cm ⁻³)	Porosity, Π (% void space)	BET surf. Area, σ [Av. Pore Diam. ^c] (m ² g ⁻¹ [nm])	Particle Diameter (nm)	Bulk Resistivity ($\mu\Omega$ cm)
Native RF aerogel	0.138 \pm 0.024	2.146 \pm 0.121	93	626 [43]	4.47	6.8 \times 10 ⁶
X-RF-N3200 aerogel	0.218 \pm 0.090	1.814 \pm 0.022	88	2.3 [7018]	[1438] ^d	e
X-RF-N3300A aerogel	0.254 \pm 0.082	1.866 \pm 0.011	86	17 [800]	[189] ^d	5.0 \times 10 ⁵

a: Average of 3 samples. b: One sample, average of 50 measurements. c: Average pore diameter = $4V_{Total}/\sigma$, where $V_{Total}=(1/\rho_b)-(1/\rho_s)$. d: In those cases, “particle” should be rather taken to mean “elementary building block.” Numbers in brackets are given for comparative purposes only, because the macroporous aerogel networks do not consist of particles. e: Owing to extreme fragility of those materials, it was not possible to fabricate rectangular blocks for electrical measurements.

4.4 Chemical, physical and morphological evolution of RF, X-RF and polyurea aerogels upon heat treatment.

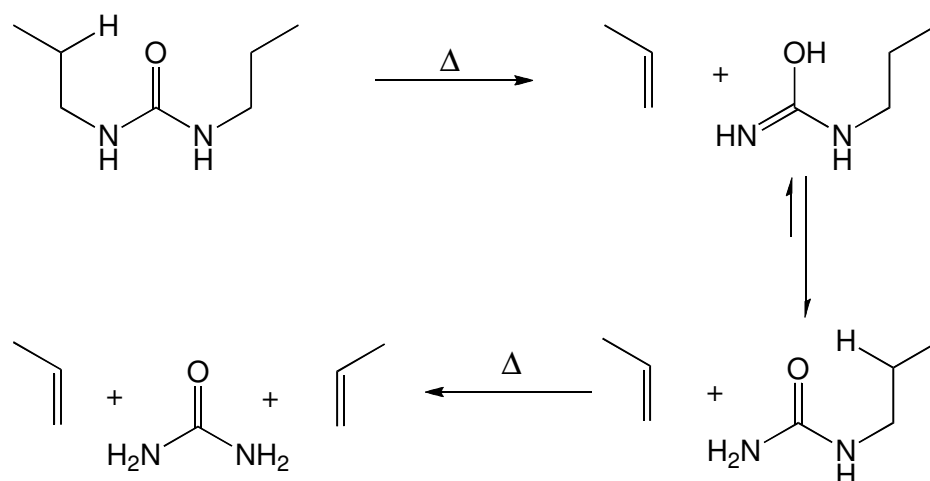
The different morphology of C-aerogels resulting from pyrolysis of X-RF versus native RF aerogels is intriguing. Skeletal densities (Table 3) for the two types of aerogels are different, but all values are in the graphitic (2.267 g cm^{-3})/carbon black ($1.8\text{-}2.1 \text{ g cm}^{-3}$) range indicating that the elementary building blocks in both kinds of materials are rather compact. Gases produced by decomposition of the crosslinker may account for the macropores. However, that mechanism alone would not account for the apparent lack of mesoporosity from the macroporous samples: gas evolution would account for the macropores but the surrounding walls should remain mesoporous. In order to investigate the mechanism that produces macropores, it was decided to follow the physical, chemical and morphological evolution of native RF, X-RF and polyurea aerogels upon heat treatment in the $200\text{-}300 \text{ }^\circ\text{C}$ temperature range that precedes and overlaps with the onset of the decomposition of the crosslinker (Figure 6).

4.4.1 Physical and chemical characterization after heat treatment at different temperatures

By DSC (Figure 10) N3300A-derived polyurea melts at $123 \text{ }^\circ\text{C}$ and starts decomposing above $280 \text{ }^\circ\text{C}$, in agreement with TGA (Figure 6). Indeed, ^{13}C -NMR (Figure 11) shows no chemical change between freshly made samples and samples treated up to $250 \text{ }^\circ\text{C}$ for 3 h under Ar. However, upon similar treatment at $300 \text{ }^\circ\text{C}$, polyurea loses the urea carbonyl, presumably through a γ -hydrogen abstraction from both sides of the carbonyl in the mass-spectrometric McLafferty rearrangement fashion

or a Norrish Type II photochemical cleavage.^{24,25,26} In that regard, the broad resonances in the 120-130 ppm range are assigned to terminal olefins produced by that decomposition pathway. The isocyanurate ring is heat-stable up to 300 °C

Scheme 3. First decomposition pathway of polyurea aerogels



By DSC, RF and X-RF aerogels (both with N3200 and N3300A) do not show evidence of melting. Instead, X-RF samples show signs of decomposition earlier than polyurea itself. Both N3200 and N3300A crosslinked samples start evolving heat at ~230 °C. ¹³C-NMR shows that the RF skeletal framework is stable all the way up to 300 °C (compare Figures 12A and 12B). However, by 250 °C X-RF samples crosslinked with N3300A (in the presence of TEA as catalyst) have lost the strong 156 ppm resonance (compare Figures 12C and 12D), which has been assigned to carbamate carbonyls with phenolic hydroxyls (see section 3.1 above), and most importantly, the relative intensity of the peaks at 118/128 ppm has been restored back near to its native RF value. Meanwhile

the crosslinker is still intact and within the sample as concluded by the low intensity urea carbonyl peak at 159 ppm and the relative intensity of the high field feature (compare Figures 12C and 12D). Those data taken together suggest that the first step in the decomposition of the X-RF samples is at least a loss of the chemical bonding between the crosslinker and the RF backbone.

4.4.2 Morphological characterization after heat treatment at different temperatures

Figure 13 presents the microscopic evolution (by SEM) of the three types of samples (native RF, X-RF and polyurea) upon heat treatment at 200 °C, 250 °C and 300 °C, and Table 4 summarizes the pertinent data. First, no significant morphological change is observed in the native RF samples in agreement with ¹³C-NMR (Figure 12). In all three temperatures, samples retain their nanoparticulate structure, although in general the secondary particles should be coming closer together, as reflected on both the porosity and the surface area, which have been both steadily reduced (compare Tables 1 and 4). On the other hand, Desmodur N3300A derived polyurea has already melted at 200 °C, loosing its nanoworm-like morphology. Macroporous voids appear as early as 200 °C, and by 250 °C polyurea samples closely resemble those of C-aerogels obtained after pyrolysis of X-RF-N3300A aerogels at 800 °C. By 300 °C polyurea aerogels have collapsed completely to the same featureless solid observed after pyrolysis at 800 °C. Since by TGA and ¹³C-NMR no significant decomposition, and therefore no significant gas evolution has taken place off polyurea samples at 250 °C, we conclude that the macropores are caused by the surface tension forces developing during melting. Now,

from that perspective, none of the X-RF samples melts (by DSC, Figure 10) or changes its appearance otherwise after heat-treatment up to 200 °C. At 250 °C, X-RF-N3200 samples have melted, while X-RF-N3300A samples remain intact. By 300 °C, both kinds of X-RF samples have melted, acquiring macroporous morphologies similar to those of their terminal C-aerogels after pyrolysis at 800 °C. (Nevertheless, it is pointed out that none of the samples pyrolyzed up to 300 °C is electrically conducting. Electrical conductivity appears upon pyrolysis above 600 °C.)

From the above, decomposition and gas evolution are not the main factors that create the macropores. The melt-and-flow model seems to explain adequately the macroporosity in C-aerogels from X-RF aerogels. However, that model is only a first approximation. For example, if we consider the thermal stability of native silica versus native RF aerogels, we realize that while the skeletal frameworks of both materials are stable up to 300 °C, nevertheless, X-RF aerogels crosslinked with N3200 show complete melting at 250 °C (Figure 13) in contrast to silica aerogels also crosslinked with Desmodur N3200 that do not show any signs of melting up to 300 °C (see Supporting Information). Therefore, the different behavior of the two crosslinked materials (silica and RF) has to be attributed to the chemical interaction of the crosslinker with the skeletal framework. The crosslinker is covalently bonded to the skeletal framework, and in essence the assembly comprises a new chemical entity with its own physical and chemical properties. Consistently with the DSC and ¹³C-NMR data, it seems that as the temperature increases the urethane bridges between RF and the crosslinker break first. The released polymer finds itself above its melting point, wetting and causing collapse of the surrounding framework. Indeed, cross-sections of the X-RF-N3200 framework after

heat-treatment at 300 °C (Figure 14.A, Inset) show nanoparticles squeezed close together into a xerogel-like structure covered with a smooth skin from the melted crosslinker.

Table 4. Pertinent materials characterization data of various samples after heat-treatment under Ar at three different temperatures as indicated.

Aerogel Type [heat-treated at]	Bulk Density ^a (ρ_b , g cm ⁻³)	Skeletal Density ^b (ρ_s , g cm ⁻³)	Porosity, P (% void space) ^c	BET surf. Area, σ [Av.Pore Diam. ^d] (m ² g ⁻¹ [nm])
Native RF [200 °C]	0.146	1.379 ± 0.022	89	319 [19.8;76.8]
Native RF [250 °C]	0.125	1.404 ± 0.029	91	259 [31.6;112]
Native RF [300 °C]	0.127	1.387 ± 0.014	91	255 [33.4;112]
Polyurea [200 °C]	0.249	0.813 ± 0.011	69	e
Polyurea [250 °C]	0.229	0.743 ± 0.007	69	e
Polyurea [300 °C]	0.285	0.846 ± 0.024	66	e
X-RF-N3200 [200 °C]	0.610	1.267 ± 0.006	52	87.2 [26.5;39.0]
X-RF-N3200 [250 °C]	0.656	1.059 ± 0.007	38	3.56 [26.9.652]
X-RF-N3200 [300 °C]	0.385	1.109 ± 0.004	65	e
X-RF-N3300 [200 °C]	0.336	1.276 ± 0.006	74	171 [36.5;51.3]
X-RF-N3300 [250 °C]	0.422	1.256 ± 0.016	66	16.1 [22.4;391]
X-RF-N3300 [300 °C]	0.397	1.094 ± 0.040	64	14.3 [32;449]

a: Irregularly-shaped samples; by the mercury displacement method. b: One sample, average of 50 measurements. c: Porosity, $\Pi = [(1/\rho_b) - 1/(\rho_s)]/(\rho_b) \times 100$. d: By the $4V_{Total}/\sigma$ method, where V_{Total} has been calculated by two methods, hence the two numbers cited for the Average Pore Diameter: first automatically by the system software from a single point volume measurement of the N₂ adsorbed, and second manually from the bulk and skeletal densities via $V_{Total} = (1/\rho_b) - (1/\rho_s)$. e: Isotherms show negative slopes and could not be used for surface area analysis.

The same morphology is retained within the walls surrounding the macropores after pyrolysis of X-RF-N3300A aerogels at 800 °C (Figure 14.B, Inset) The xerogel-like internal texture of the macroporous walls of C-aerogels is consistent with the lower skeletal densities of those materials relative to the skeletal densities of C-aerogels from native RF. Furthermore, the better contact between carbon particles squeezed together in a xerogel-like fashion also explains the lower resistivity of our macroporous variety of C-aerogels.

4.5 Electrochemical evaluation of C-aerogels made from X-RF aerogels

It is well-established from work in monolithic separation media that mass transfer in macropores has both convective and diffusional components, while only diffusion prevails in mesopores.²⁷ That, coupled with the fact that our macroporous carbon aerogels are more electrically conducting than typical mesoporous C-aerogels, suggests that sturdy macroporous C-aerogels may be useful as gas diffusion electrodes in fuel cells. In that regard, the actual performance of macroporous C-aerogels as electrode materials was evaluated electrochemically. Figure 15 compares the cyclic voltammograms of ferrocene on a monolithic macroporous C-aerogel electrode made from X-RF-N3300A versus on a typical Pt disk electrode. The large pre-wave background current, $i_{background}$, in the C-aerogel electrode is due to charging of the double layer, and based on the relationship $i_{background} = \nu C_d$ (ν is the potential sweep rate, set equal to 0.1 Vs⁻¹) we calculate the double layer capacity, C_d .²⁸ Assuming a typical value for the specific electrical double layer capacity of 20 $\mu\text{F cm}^{-2}$, it is calculated that the electrode area is in the order to 1.25 $\text{m}^2 \text{g}^{-1}$. This figure is lower than the BET surface area reported in Table 3 for the same material (17 $\text{m}^2 \text{g}^{-1}$) and the difference is taken as evidence that the electrolytic solution

does not reach all surfaces accessible for N₂ physisorption, or equivalently, only a fraction of the BET surface area is accessible for redox chemistry. A second observation is that the potential peak-to-peak separation, E_{p-p} , is much larger with the C-aerogel electrode (390 mV) than what it is with Pt (100 mV) and that is attributed directly to the higher ohmic resistance of the carbon electrode. Owing to their fragility, it was difficult to conduct similar experiments with C-aerogels derived from either native RF or X-RF-N3200 aerogels.

Macroporous C-aerogels from X-RF-N3300A were finally used as substrates for the electrochemical deposition of Pt, which is used as catalyst in fuel cell electrodes. The electrocatalytic activity of those materials will be reported elsewhere. Figure 16.A shows a low-resolution SEM after Pt electrodeposition, and Figure 16.B shows the EDS-generated Pt map on the same spot. The charge consumed for electrodeposition of Pt was 85.6 mC, corresponding to 4.44×10^{-4} mmol of Pt. The piece of C-aerogel used as an electrode weighed 0.046 g, and by considering the BET surface area from Table 3 ($17 \text{ m}^2 \text{ g}^{-1}$), it is calculated that the specific electrode had a total internal surface area (both accessible and inaccessible electrochemically) of 0.782 m^2 . Therefore, the Pt coverage was $5.67 \times 10^{-11} \text{ mol cm}^{-2}$, which corresponds to 57% of a monolayer coverage (assuming $1.0 \times 10^{-10} \text{ mol cm}^{-2}$ for a single monolayer coverage with a small molecule). However, as it can be seen on the Pt map, the metal has been deposited non-uniformly, in islands.

5. CONCLUSIONS

Polymer crosslinked RF aerogels are sturdier and lower density materials than their corresponding native RF precursors, and therefore they may be pursued on their

own right for typical aerogel applications in thermal and acoustic insulation. Pyrolysis of those materials, however, creates a new class of macroporous carbon aerogels, without need for using templating agents. The new materials have been evaluated electrochemically and applications as fuel cell electrodes are clearly visible. Along the way we have stumbled across some quite interesting low-density polyurea aerogels, that are evaluated thermally and mechanically.

6. ACKNOWLEDGEMENTS

We acknowledge the University of Missouri Research Board (N.L.) and the NSF under CMMI-0653919 for financial support. We also thank Dr. Wei Wycoff for her assistance with solids NMR and Professor Douglas K. Ludlow for his assistance with N₂ sorption porosimetry.

7. REFERENCES

1. (a) Pekala, R. W. *J. Mater. Science* **1989**, *24*, 3221-3227. (b) Pekala, R. W.; Alviso, C. T.; Kong, F. M.; Hulsey, S. S. *J. Non-Cryst. Solids* **1992**, *145*, 90-98. (c) Yamamoto, T.; Nishimura, T.; Suzuki, T.; Tamon, H. *J. Non-Cryst. Solids* **2001**, *288*, 46-55. (d) Li, Wen-Cui; Lu, An-Hui; Schueth, F. *Chem. Mater.* **2005**, *17*, 3620-3626.
2. Al-Muhtaseb, S A.; Ritter, J. A. *Adv. Mater.* **2003**, *15*, 101-114.
3. Yamamoto, T.; Sugimoto, T.; Suzuki, T.; Mukai, S. R.; Tamon, H. *Carbon* **2002**, *40*, 1345-1351.
4. (a) Pekala, R. W.; Farmer, J. C.; Alviso, C. T.; Tran, T. D.; Mayer, S. T.; Miller, J. M.; Dunn, B. *J. Non-Cryst. Solids* **1998**, *225*, 74-80. (b) Jurewicz, K.; Frackowiak, E.; Beguin, F. *J. Power Sources* **2001**, *96*, 270.
5. Kabbour, H.; Baumann, T. F.; Satcher, J. H., Jr.; Saulnier, A.; Ahn, C. C. *Chem. Mater.* **2006**, *18*, 6085-6087.
6. Merzbacher, C. I.; Meier, S. R.; Pierce, J. R.; Korwin, M. L. *J. Non-Cryst. Solids* **2001**, *285*, 210-215.
7. Chan, K.; Ding, J.; Cheng, S.; Tsang, K. *J. Mater. Chem.* **2004**, *14*, 505-516.
8. (a) Biesmans, G.; Mertens, A.; Duffours, L.; Woignier, T.; Phalippou, J. *J. Non-Cryst. Solids* **1998**, *225*, 64-68. (b) Sakintuna, B.; Yueruem, Y. *Industrial & Engineering Chemistry Research* **2005**, *44*, 2893-2902.
9. Liu, R.; Shi, Y.; Wan, Y.; Meng, Y.; Zhang, F.; Gu, D.; Chen, Z.; Tu, B.; Zhao, D. *J. Am. Chem. Soc.* **2006**, *128*, 11652-11662.
10. Baumann, T. F.; Satcher, J. H. *J. Non-Cryst. Solids* **2004**, *350*, 120-125.

11. Perpall, M. W.; Perera, K. P. U.; DiMaio, J.; Ballato, J.; Foulger, S. H.; Smith, D. W. J.; *Langmuir* **2003**, *19*, 7151-7156.
12. Gierszal, K. P.; Jaroniec, M. *J. Am. Chem. Soc.* **2006**, *128*, 10026-10027.
13. Tanaka, S.; Katayama, Y.; Tate, M. P.; Hillhouse, H. W.; Miyake, Y. *J. Mater. Chem.* **2007**, *17*, 3639-3645.
14. (a) Leventis, N.; Sotiriou-Leventis, C.; Zhang, G.; Rawashdeh, A.-M. M. *NanoLetters* **2002**, *2*, 957-960. (b) Zhang, G.; Dass, A.; Rawashdeh, A.-M. M.; Thomas, J.; Council, J. A.; Sotiriou-Leventis, C.; Fabrizio, E. F.; Ilhan, F.; Vassilaras, P.; Scheiman, D. A.; McCorkle, L.; Palczer, A.; Johnston, J. C.; Meador, M. A. B.; Leventis, N. *J. Non-Cryst. Solids*, **2004**, *350*, 152-164.
15. (a) Leventis, N.; Gao, X. *J. Electroanal. Chem.* **2001**, *500*, 78-94. (b) Leventis, N.; Oh, W. S.; Gao, X.; Rawashdeh, A.-M. M. *Anal. Chem.* **2003**, *75*, 4996-5005.
16. Mulik, S.; Sotiriou-Leventis, C.; Leventis, N. *Chem. Mater.* **2007**, *19*, 25, 6138-6144.
17. (a) Leventis, N. *Acc. Chem. Res.* **2007**, *40*, 874-884. (b) Katti, A.; Shimpi, N.; Roy, S.; Lu, H.; Fabrizio, E. F.; Dass, A.; Capadona, L. A.; Leventis, N. *Chem. Mater.* **2006**, *18*, 285-296. (c) Leventis, N.; Sotiriou-Leventis, C.; Mulik, S.; Dass, A.; Schnobrich, J.; Hobbs, A.; Fabrizio, E. F.; Luo, H.; Churu, G.; Zhang, Y.; Lu, H. *J. Mater. Chem.* **2008**, *18*, 2475-2482. (d) Leventis, N.; Vassilaras, P.; Fabrizio, E.; Dass, A. *J. Mater. Chem.* **2007**, *17*, 1502-1508.
18. Brunauer, S.; Emmett, P. H.; Teller, E. *J. Am. Chem. Soc.* **1938**, *60*, 309.
19. Hüsing, N.; Schubert, U.; Mezei, R.; Fratzl, P.; Riegel, B.; Kiefer, W.; Kohler, D.; Mader, W. *Chem. Mater.* **1999**, *11*, 451-457.

20. Fricke, J.; Reichenauer, G. *J. Non-Cryst. Solids* **1987**, 95-96, 1135-1142.
21. Albrecht, M.; Zauner, J.; Fröhlich, R.; Kataeva, O.; Wegejius, E.; Rissanen, K. *Synthesis* **2002**, 10, 1434-1444.
22. Leventis, N.; Sotiriou-Leventis, C.; Mulik, S.; Dass, A.; Schnobrich, J.; Hobbs, A.; Fabrizio, E. F.; Luo, H.; Churu, G.; Zhang, Y.; Lu, H. *J. Mater. Chem.* **2008**, 18, 2475-2482.
23. (a) Leventis, N.; Mulik, S.; Wang, X.; Dass, A.; Patil, V. U.; Sotiriou-Leventis, C.; Lu, H.; Churu, G.; Capecelatro, A. *J. Non-Cryst. Solids* **2008**, 354, 632-644.
(b) Leventis, N.; Mulik, S.; Wang, X.; Dass, A.; Sotiriou-Leventis, C.; Lu, H. *J. Am. Chem. Soc.* **2007**, 129, 10660-10661.
24. Silverstein, R. M.; Bassler, G. C.; Morrill, T. C. *Spectroscopic Identification of Organic Compounds*, 5th ed., John Wiley & Sons, Inc., New York, N.Y., 1991, Chapter 2.
25. Barltrop, J. A.; Coyle, J. D. *Principles of Photochemistry*, John Wiley and Sons, Inc., New York, N.Y., 1978, Chapter 6.
26. Durairaj, B.; Dimock, A. W.; Samulski, E. T. *J. Polym. Sci.: Part A: Polym. Chem.* **1989**, 27, 3211-3225.
27. Svec, F.; Huber, C. G. *Anal. Chem.* **2006**, 78, 2101-2107.
28. Bard, A. J.; Faulkner, L. J. *Electrochemical Methods, Fundamentals and Applications*, 2nd ed.; Wiley: New York, **2000**.

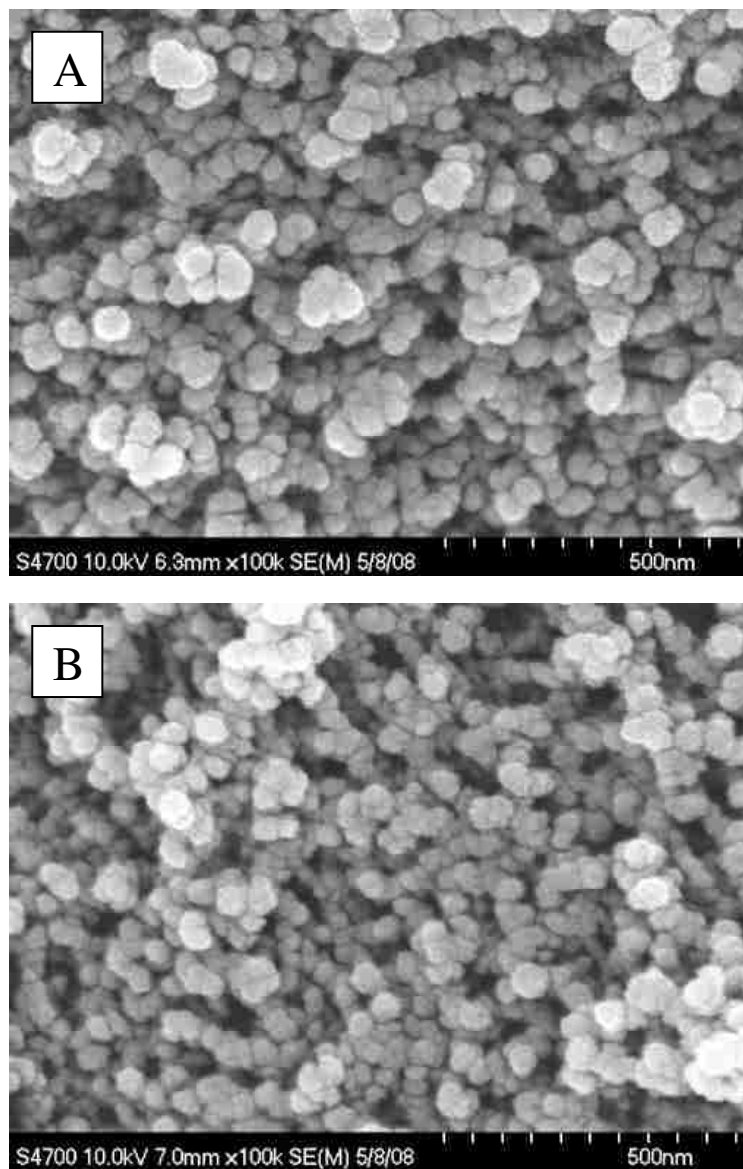
8. FIGURES

Figure 1. Scanning Electron Microscopy (SEM) of a native RF aerogel (A), and of a Desmodour N3300A tri-isocyanate crosslinked (X-RF) aerogel (B), prepared according to Scheme 1.

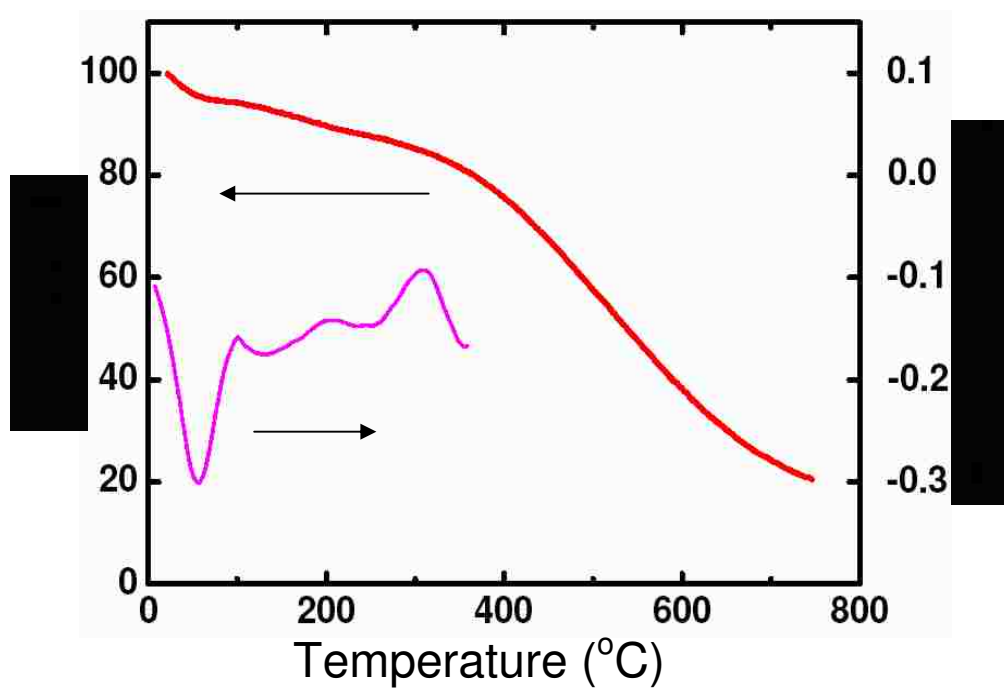


Figure 2. Thermogravimetric Analysis (TGA) and Differential Scanning Calorimetry (DSC) both under N_2 of native RF aerogels. (Heating rate: $10\text{ }^\circ\text{C}/\text{min}$).

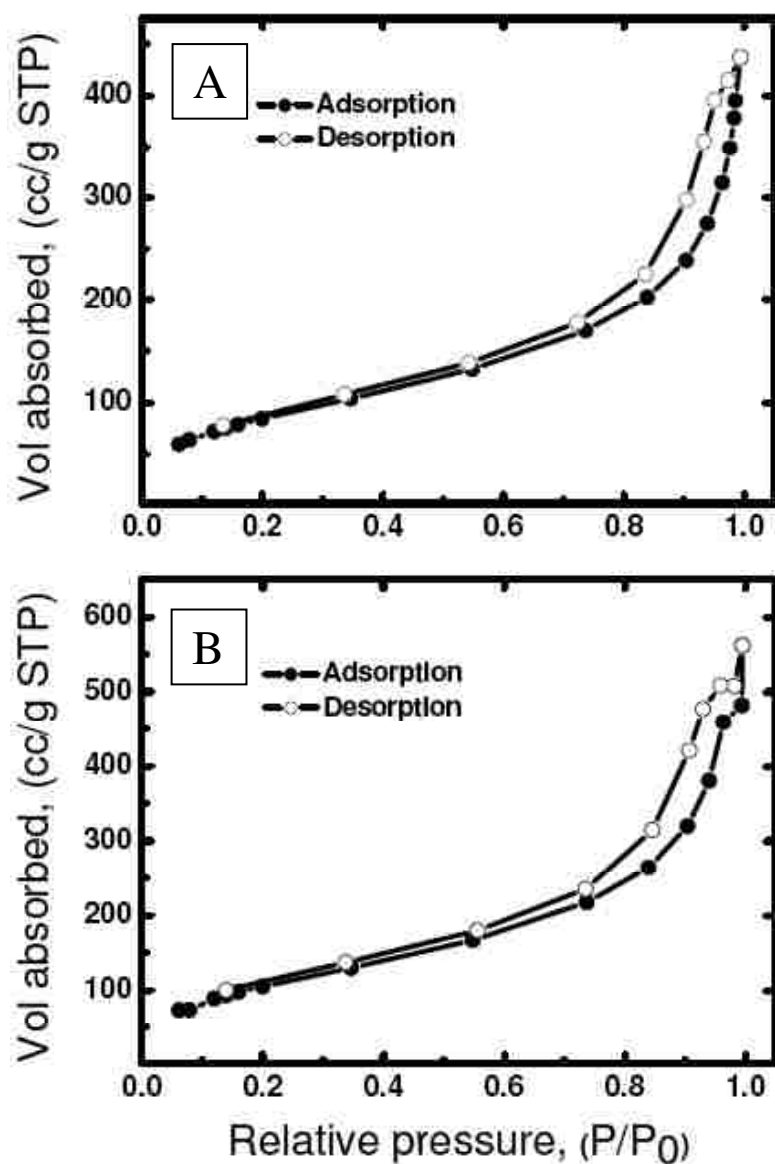


Figure 3. Nitrogen sorption porosimetry. (A) Adsorption-desorption isotherms for a native RF aerogel ($\rho_b = 0.136 \pm 0.008 \text{ g cm}^{-3}$; BET surface area = $318 \text{ m}^2 \text{ g}^{-1}$). (B) Adsorption-desorption isotherms for a X-RF aerogel crosslinked with Desmodur N3300A in the presence of TEA ($\rho_b = 0.120 \pm 0.005 \text{ g cm}^{-3}$; BET surface area = $396 \text{ m}^2 \text{ g}^{-1}$).

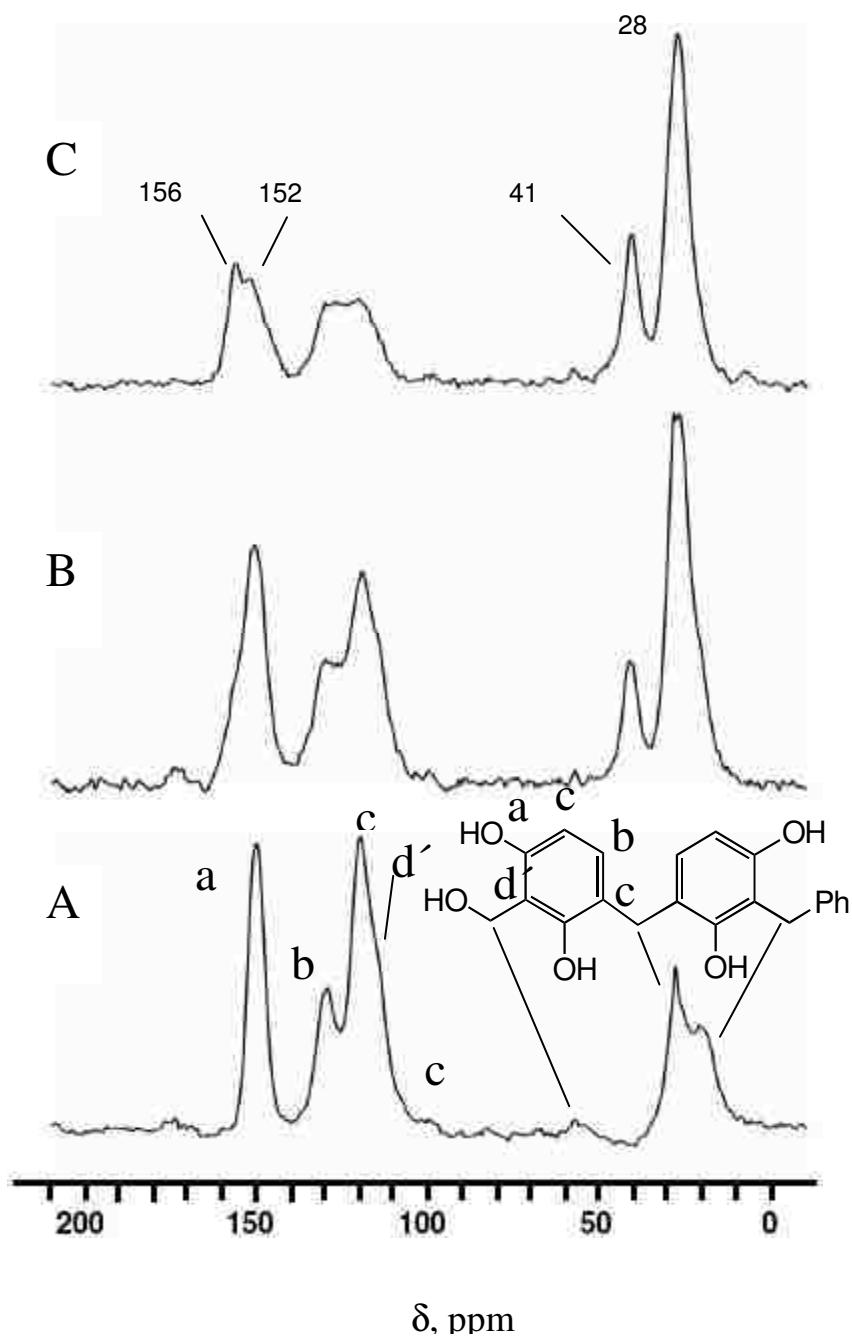


Figure 4. Solid ^{13}C CPMAS NMR of acid-catalyzed native RF aerogel (A), a X-RF aerogel sample crosslinked with Desmodur N3300A without catalyst (B) and a X-RF aerogel sample crosslinked with Desmodur N3300A in the presence of TEA (C). (For pertinent materials characterization data refer to Table 1.)

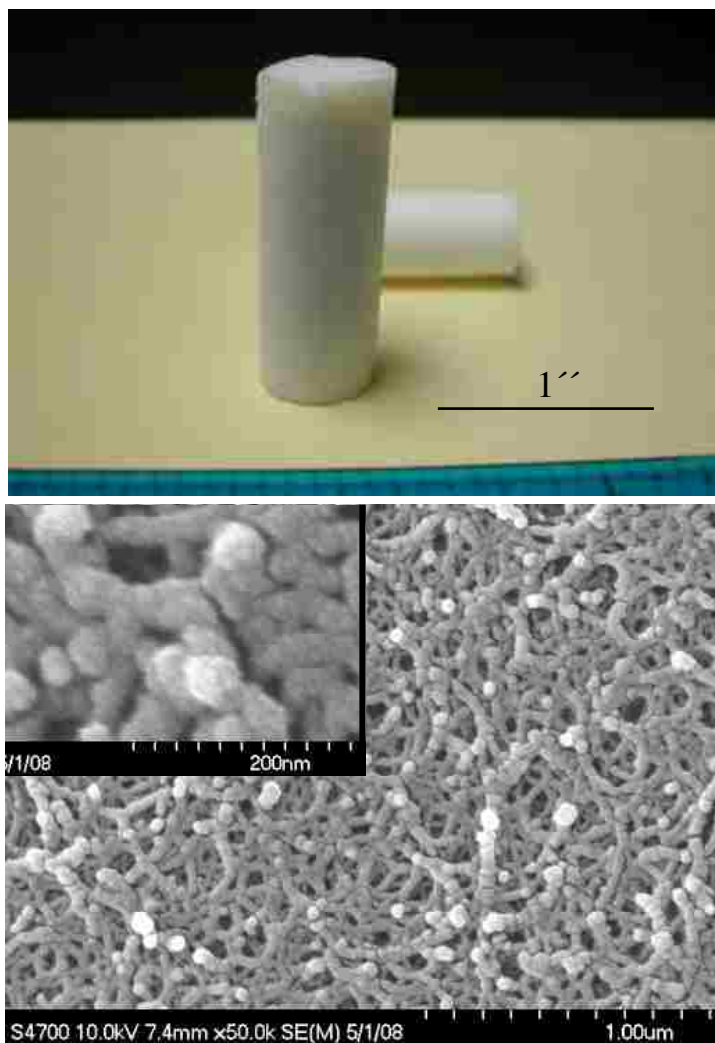


Figure 5. Photograph (A) and SEM (B) of a polyurea aerogel sample prepared by gelation of Desmodur N3300A in acetone/water in the presence of TEA.

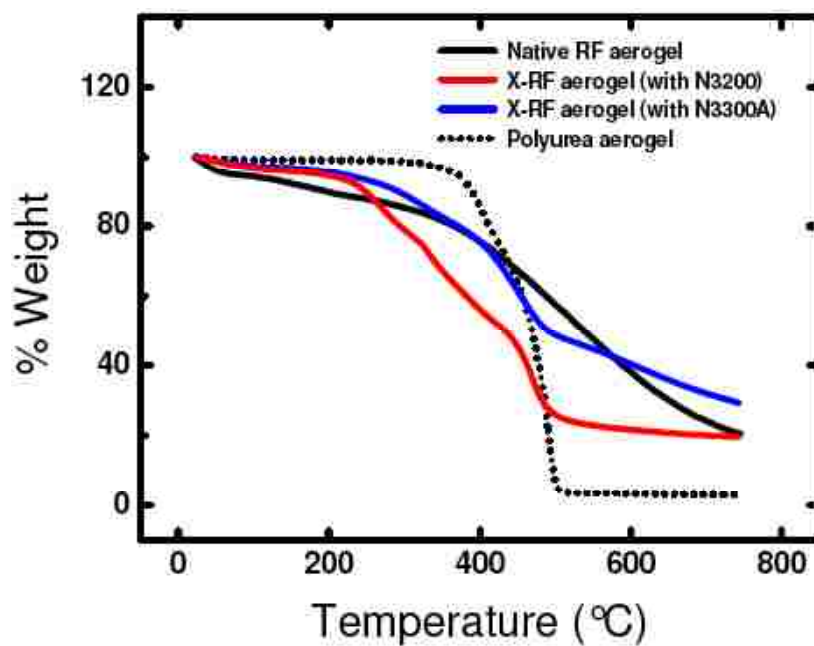


Figure 6. Thermogravimetric analysis under N_2 of a native RF, two X-RF samples, one crosslinked with Desmodur N3200 di-isocyanate and one with Desmodur N3300A tri-isocyanate, and a polyurea aerogel, as indicated. (Heating rate: $10\text{ }^\circ\text{C min}^{-1}$.)



Figure 7. Photographs of carbon aerogels prepared by pyrolysis at 800 °C under Ar of native RF aerogels and of X-RF aerogels prepared using Desmodur N3300A triisocyanate and TEA.

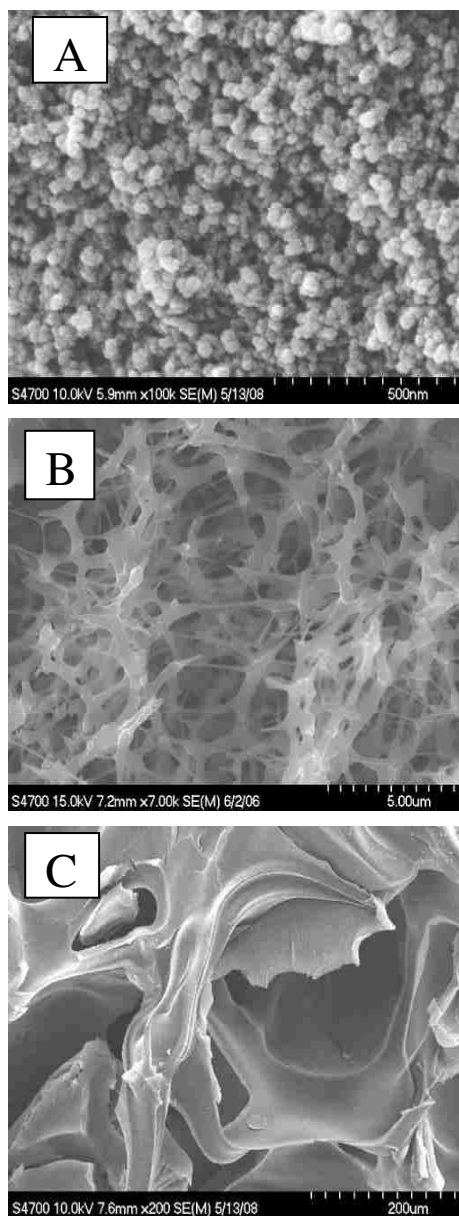


Figure 8. SEM of carbon aerogels made by pyrolysis of native RF aerogels (A), X-RF aerogels crosslinked with Desmodur N3300A tri-isocyanate (B) and X-RF aerogels crosslinked with Desmodur N3200 di-isocyanate (C). (Notice the different magnifications and length scales.)

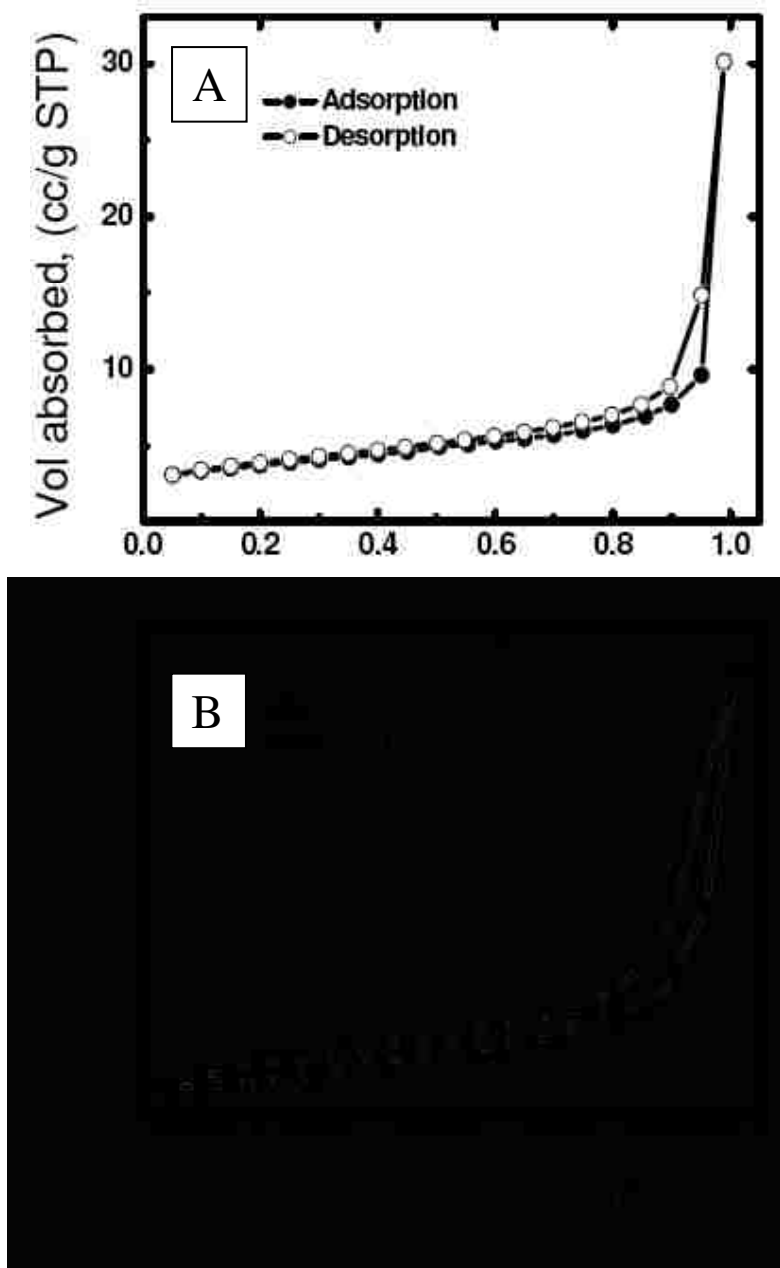


Figure 9. Nitrogen sorption porosimetry. (A) Adsorption-desorption isotherms for a C-aerogel made from a native RF aerogel ($\rho_b = 0.138 \pm 0.024 \text{ g cm}^{-3}$; BET surface area = $626 \text{ m}^2 \text{ g}^{-1}$). (B) Adsorption-desorption isotherms for a C-aerogel prepared from a X-RF aerogel crosslinked with Desmodur N3300A in the presence of TEA ($\rho_b = 0.254 \pm 0.082 \text{ g cm}^{-3}$; BET surface area = $17 \text{ m}^2 \text{ g}^{-1}$).

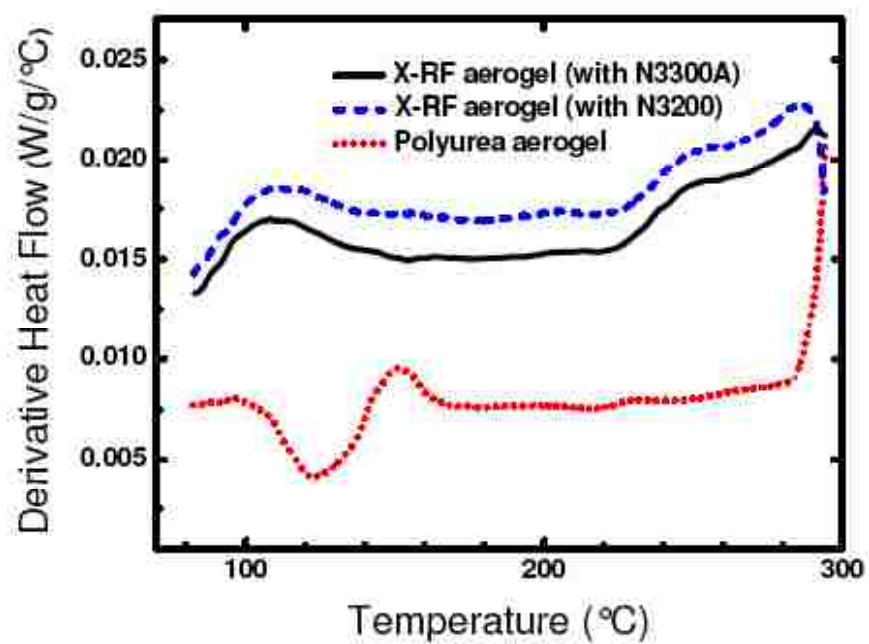


Figure 10. Differential Scanning Calorimetry (DSC) under N_2 at $10\text{ }^\circ\text{C min}^{-1}$ of two X-RF samples, one crosslinked with Desmodur N3200 di-isocyanate and one with Desmodur N3300A tri-isocyanate, and a polyurea aerogel, as indicated.

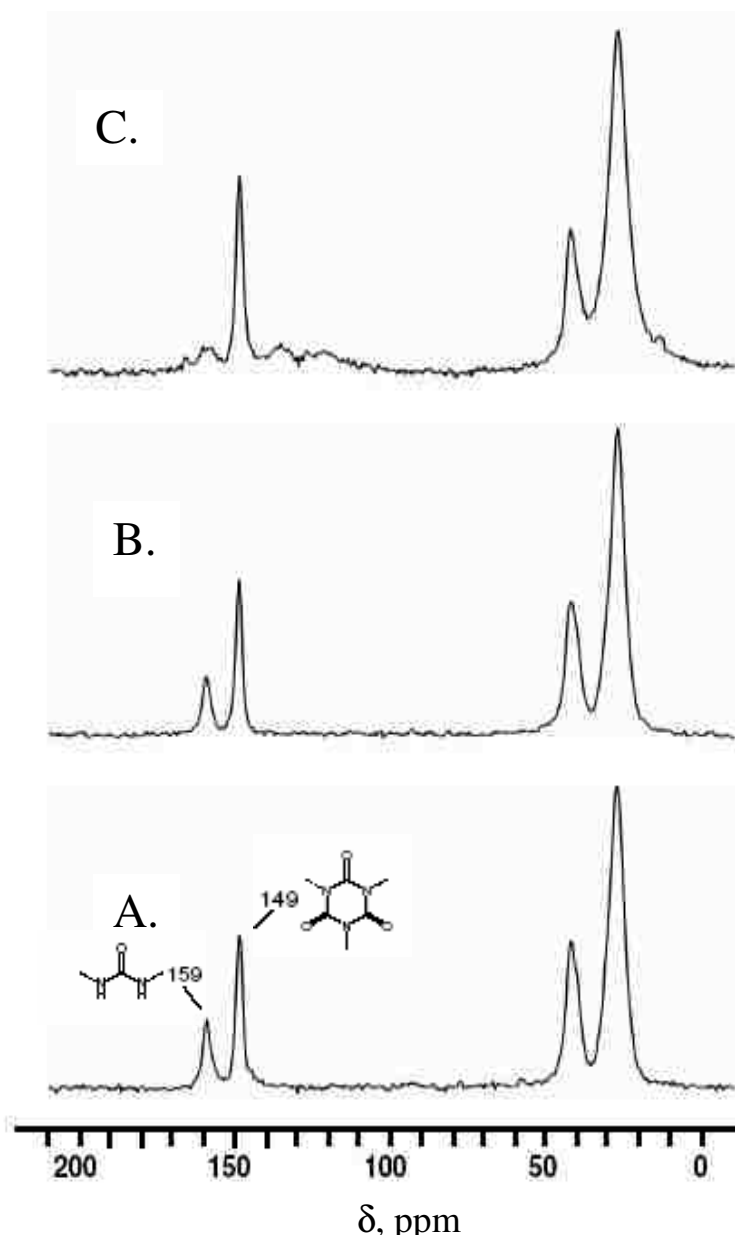


Figure 11. Solid ^{13}C CPMAS NMR of polyurea aerogels: as-made (A), after heating under Ar for 3 h at 250 °C (B) and at 300 °C (C). (For pertinent materials characterization data refer to Table 4.)

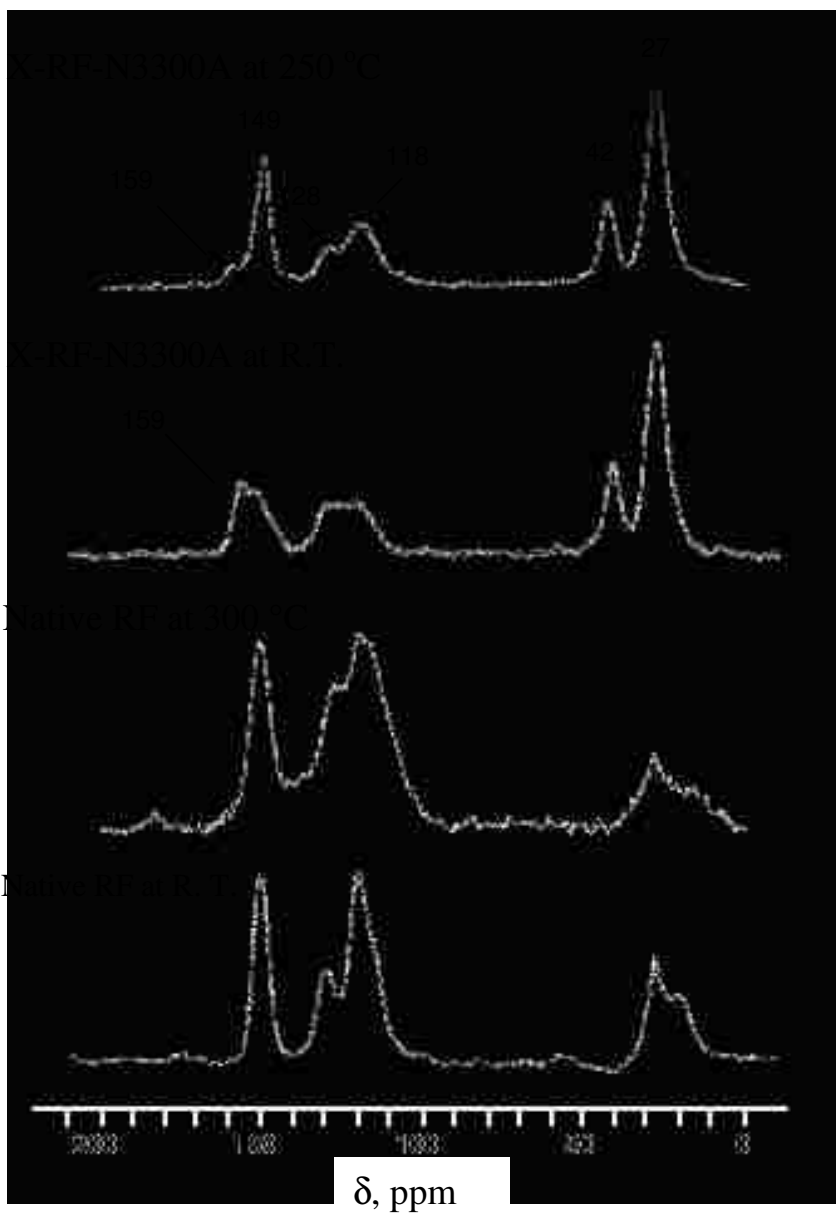


Figure 12. Solid ^{13}C CPMAS NMR of native RF and X-RF-N3300A aerogels as indicated. The crosslinked sample after heat treatment at 250 °C without losing the crosslinker (the high-field features maintain the same relative intensity) it recovers features of the native RF aerogel, which is interpreted that the chemical bonding of the crosslinker with the polymer has been broken.

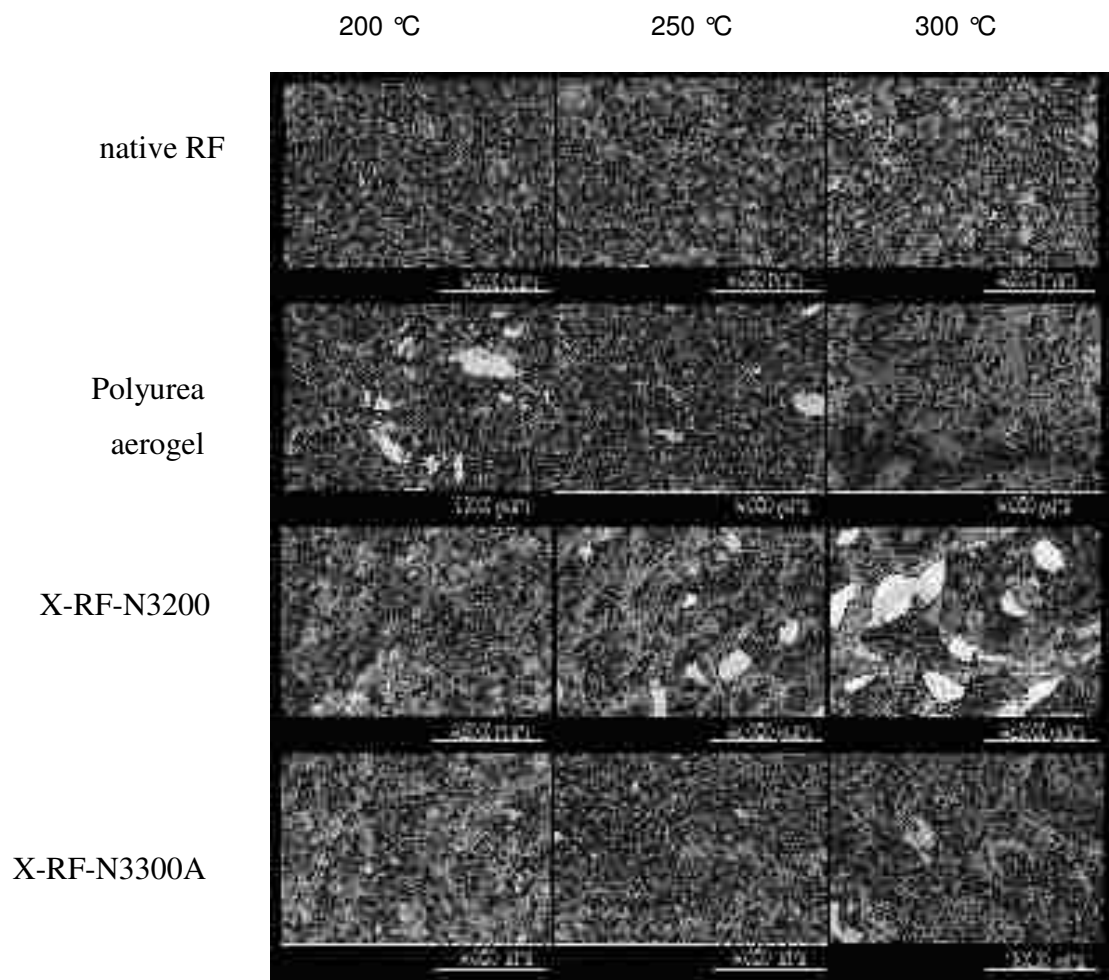


Figure 13. SEM of four types of aerogels, heat-treated under Ar for 3 h at three different temperatures, as indicated. (Notice the different magnifications and length scales. For pertinent materials characterization data refer to Table 4.)

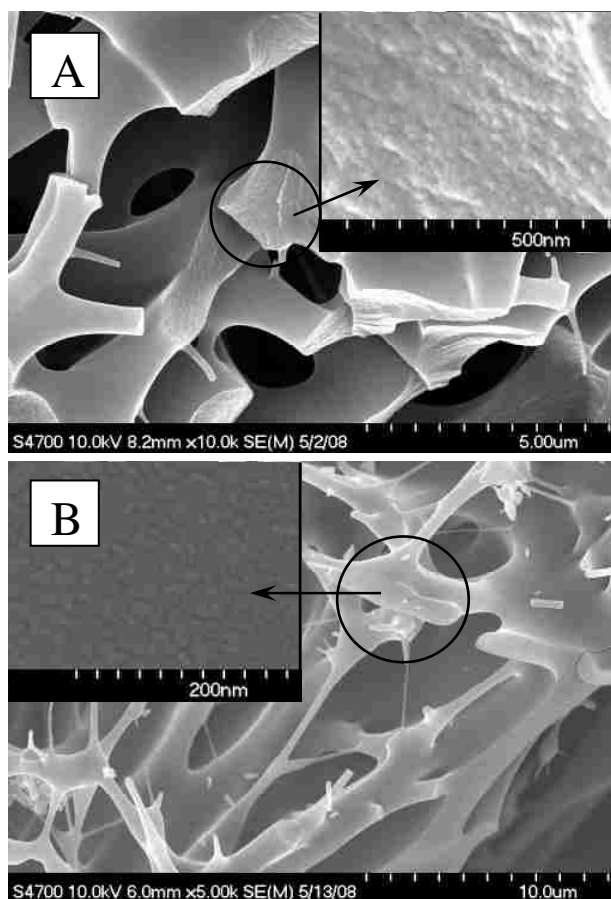


Figure 14. Looking inside the skeletal framework: (A) Survey SEM and SEM at the fracture (see inset) on the skeletal framework of an X-RF sample crosslinked with Desmodur N3200 (X-RF-N3200) and heat-treated under Ar at 300 °C (compare with Figure A and notice the xerogel-like appearance inside the skeletal framework underneath the skin of molten crosslinker). (B) Survey SEM and SEM at the fracture (see inset) on the skeletal framework of a C-aerogel prepared by pyrolysis under Ar at 800 °C of a X-RF-N3300A aerogel. (Notice again the xerogel-like appearance inside the skeletal framework of the macroporous C-aerogel.)

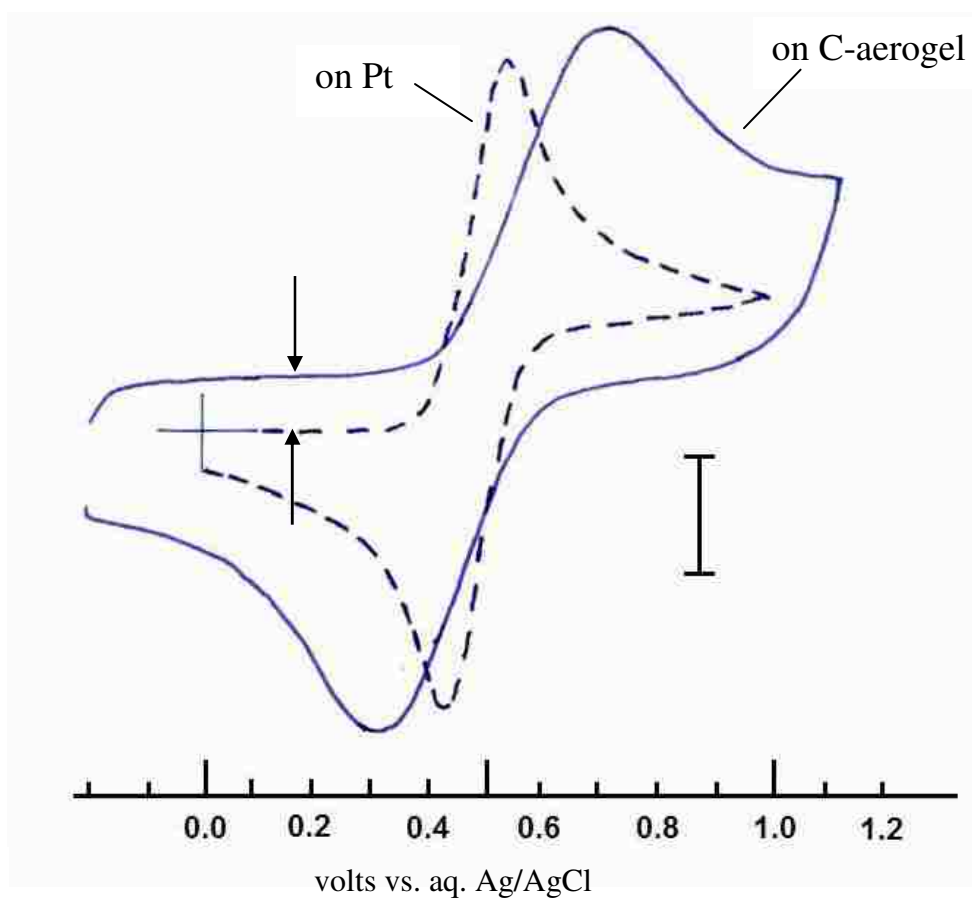


Figure 15. Cyclic voltammetry of ferrocene (3 mM) in $\text{CH}_3\text{CN}/0.1 \text{ M TBAP}$ at 0.1 V s^{-1} , using a Pt disc electrode (1 mm in diameter), or a C-aerogel electrode (0.008 g) made from a X-RF-N3300A aerogel, as indicated. Current scale: bar length 0.02 mA for Pt and 0.4 mA for the C-aerogel. (The C-aerogel surface area accessible by the electrolytic solution is calculated from the pre-wave charging current, shown with arrows.)

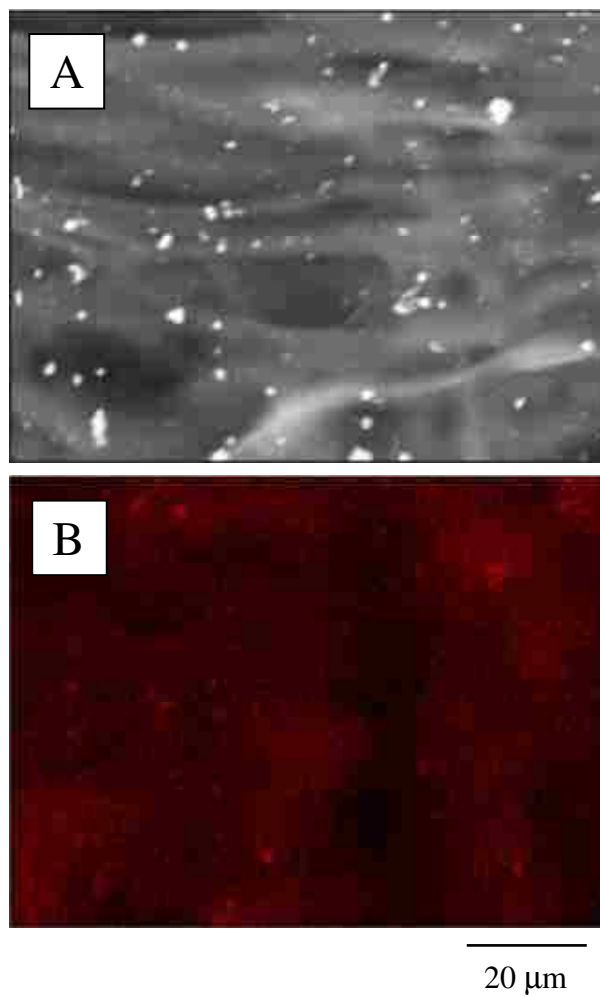


Figure 16. (A) SEM of a carbon aerogel prepared by pyrolysis of a X-RF-N3300A aerogel after electrodeposition of Pt from a 3 mM solution of K_2PtCl_4 in $\text{CH}_3\text{CN}/0.1$ M TBAP containing enough water to solubilize the salt. (B) Energy Dispersive Spectra (EDS)-derived Pt map at the same location.

9. SUPPORTING INFORMATION

FTIR spectra of RF and X-RF aerogels. Solid CPMAS ^{13}C -NMR spectra of X-RF aerogels crosslinked with Desmodur N3200. XRD of carbon aerogels from native and X-RF aerogels. SEM after heat treatment at three different temperatures of silica aerogels crosslinked with Desmodur N3200.

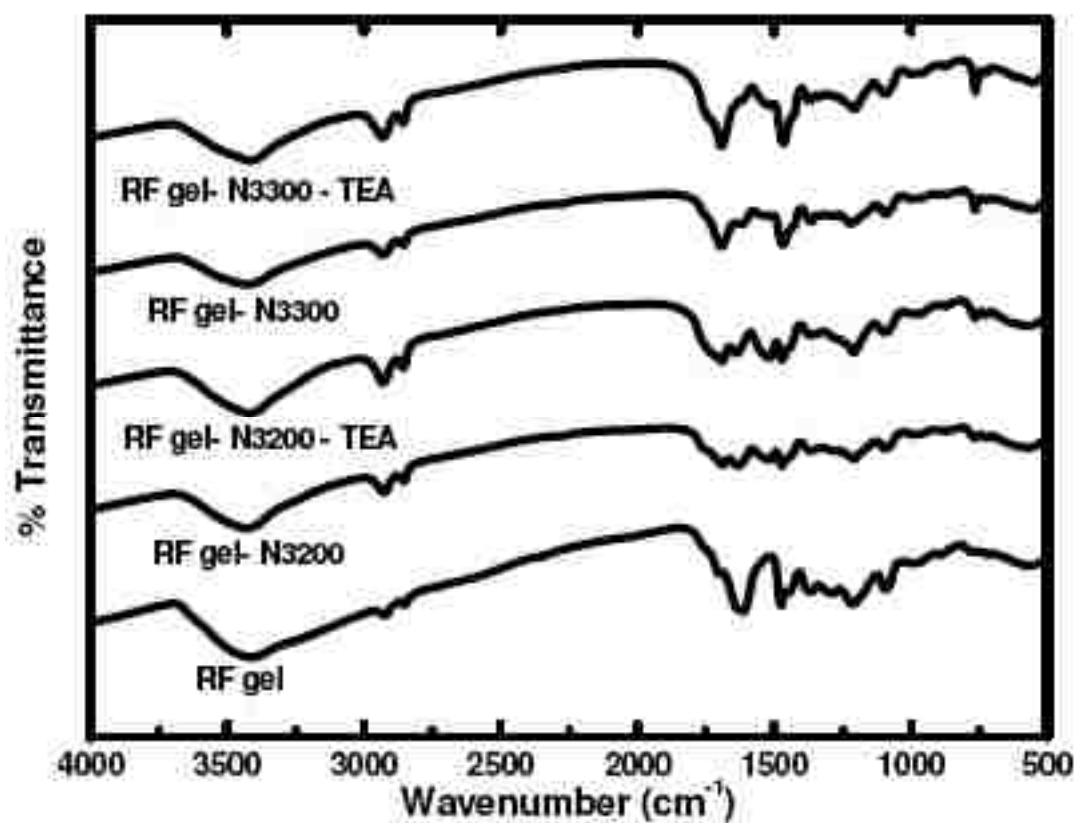


Figure 1S. FTIR spectra of RF and X-RF aerogels.

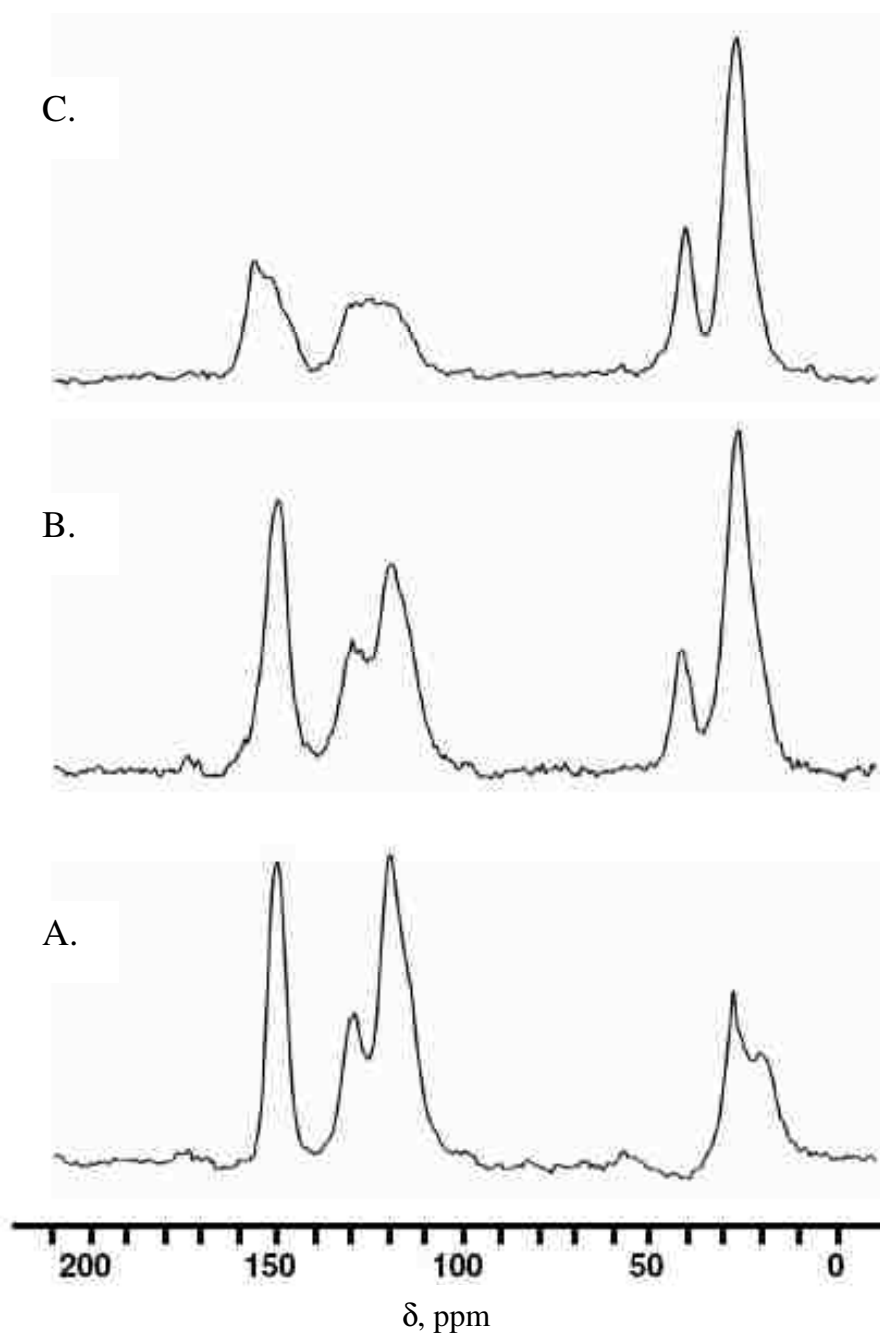


Figure 2S. Solid ^{13}C CPMAS NMR of acid-catalyzed native RF aerogel (A), a X-RF aerogel sample crosslinked with Desmodur N3200 without catalyst (B) and a X-RF aerogel sample crosslinked with Desmodur N3200 in the presence of TEA. (For pertinent materials characterization data refer to Table 1.)

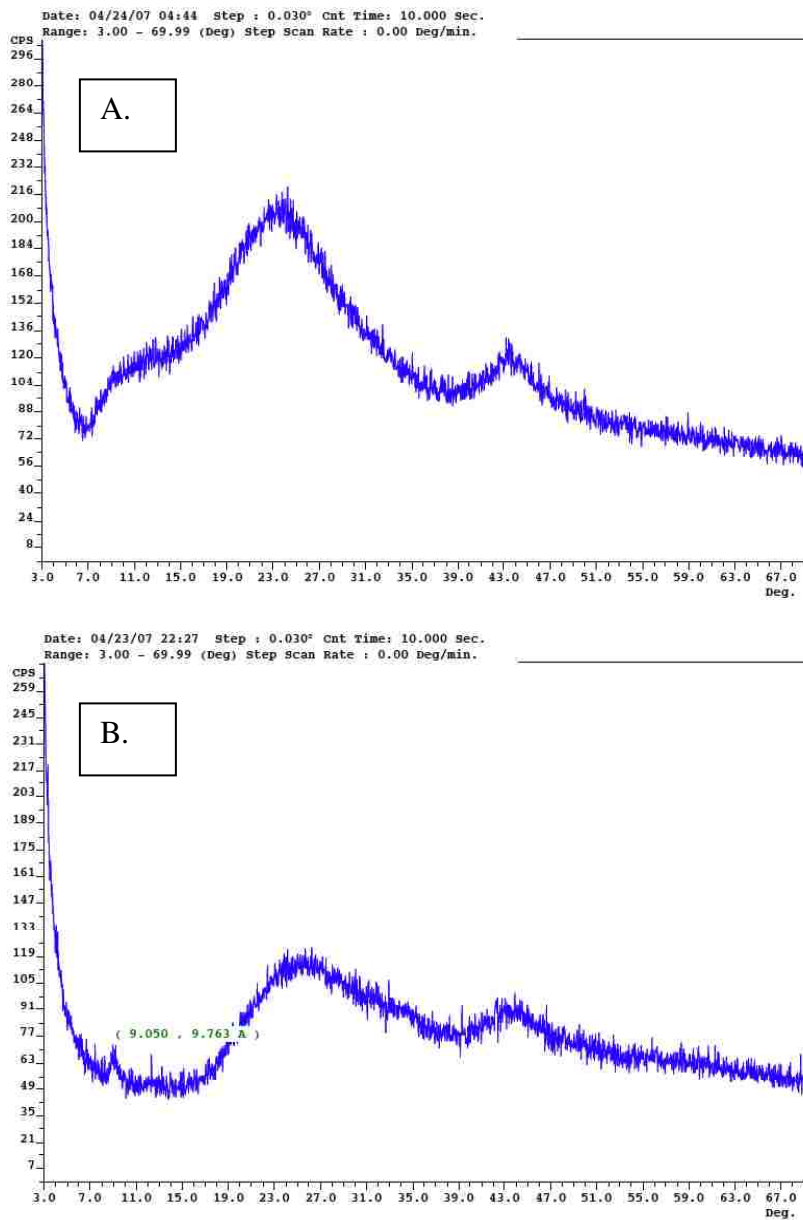


Figure 3S. XRD of C-aerogels. (A) From pyrolysis of native RF aerogel. (B) From pyrolysis of X-RF-N3300A.

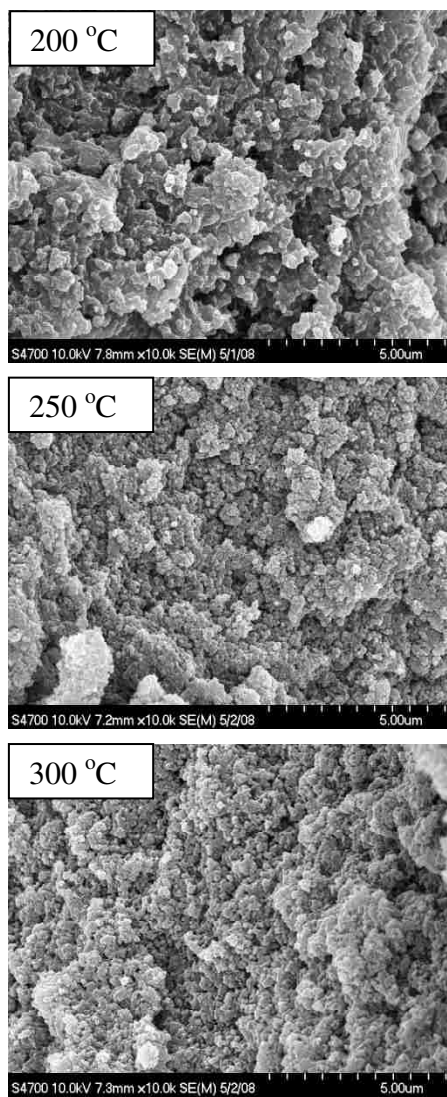


Figure 4S. SEM of silica aerogels crosslinked with Desmodur N3200 and heat-treated for 3 h under Ar at three different temperatures, as indicated.

VITA

Sudhir Mulik was born on March 18, 1979 in Mumbai, India. He received a Bachelor in Technology from North Maharashtra University, India. Following his graduation in 2000, he worked as a Technical Officer for one year with the Research and Development Division of Goodlass Nerolac Paints also in Mumbai. In 2001 he joined University Department of Chemical Technology, Mumbai, from where he received his Masters in year 2003 in Coatings Technology. After that, he came to the University of Missouri Rolla to pursue Ph.D. in Chemistry. He received Ph.D. in Chemistry in year 2008. On the date of his graduation he had 12 papers published and one submitted. He is co-inventor in 5 patent applications.